Royal Holloway, University of London

Department of Physics

Development of a Synchrotron Radiation Interferometer for Accurate Transverse Beam Size Measurement at the LHC

Supervisory team:

Prof. Stephen GIBSON - RHUL

Enrico BRAVIN - CERN

Author:

Daniele BUTTI - ID 100936925

Submitted to the University of London for the degree of Doctor of Philosophy

Academic Year 2022-2023

Acknowledgements

There are many people I need to thank, starting with my team of supervisors. I thank Stephen for always ensuring a smooth progression of my work, Georges for the valuable transfer of knowledge on the subject, and especially Enrico, to whom I certainly owe much more than this thesis.

I am deeply grateful to all the people in the BI-PM section I have met over the years, as they have contributed to making each day interesting. I would like to give a special mention to Andreas, Araceli, Can, Eugenio, Jose, Michele, Salvatore, and Stephane.

Special thanks to all the friends who have helped maintain an acceptable level of mental health, sometimes despite the distance, and in particular to Antonia, Davide, Michela, Miltos, Roberto, Silvia e Valeria.

Infine, il ringraziamento più sentito va alla mia famiglia, per avermi permesso di raggiungere questo traguardo e per il costante sostegno che mi hanno offerto nel corso di questi anni. A loro dedico questa tesi.

Declaration of Authorship

I Daniele Butti hereby declare that this thesis and the work presented in it is entirely my own. Where I have consulted the work of others, this is always clearly stated.

Signed:

Abstract

Accurate monitoring of transverse beam emittance is a critical aspect in the optimization of a particle collider, as it directly influences luminosity, the primary figure of merit for such a machine. At the Large Hadron Collider (LHC), transverse emittance measurements are currently accomplished using synchrotron radiation telescopes (BSRTs) and wire scanners (BWSs). Complementing the existing diagnostics with a novel instrument would be beneficial for reliability and accuracy. The synchrotron radiation interferometer (BSRI) emerges as a promising candidate. Similarly to the BSRT, the BSRI relies on a non-invasive optical technique which can theoretically provide an absolute beam size measurement.

This thesis provides a comprehensive overview of the technique and examines its applicability to the LHC synchrotron radiation source. Extensive numerical simulations are conducted to characterize the emitted synchrotron radiation field and its evolution throughout the different stages of the accelerator cycle. Particular emphasis is placed on the spatial coherence properties of the light, as they are the primary target of interferometric measurements. These studies confirmed the feasibility of using interferometry to measure the LHC transverse beam size. The Van Cittert and Zernike theorem, a fundamental result in classical optics, is applicable with minor corrections that consider the source's specific characteristics.

The existing BSRI test setup underwent refurbishment and upgrades based on the new findings, and the simulation results were systematically benchmarked during the 2022 run of the LHC. The experimental campaign validates the expected performance of the interferometer at injection energy. Discrepancies are identified at the LHC flat-top energy of 6.8 TeV, where measurements are more challenging due to the increased complexity of the synchrotron radiation source. Although the discrepancies are not entirely explained, a semi-empirical model is developed to correct for the systematic loss of contrast observed in interference fringes. The resulting system achieves the 5 % emittance accuracy target required by the machine operation. Absolute measurements are possible at injection energy whereas a calibration with the wire scanner is

necessary at flat-top energy. The ultimate limitation of the interferometer remains the diffraction limit, determined by the operating wavelength within the visible domain. This limitation does not impact the measurement of standard LHC beams, with an emittance of 2.5 µm, as the system's sensitivity is smaller than the corresponding beam size at both injection and flat-top energy. However, the diffraction limit does affect the interferometer's performance at flat-top energy for beams with emittance smaller than 1.5 µm. In this regime, the BSRI can still be used to monitor the relative change of beam size or provide an estimation of the beam size only if the shape of the transverse beam distribution is known a priori.

A redesign of the system, focused on reducing the operating wavelength to the ultraviolet domain, remains the sole solution for improving sensitivity and allowing accurate measurements of the smallest bunches without requiring assumptions about their shape.

Contents

List of Figures

List of Tables

Chapter 1

Introduction

An overview of the Large Hadron Collider (LHC) and its typical operational cycle is presented. The fundamental principles of transverse beam dynamics are reported, introducing the concepts of transverse beam size and emittance and discussing their relationship in circular accelerators. The present status of transverse diagnostics at the LHC is examined, emphasizing the need for additional transverse diagnostic systems. Synchrotron radiation interferometry (BSRI) is presented as a promising candidate for expanding the existing family of operational instruments. The last section states the objective of this thesis to assess the performance of the BSRI as a prospective operational instrument for precise beam size measurements at the LHC.

1.1 The Large Hadron Collider

The European Organization for Nuclear Research (CERN) is a leading institution in the field of particle physics. The laboratory hosts the world's largest accelerator complex [1]. The complex accelerates proton beams to the record energy of 6.8 TeV. The process involves many machines [2, 3] and starts with the acceleration of negative hydrogen ions (H^-) in a linear accelerator, the LINAC4, to an energy of 160 MeV. The hydrogen ions are then stripped and injected into a four-ring synchrotron, the Proton Synchrotron Booster (PSB), where the resulting proton beams accelerated to 2 GeV. The acceleration continues with other two machines, the Proton Synchrotron (PS) and the Super Proton Synchrotron (SPS), which boost the beam energy to 26 GeV and 450 GeV respectively. Finally, particles are injected into the Large Hadron Collider (LHC) where two counter-rotating beams are accelerated to the flat-top energy of 6.8 TeV and collide in four interaction points where as many experiments (ATLAS, ALICE, CMS, and LHCb) study the reactions induced by the particle collisions [4]. When the LHC is in this stationary state, the injector complex is available to serve a multitude of other experimental facilities, whose layout is shown in Fig. 1.1a.

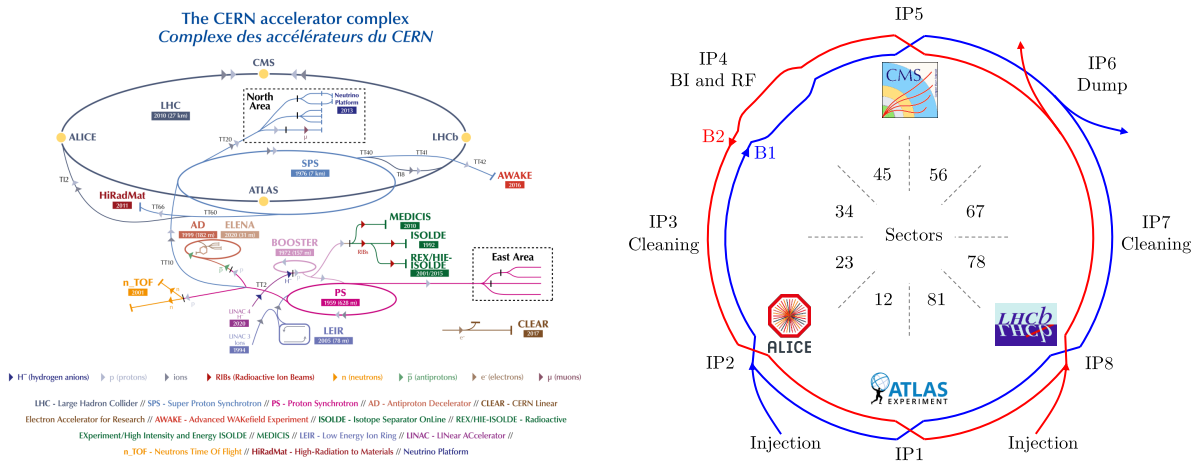

(a) (b)

Figure 1.1: The CERN accelerator complex (a) and the LHC layout (b).

The LHC is a synchrotron that consists of eight sectors. Each sector comprises an arc where the main dipoles and quadrupoles bend and transversely confine the particle beams. The four main LHC experiments and most of the equipment needed to operate the machine are located in the straight sections connecting two consecutive arcs. The structure of the LHC is depicted in Fig. 1.1b. The machine layout at the Interaction Point 4 (IP4) will be discussed in more

detail in Chapter 3 as the LHC synchrotron radiation monitors and the majority of the beam instrumentation are installed at this location.

Parameter	Value	Unit
Circumference	26659	m
Beam energy	$450 \div 6800$	GeV
RF frequency	400	MHz
Bunch spacing	25	ns
Bunch number	2808	
Bunch intensity	1.5×10^{11}	protons
Nominal emittance	2.5	µm
Peak luminosity	2×10^{34}	$\mathrm{cm}^{-2}\mathrm{s}^{-1}$

Table 1.1: Main parameters of the LHC machine and beams.

As the world's most powerful collider, the LHC features unique machine parameters, listed in Tab. 1.1. The *instantaneous luminosity* $\mathcal{L}$ is one of the most important figures of merit. It is proportional to the rate of events $\mathrm{d}N/\mathrm{d}t$ the collider can produce

$$\mathcal{L} \triangleq \frac{1}{\sigma_e}\frac{\mathrm{d}N}{\mathrm{d}t}. \tag{1.1}$$

The normalization to the event cross-section σ_e makes the luminosity a general parameter of the machine, independent of any specific collision reaction. Therefore, the luminosity quantifies the capability of the accelerator to produce collision events. Machine optimization primarily involves the constant monitoring and maximization of luminosity. In a simplified collision model [5, p. 712], the luminosity can be related to other fundamental beam parameters

$$\mathcal{L} = \frac{f_{rev} N_1 N_2 N_{bunch}}{4\pi\sigma_x\sigma_y} \tag{1.2}$$

where f_{rev} is the machine revolution frequency, N_i the particle populations of the two colliding bunches, N_{bunch} the total number of colliding bunches and $\sigma_{x,y}$ the transverse beam size at the collision point. Accurate knowledge of the transverse beam size is of paramount importance for machine performance, as it has a direct impact on luminosity. Beam size measurements are also more versatile than direct luminosity measurements as they allow monitoring the quality of each beam separately at any stage of the accelerator cycle, without necessarily requiring collisions. Hence, transverse profile measurements stand as an essential aspect of beam diagnostics.

1.1.1 The LHC cycle

A typical cycle of the LHC consists of an *injection* stage, an energy *ramp*, and a long period at high energy, known as the *flat-top*, during which the machine is essentially in stationary conditions and collisions occur at the experimental points. Figure 1.2 displays the evolution of energy and beam intensity during a typical fill for physics production.

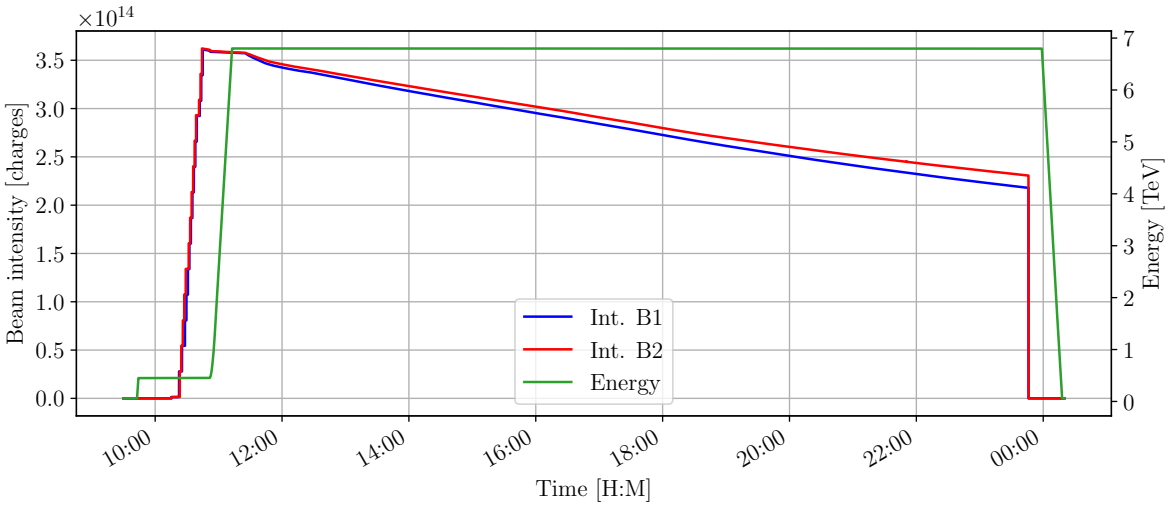

Figure 1.2: An example of an LHC cycle of a typical fill for physics.

The injection process takes approximately 20 minutes, during which trains of bunches from the SPS are injected to fill both beams with a population of up to 2808 bunches per beam, arranged along the ring according to specific filling schemes [6]. Measuring the transverse size at injection is important to confirm the preservation of beam quality from the injectors and to establish the initial reference for the subsequent acceleration [7]. Once the machine is filled, the energy ramp starts, lasting approximately another 20 minutes. At the end of the ramp, the beam energy stabilizes at the flat-top value, the beams are adjusted and collisions start. Throughout the flat-top phase, the beam population is depleted by collisions and losses, resulting in a decrease in luminosity. After typically 10 hours, the beams are dumped, and a new cycle begins.

The injection energy is fixed at 450 GeV, corresponding to flat-top value of the SPS. Over the years, the flat-top energy has been progressively increased through hardware upgrades [8], mainly by increasing the magnetic field of the main dipoles. In 2010, the commissioning value was 3.5 TeV, and starting from the beginning of run 3 in 2022, the flat-top energy is 6.8 TeV. The flat-top energy of 6.8 TeV is used as the default value in this thesis, unless specified otherwise. However, it should be noted that the performance of the SR monitors above 4 TeV is slightly

affected by changes in beam energy. All considerations reported for the 6.8 TeV value are applicable to the 6.5 TeV flat-top of run 2 (2015-2018) and will remain valid in case of future upgrades to reach the LHC design energy of 7 TeV.

1.2 Transverse beam dynamics

In an accelerator beam, the transverse distribution of particles evolves as they propagate through the magnetic lattice of the machine. As beam size measurements are typically performed at only a few locations along the ring, it is helpful to introduce general quantities that allow inferring the beam transverse distribution at any point in the machine.

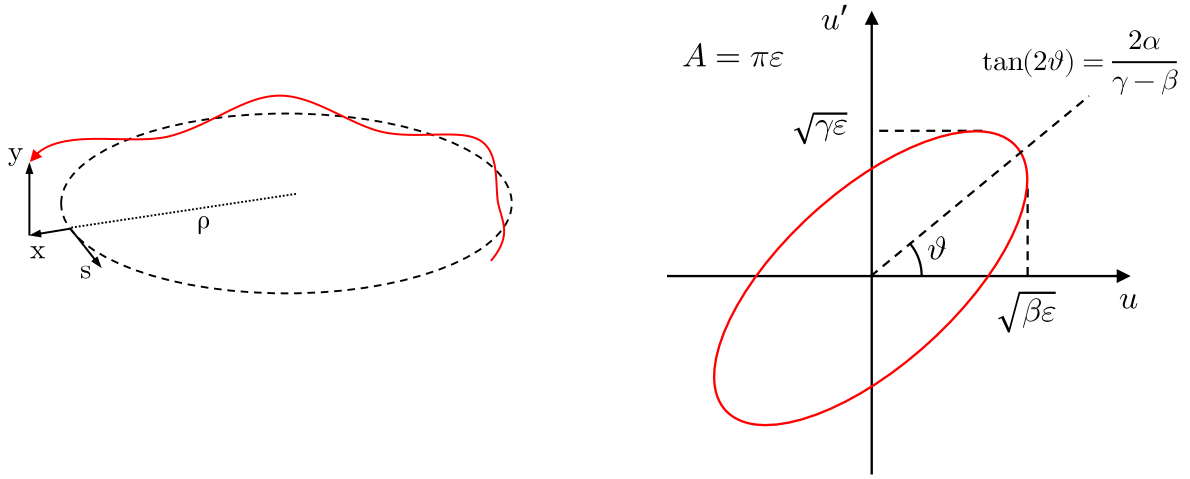

(a) (b)

Figure 1.3: In (a), coordinate frame to study the particle transverse dynamics and, in (b), Twiss ellipse of a single particle.

The motion of particles in the transverse plane of a synchrotron is governed by the magnetic field produced by the several magnets comprising the machine's lattice. Charged particles are subject to the Lorentz force

$$\mathbf{F} = q\mathbf{v} \times \mathbf{B}, \tag{1.3}$$

where q is the particle charge, $\mathbf{v}$ the particle velocity and $\mathbf{B}$ the static magnetic field. Let us consider the motion of a single particle, adopting the coordinate frame shown in Fig. 1.3a. Dipole magnets deflect the particle, causing it to follow a closed trajectory. The *nominal particle* is defined as the ideal particle which is subject only to the dipole magnets deflections. The corresponding trajectory is called the *nominal orbit* of the machine, which is represented by the dotted line in the figure. The nominal orbit defines the centre of the transverse coordinate

system. Quadrupole magnets are used to confine the transverse motion of particles around the nominal orbit and maintain a stable beam. The transverse state of a particle is defined by its coordinates in the *transverse phase space* (u, u'), being u the particle's transverse position (in either the x or y direction) and $u' = \frac{du}{ds}$ its angle, relative to the nominal orbit. Both of these quantities vary along the orbit as functions of the curvilinear coordinate s. The dynamics of the single particle in the transverse plane follows the Hill's equation [9]

$$u''(s) + K(s)\, u(s) = 0, \tag{1.4}$$

a generalization of the harmonic oscillator, in which the strength factor $K(s)$ is not constant but depends on the gradient of the local magnetic field

$$\begin{cases} K_x = \frac{G_x}{p/q} + \frac{1}{\rho^2}, \\ K_y = -\frac{G_y}{p/q}, \end{cases} \tag{1.5}$$

being $G_x = \frac{\partial B_y}{\partial x}$ and $G_y = \frac{\partial B_x}{\partial y}$ the field gradients, p/q the momentum to charge ratio of the particle and ρ the local bending radius of the nominal orbit. The general solution of Eq. 1.4 is

$$u(s) = \sqrt{\varepsilon}\sqrt{\beta(s)}\cos(\phi(s) + \phi(0)), \tag{1.6}$$

with

$$\phi(s) = \int_0^s \frac{1}{\beta(\bar{s})} d\bar{s}. \tag{1.7}$$

The solution of the Hill's equation describes an oscillatory motion of the particle around the nominal orbit with a variable amplitude $\beta(s)$, determined by the strength of the focusing fields. The phase advance of the transverse oscillations is quantified by $\phi(s)$. The integral of $\phi(s)$ over one full revolution along the ring defines the *tune* of the accelerator $Q \triangleq \phi(L)/(2\pi)$. The two free parameters that scale the oscillation amplitude and the initial phase of the oscillations are ε and ϕ_0, respectively. The transverse motion of a particle around the nominal orbit is known as *betatron oscillations*, named after the class of accelerator in which it was first studied.

The Hill's equation admits a constant of motion, referred to as the Courant-Snyder invariant

$$\varepsilon = \beta(s)u'^2 + 2\alpha(s)uu' + \gamma(s)u^2 \tag{1.8}$$

where the parameters (α, β, γ), collectively called *Twiss parameters*, are related as

$$\begin{cases} \alpha(s) \triangleq -\frac{\beta'(s)}{2}, \\ \gamma(s) \triangleq \frac{1+\alpha^2}{\beta}. \end{cases} \tag{1.9}$$

Equation 1.8 can be conveniently represented as an ellipse in the transverse phase space, called the *Twiss ellipse* of the single particle. The relevant points of the Twiss ellipse are marked in Fig. 1.3b. The transverse oscillation of the particle is fully described by this curve, which covers all possible position-angle pairs the particle can have during its motion around the ring. The phase advance $\phi(s)$ defines the angular velocity at which the particle moves around the Twiss ellipse.

So far, the treatment has been limited to the motion of a single particle. Since the Twiss functions depend on the machine lattice and not on the individual particle, the Twiss ellipse is similar for all particles inside the beam. Each single-particle ellipse has a specific area, proportional to ε, which is the free parameter that scales the amplitude of the oscillations. The representation of the particle beam in the transverse phase space is a superposition of many single-particle ellipses, with similar shape but different areas. In most practical cases, the particle distribution in the transverse phase space can be approximated by a bivariate Gaussian defined by the *covariance matrix*

$$\Sigma = \begin{pmatrix} \sigma_u^2 & \sigma_{uu'} \\ \sigma_{uu'} & \sigma_{u'^2} \end{pmatrix}. \tag{1.10}$$

The standard deviations of the distribution correspond to the *beam size* $\sigma \triangleq \sigma_u$, which describes the spread of positions in the transverse direction, and the *beam divergence* $\sigma' \triangleq \sigma_{u'}$, which characterizes the spread of angles. The covariance $\sigma_{uu'}$ represents the correlation between the spatial and angular components of the distribution. The *geometric emittance of the beam* is defined as the square root of the determinant of the covariance matrix

$$\varepsilon_g = \sqrt{\det \Sigma} = \sqrt{\sigma_u^2 \sigma_{u'}^2 - \sigma_{uu'}^2}. \tag{1.11}$$

The extended beam can be described in the phase space as the specific Twiss ellipse with an area given by its geometric emittance $A = \pi \varepsilon_g$. From the representation of the Twiss ellipse shown in Fig. 1.3b, one can relate the geometric emittance with the beam size and divergence,

through the Twiss parameters

$$\begin{cases} \sigma(s) = \sqrt{\beta(s)\varepsilon_g}, \\ \sigma'(s) = \sqrt{\gamma(s)\varepsilon_g}. \end{cases} \tag{1.12}$$

These relationships are fundamental to transverse beam dynamics as they allow the determination of beam size and divergence at any point along the orbit, knowing the geometric emittance of the beam and the values of the machine Twiss functions at that location.

The model outlined in this section describes an ideal machine consisting of perfect dipoles and quadrupoles. Real machines are characterized by higher-order field components due to magnetic multipoles or imperfections in the magnetic field. These higher-order components introduce additional nonlinear terms in the Hill's equation, which perturb the phase portrait of particles at high amplitudes [10]. These effects have a significant impact on the beam, primarily influencing the stability of the beam and causing beam losses. However, since the trajectories inside the beam core are only marginally affected by the field nonlinearities, the linear approximation remains a valid model for describing the beam transverse distributions.

A more significant limitation of this model is the assumptions that all particles in the beam have the same energy. Real accelerator beams are characterised by a finite energy spread and the mean beam energy changes during the acceleration. The next two paragraphs discuss the scenario of non-monochromatic beams and introduce a more convenient definition for the beam emittance in presence of acceleration.

1.2.1 Dispersion

Let us consider a particle with a momentum $p = p_0 + \mathrm{d}p$, slightly off the nominal one p_0. It can be shown [9] that the equation of motion for this particle becomes

$$u''(s) + K(s)u(s) = \frac{1}{\rho}\frac{\mathrm{d}p}{p_0}, \tag{1.13}$$

which is a nonhomogeneous Hill's equation with a constant forcing term induced by the momentum error. Its solution is the sum of the betatron oscillation motion and a term $u_D(s)$, due to the off-momentum of the particle. This additional term is conventionally written as $u_D(s) \triangleq D(s)\,\mathrm{d}p\,/p_0$ where $D(s)$ is defined as *dispersion* function and satisfies the equation

$$D''(s) + K(s)D(s) = \frac{1}{\rho}. \tag{1.14}$$

Since the off-momentum term influences the trajectory of each particle, the transverse size of the beam is affected by dispersion. The expression for the beam size of Eq. 1.12 is amended as

$$\sigma = \sqrt{\langle u_{betatron} \rangle^2 + \langle u_{dispersion} \rangle^2} = \sqrt{\varepsilon_g \beta + D^2 \frac{\sigma_p^2}{p_0^2}}, \tag{1.15}$$

including a positive contribution due to the beam *momentum spread* σ_p, defined as the standard deviation of the off-momentum distribution.

The correction for the momentum spread has an intuitive explanation in the transverse phase space. An off-momentum particle oscillates around an orbit different from the nominal one, because the dipole deflection is proportional to the particle momentum. This transverse displacement leads to a horizontal shift of the particle ellipse in the phase space. As a result, the beam phase portrait is a convolution of the betatron and dispersion terms, hence the addition in quadrature of Eq. 1.15. Since this effect originates from dipolar fields, the dispersion correction is typically only relevant on the horizontal plane of the machine, where most of the bending occurs.

1.2.2 Adiabatic damping and normalized emittance

The geometric emittance defined by Eq. 1.11 is not suitable as invariant of motion when particles are accelerated. The Radio Frequency cavities boost the particle momentum only along the longitudinal direction, thus reducing the particle angle u'. The beam distribution in the phase space shrinks, and the geometric emittance decreases as the particle energy increases. This phenomenon is commonly referred to as *adiabatic damping*, even though it does not involve any dissipative forces. The *normalized emittance* is introduced [5, p.345] to take into account the adiabatic damping

$$\varepsilon_n \triangleq \gamma_{rel} \beta_{rel} \varepsilon_g, \tag{1.16}$$

with γ_{rel} and β_{rel} the particle relativistic factors. The increasing product of $\gamma_{rel}\beta_{rel}$ compensates for the reduction in geometric emittance. Since the normalised emittance is independent of the beam energy, it is a more convenient quantity to describe the transverse beam distributions of accelerate beams.

Throughout this thesis, the beam emittance is always assumed to be the normalized emittance, although it should be noted that the geometric emittance is necessary to calculate the beam size and divergence using Eq. 1.12. As an area in phase space, emittance is technically a

product of length and angle. However, it is common practice, adopted in the following, to omit the angular component and express emittance values in units of µm, aligning with the typical range of normalized emittance at LHC.

1.3 Transverse diagnostics at the LHC

At the LHC, two families of operational instruments are currently used for transverse beam size measurements, wire scanners and synchrotron radiation telescopes. The two devices are complementary and their combined use ensures reliable and accurate transverse diagnostics of the beam.

In addition to these beam instrumentation systems, the beam size information can also be obtained from the data recorded by the four LHC experiments.

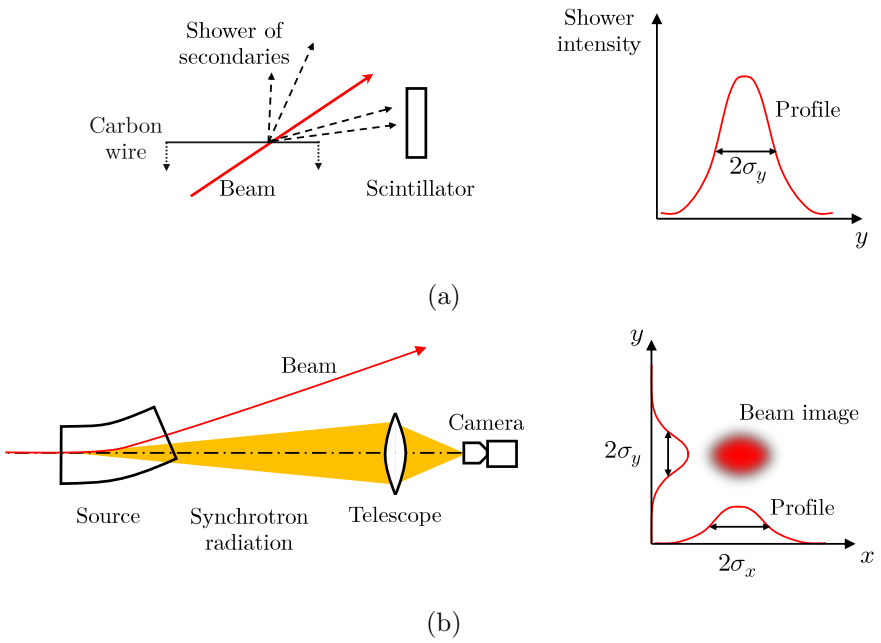

Figure 1.4: Working principle of (a) wire scanners and (b) synchrotron radiation telescopes.

Wire scanner (BWS)

A wire scanner (BWS) is an interceptive device used to measure the transverse beam profile [11]. It consists of a 30 µm thick carbon wire that traverses the beam, generating a shower of secondary particles. These secondary particles are then detected by a downstream scintillator. The shower intensity is proportional to the number of particles intercepted by the wire. Thus, the intensity of secondaries as a function of the wire position provides a reliable estimate of the transverse

beam profile, which can be fitted to determine the transverse beam size.

Wire scanners provide an absolute measurement of the beam size and can be used at any stage of the accelerator cycle and the detection system, based on a plastic scintillator, is sufficiently fast to allow bunch-by-bunch measurements. The instrument is therefore adopted as a reference for the LHC transverse size measurements. The primary limitation of wire scanners is their maximum operating beam intensity [12]. The beam-wire interaction generates losses that can cause the superconducting magnets in the surrounding area to loose their superconducting status and induce a beam dump. The operational limit for the device is currently set to 12 nominal bunches at flat-top energy. This threshold precludes the continuous monitoring of a standard high-intensity fill, thus requiring additional diagnostics.

Synchrotron radiation telescope (BSRT)

The synchrotron radiation telescope (BSRT) is a non-invasive instrument that measures the two-dimensional transverse beam distribution by imaging the synchrotron radiation emitted by the particles [13]. The principle of operation of the device is illustrated in Fig. 1.4b. The system collects the visible synchrotron radiation (SR) spontaneously emitted as the beam is deflected by the magnetic devices of the SR source. A refractive telescope then produces an image of the beam on a fast-gated camera that can resolve a single bunch. The horizontal and vertical profiles are finally extracted from the two-dimensional light distribution and fitted to obtain the standard deviation of the light spot σ_{image}. The intensity distribution at the detector can be written as the convolution between the transverse beam distribution and the system Point Spread Function σ_{PSF}, i.e. the response of the system to the single particle. Assuming that both the beam distribution and the PSF are Gaussian, the size of the light spot can be expressed as

$$\sigma_{image} = M\sqrt{\sigma^2 + \sigma_{PSF}^2}, \tag{1.17}$$

being M the system magnification and σ the transverse beam size.

This imaging-based technique could in principle provide an absolute measurement of the transverse beam size. The system magnification is in fact defined by design and the PSF can be simulated using numerical codes for synchrotron radiation propagation. However, this approach is hindered by the complexity of the LHC synchrotron radiation source, which makes it difficult to accurately determine a priori the real system magnification and Point Spread

Function (PSF). The beam size inferred using the expected values of magnification and PSF are not compatible with the reference values measured by the wire scanners. To overcome this issue, the magnification and PSF parameters need to be experimentally evaluated. The instrument is calibrated in a dedicated fill, where bunches with various emittances are injected, and the reference beam size is measured using wire scanners. Experimental values for magnification and σ_{PSF} are then derived through a linear fit of $\sigma^2_{image}(\sigma^2)$. Distinct calibrations are required for injection and flat-top energy due to variations in the synchrotron radiation source between these stages. Currently, the BSRT cannot provide a reliable measurement during the energy ramp because of the evolution of the synchrotron radiation properties that affect the system's response. This issue will be discussed in the following chapters, as both the BSRT and the interferometer share the same synchrotron radiation source.

Despite these limitations, the BSRT is a highly reliable system. Once calibrated with the wire scanners, its operation is not constrained by beam intensity, enabling real-time and bunch-by-bunch transverse diagnostics at both injection and flat-top energies.

Transverse beam diagnostics from experiment data

Information regarding the transverse beam profile can also be obtained from the data collected by the LHC experiments at the four collision points [14]. While the transverse size of the beam could, in principle, be estimated from the instantaneous luminosity using Eq.1.2, a more robust assessment of the emittance is achieved through an "emittance scan"[15]. This involves transversely displacing the colliding beams and recording the luminosity evolution as a function of beam separation. Neglecting effects due to the crossing angle, this curve is approximately the convolution of the transverse sizes of the two beams.

These techniques have limited operational applicability as they are exclusively available during collisions, cannot provide an independent measurement of each beam, and are conducted only a few times per fill. Despite these limitations, emittance scans offer a completely independent means of assessing the transverse emittance and offer a valuable comparison for the measurements obtained from the beam instrumentation systems.

1.3.1 Need for additional transverse diagnostic systems

Both operational systems currently used for transverse beam diagnostics at the LHC have their own limitations. The wire scanners can provide an absolute measurement of the beam size

throughout the whole accelerator cycle, but they cannot be used at nominal beam intensity due to the beam-wire interaction. On the other hand, the synchrotron radiation telescopes are suitable for continuous monitoring of the beam size, but they require calibration and the measurement during the energy ramp is not reliable due to the complexities of the LHC synchrotron radiation source.

To complement the existing diagnostics, an additional instrument is necessary. The ideal candidate device should be able to provide an absolute measurement of the beam size with an accuracy target of 5 % throughout the entire accelerator cycle, regardless of the beam intensity [16]. Two prototype systems based on beam-gas interaction have been investigated for this purpose, the Beam Gas Vertex monitor (BGV) and the Beam Gas Ionization monitor (BGI). The BGV is a device that infers the beam profile by reconstructing the distribution of the vertices of the beam-gas collisions. The BGV demonstrator, installed at the LHC in 2016, successfully validated the feasibility of the technique [17]. However, due to its high complexity, the exploitation of the BGV as an operational system for transverse diagnostics is challenging. The BGI technique reconstructs the beam profile by detecting the ionization products of the beam-gas collisions. A first prototype of the BGI was installed at the beginning of the LHC era but later removed due to impedance-induced heating issues. A new version based on the Timepix3 detector was proposed in 2019, following the successful implementation of this technology at the Proton Synchrotron [18].

Other techniques are being explored to enhance the LHC transverse diagnostics for the upcoming HiLumi era. Synchrotron radiation interferometry is a promising candidate for non-invasive diagnostics that can complement the operation of synchrotron radiation telescopes by providing an independent and absolute measurement of the beam size. The technique is also a valuable tool for characterizing the coherence properties of the LHC SR source, providing a better understanding of the source used for beam diagnostics.

To explore the feasibility of the technique, a synchrotron radiation interferometer (BSRI) was installed alongside the synchrotron radiation telescope at the beginning of LHC run 2. The successful implementation of the instrument served as a proof of concept [13]. However, unexpected behaviors were observed during systematic measurements conducted at the end of the same run [19].

This thesis presents the results of comprehensive studies aimed at characterizing the coherence properties of the LHC synchrotron radiation source and validating the experimental

findings obtained during run 2. The setup was subsequently refurbished and optimized based on the results of recent synchrotron radiation simulations. The ultimate objective of this thesis is to investigate the performance of the synchrotron radiation interferometer as an operational instrument for accurate beam size measurements at the LHC.

Chapter 2

Principles of Synchrotron Radiation

The physics of Synchrotron Radiation (SR) has been extensively studied in literature, primarily focusing on its application to electron beams in synchrotron light sources. While the underlying physics is the same for both electrons and protons, the higher mass of protons allows for certain simplifications that are typically not applicable to electrons.

This chapter aims to provide the necessary background on synchrotron radiation to understand the characteristics of the LHC SR source. In Section 2.1, an overview of the phenomenon is presented, along with an introduction to the key variables involved. The weak magnet approximation is discussed, which provides an analytical expression for the radiated electric field and is often applicable to proton beams. This approximation is then employed to derive the expressions for the field radiated by a weak undulator and the edge of a magnetic dipole, both relevant in the context of the LHC synchrotron radiation source. Section 2.3 delves into the properties of radiation emitted by a particle in a uniform magnetic field, particularly relevant for describing radiation from the core of dipole magnets that do not satisfy the weak magnet approximation. Since the LHC SR source consists of multiple magnetic elements, the issue of SR interference is addressed in Section 2.4.

While analytical models provide valuable insights into the physics of SR emission, numerical simulations are often essential for accurate quantitative analysis. The final section introduces the simulation code employed in this thesis work, outlining the features and limitations.

2.1 Field radiated by a relativistic charged particle

Synchrotron Radiation (SR) is a form of electromagnetic radiation, emitted when relativistic charged particles experience an acceleration perpendicular to their direction of motion. Although SR naturally occurs in various astronomical objects [20], this chapter focuses on the specific case of radiation emitted by accelerator beams deflected by static magnetic fields. Discovered as an unintended consequence in the early stages of accelerator development [21], synchrotron radiation has since become the focus of dedicated facilities that produce and harness its unique properties across various disciplines in physics, chemistry, and biology [22]. At the LHC, synchrotron radiation is exploited as a tool for non-invasive diagnostics. The spontaneous emission of light within the magnets of the machine provides valuable information about various beam properties, which are investigated using a dedicated family of SR monitors.

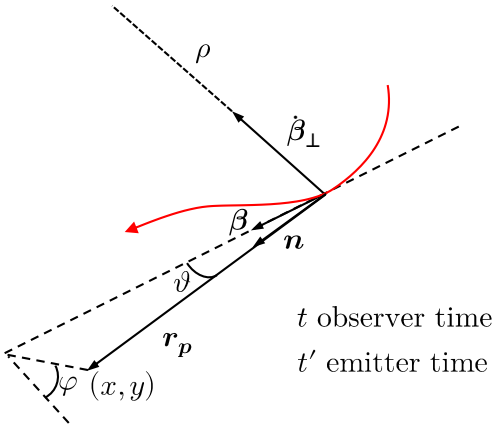

Figure 2.1: Geometry of synchrotron radiation emission. A charged particle with velocity β is deflected with local bending radius ρ and transverse acceleration $\dot{\beta}_\perp$. The $\mathbf{r_p}$ vector defines the observer's position along the observation direction $\mathbf{n}$. Polar coordinates (ϑ, φ) are adopted to describe light emission. Cartesian coordinates (x, y) are used in the following chapters when discussing the spatial distribution of radiation arriving at the entrance plane of the optical system.

Electromagnetic radiation is always emitted when a charged particle is accelerated. In cases involving relativistic particles, this emission can significantly deplete the particle's kinetic energy. A classic example of this phenomenon is Bremsstrahlung radiation, where a charged particle experiences substantial longitudinal deceleration due to Coulomb interactions as it traverses a material, and it is ultimately halted. Synchrotron radiation, on the other hand, primarily involves transverse acceleration induced by static magnetic fields. In the case of hadrons, the high magnetic rigidity prevents strong deflections of the particle's trajectory, resulting in negligible

energy loss compared to the total energy of the particle, thus preserving its longitudinal velocity.

The expression for the field emitted by a moving charged particle can be derived in the time domain from the Liénard-Wiechert potentials [23, p. 661], yielding

$$\mathbf{E}(t) = \frac{q}{4\pi\varepsilon_0}\left[\frac{\mathbf{n}\times((\mathbf{n}-\beta)\times\dot{\beta})}{cr_p(1-\mathbf{n}\cdot\beta)^3}\right]_{t'}. \tag{2.1}$$

In this equation, q is the particle charge, ε_0 the dielectric constant, $\mathbf{n}$ denotes the unit vector in the direction of observation, $\beta = \mathbf{v}/c$ represents the particle's velocity normalized by the speed of light, and $\dot{\beta}$ corresponds to the particle's acceleration. The distinction in time variables implies that the electric field detected by the observer at time t originates from the state of the particle at the emitter time t'. This difference in time scales accounts for the propagation of the electromagnetic radiation from the particle to the observer.

Figure 2.1 provides an overview of the relevant quantities involved. In the case of non-relativistic particles, integrating the field expression leads to the well known Larmor formula for the intensity distribution radiated by an accelerated particle [23, p. 668]. This model accounts for a broad angular distribution of the radiated intensity. The same broad distribution occurs in the case of a relativistic particle, when the radiation is observed from an inertial frame of reference moving at the same velocity as the particle, along a tangent to its trajectory [24]. However, the emission becomes forward-boosted when the radiation is observed from a stationary external observer. This effect arises from the Lorentz transformation between the two frames of reference, which confines the entire intensity within a narrow angle of approximately $1/\gamma$ in the forward direction, where γ is the particle's relativistic factor. The transformation between the emitter and observer frames of reference, qualitatively illustrated in Fig. 2.2, is the ultimate cause of the brightness and highly collimated nature of synchrotron radiation.

2.1.1 Emitter and observer time scales

When a charged particle is accelerated and emits electromagnetic radiation at the time instant t', the radiation propagates at the speed of light c and reaches the observer at a later time instant

$$t = t' + \frac{r_p(t')}{c}, \tag{2.2}$$

where $r_p(t') \triangleq |\mathbf{r_p}(t')|$ is the distance between the observer and the particle, evaluated at the time of the radiation emission. If the particle velocity is significantly smaller than the speed

Figure 2.2: Origin of the brightness and narrow angular emission of synchrotron radiation. A relativistic particle (red arrow) with normalized velocity β experiences a transverse acceleration $\dot{\beta}$, which results in the emission of electromagnetic radiation. On the left, the radiation distribution is observed from an observer traveling at the particle's velocity, along a tangent to the trajectory (black arrow). Since the emitter and the observer travel at similar velocities, the observer perceives only the transverse deflection of the particle, leading to a broad radiation pattern which follows the Larmor model for the intensity radiated by a non-relativistic particle. The radiation distribution in the laboratory frame can be derived by applying a Lorentz transformation from this relativistic observer to a stationary one. This transformation, illustrated on the right, enhances the intensity distribution in the forward direction, giving rise to the characteristic highly collimated distribution of synchrotron radiation.

of light, $r_p(t')$ is a slow function of t'. The two time scales coincide, with the exception of a constant time delay due to the propagation from the emitter to the observer which has no impact on the radiation properties. In a more general scenario, the relationship between the emitter and observer time can be quantified by introducing a *time scale change factor* $\kappa(t')$ [25] defined as

$$\kappa(t') \triangleq \frac{\mathrm{d}t}{\mathrm{d}t'}. \tag{2.3}$$

The time scale change factor has an important physical meaning in the context of synchrotron radiation emission. Due to the finite speed of light propagation, the observer perceives an apparent motion of the emitter which may be different from its actual trajectory. The actions of the emitter within a specific time interval $\mathrm{d}t'$ are perceived by the observer in a different time interval $\mathrm{d}t$. The factor $\kappa(t')$ quantifies the relationship between these two time scales.

The time scale change factor can be expressed explicitly using Eq. 2.2

$$\kappa(t') = 1 + \frac{1}{c}\frac{\mathrm{d}r_p(t')}{\mathrm{d}t'} = 1 - \beta\cos\big(\vartheta(t')\big), \tag{2.4}$$

where last member of the equation stems from the geometry of the problem, as the differential of the distance can be written as $\mathrm{d}r_p(t') = -c\,\mathbf{n}(t')\cdot\beta(t')\,\mathrm{d}t'$.

When the time scale change factor $\kappa(t')$ is approximately equal to 1, the emitter and observer share the same time scale. The observer perceives the actual trajectory of the emitter with a constant propagation delay. This condition occurs when the particle motion is non-relativistic,

i.e. $\beta \approx 0$, or when the observation angles are sufficiently large, i.e. for $\cos(\vartheta) \approx 0$. In this regime, the emission of electromagnetic radiation does not exhibit significant relativistic effects.

The scenario changes significantly when considering a relativistic particle observed at a small angle with respect to the tangent of the direction of motion. As the particle approaches relativistic speeds ($\beta \to 1$) and the observation angle becomes small ($\vartheta \to 0$), we can calculate the Taylor expansion of Eq. 2.4 to obtain

$$\kappa(t') \approx \frac{1 + \gamma^2 \vartheta^2(t')}{2\gamma^2}, \tag{2.5}$$

where the ultra-relativistic approximation $1 - \beta \approx 1/2\gamma^2$ was employed. This expression is a crucial result to interpret synchrotron radiation. It shows that the emitter time scale t' is squeezed into a much faster time scale t of the observer, by a factor proportional to γ^2. A smooth trajectory of the particle may be transformed into an apparent motion marked by abrupt accelerations, ultimately associated to an intense electromagnetic radiation. Since these effects become significant when $\kappa(t') \ll 1$, Eq. 2.5 offers an estimation of the necessary observation angle $\vartheta \approx 1/\gamma$, which corresponds to the well-known typical emission angle of synchrotron radiation. The impact of the time scale change factor on enhancing the radiation intensity is apparent from Eq. 2.1, as the strength of radiated field is inversely proportional to the third power of $\kappa = 1 - \mathbf{n} \cdot \beta$.

A comprehensive characterization of the emitted synchrotron radiation field requires the computation of $\mathbf{E}(t, \mathbf{n})$ as the particle moves along its trajectory. In most cases, the expression of Eq. 2.1 cannot be analytically solved, and numerical integration of the particle trajectory is required to compute the radiated field. The main difficulty comes indeed from the time scale transformation, which distorts the emitter trajectory. However, there are some exceptions where either the particle trajectory allows for an explicit computation of the field or the time scale transformation can be approximated, simplifying the calculation. The weak magnet approximation is one such case, widely applicable to synchrotron radiation emitted by proton beams.

2.1.2 Radiated field in space-time and space-frequency domains

The electromagnetic radiation emitted by a relativistic particle is described by the electric field in the space-time domain, denoted as $\mathbf{E}(t, \mathbf{n})$ in Eq. 2.1. The electric field contains all the necessary information to fully characterize the radiation, as the magnetic field component of the

wave can be determined unambiguously from Maxwell's equations as $\mathbf{B}(t, \mathbf{n}) = \mathbf{n} \times \mathbf{E}(t)/c$.

In many applications of physical optics, it is often convenient to work in the space-frequency domain, where the wavefront can be expressed as a superposition of monochromatic components. This transformation is achieved through a Fourier transform, leading to the definition of the *Fourier-transformed* field as presented in [24, p. 35]

$$\tilde{\mathbf{E}}(\omega, \mathbf{n}) = \frac{1}{\sqrt{2\pi}} \int \mathbf{E}(\mathbf{n}, t) e^{-i\omega t} \, \mathrm{d}t \,. \tag{2.6}$$

In this thesis, the characterization of the synchrotron radiation field is primarily presented in the space-frequency domain. The Fourier-transformed field $\tilde{\mathbf{E}}(\omega, \mathbf{n})$ is thus referred to as the "field" or "wavefront" of the radiation.

The optical intensity associated with the radiation can be obtained by taking the square modulus of the field $I(\omega, \mathbf{n}) \propto \left|\tilde{\mathbf{E}}(\omega, \mathbf{n})\right|^2$. Appendix A provides detailed information on the variables useful for quantifying radiation intensity and their exact relationship with the radiation field.

The angular frequency ω is assumed as the standard frequency variable in the theoretical models presented in this section. However, depending on the context, it is also convenient to express the field in terms of the radiation wavelength λ or the radiation wavevector k. The relationship

$$\omega = 2\pi \frac{c}{\lambda} = ck \tag{2.7}$$

allows for easy interchangeability between the frequency, wavelength, and wavevector representations of the radiation.

2.2 The weak magnet approximation

The transformation from emitter to observer time, as described by Eq. 2.5, is generally not a constant of motion. As the particle moves along the trajectory, its direction changes, resulting in different observation angles, hence the time dependence of $\vartheta(t')$. If the particle experiences a "small" deflection and the acceleration takes place over distances that are shorter than the observation distance, the observation angle can be approximated as constant [26]. This approximation dramatically simplifies the computation of the field, as the time transformation reduces to a constant scaling factor. In this case, the apparent trajectory of the particle is not distorted

by the time transformation, but only compressed along the direction of motion by a constant factor. This condition is known as the *weak magnet approximation* because it relies on the assumption of a small deflection of the particle. The complete derivation, along with a list of the underlying assumptions, is provided in Appendix B. The final result for the field is

$$\tilde{\mathbf{E}}(\omega) = \frac{2r_0\gamma}{r_p}\frac{\left[1-\gamma^2\vartheta^2\cos(2\varphi), -\gamma^2\vartheta^2\sin(2\varphi)\right]}{(1+\gamma^2\vartheta^2)^2}\tilde{B}\Big(\kappa\frac{\omega}{c}\Big), \tag{2.8}$$

being $r_0 = 1/(4\pi\varepsilon_0)\, q^2/(m_p c^2)$ the classical radius of the particle. The function $\tilde{B}(k_{wm})$ denotes the Fourier transform of the magnetic field profile $B(z)$ experienced by the particle as it moves along the magnet, evaluated at the "weak magnet" wavevector $k_{wm} = \kappa\omega/c$. The use of square brackets provides a concise representation of the horizontal and vertical polarization components of the radiated field.

This model has important physical bases. The magnetic field of the weak magnet $B(z)$ is decomposed in its sinusoidal components of wavelength λ_{wm} through a Fourier transform operation. Since a sinusoidal field induces a sinusoidal motion with the same periodicity, the real trajectory of the emitter is itself a linear superposition of sinusoids with wavelengths λ_{wm}. Under the weak magnet approximation, the sinusoidal motion of the emitter is preserved in the observer frame, but the apparent period is squeezed by the constant time scale change κ. In summary, for each sinusoidal component λ_{wm} of the magnetic field, there is a corresponding harmonic contribution to the radiated field at the observation wavelength

$$\lambda = \kappa\lambda_{wm} = \frac{1+\gamma^2\vartheta^2}{2\gamma^2}\lambda_{wm}. \tag{2.9}$$

The weak magnet approximation is generally not applicable to electrons because of their small mass, which allows for significant deflections even in relatively weak magnetic fields. Conversely, the model is valid for high-energy proton beams due to their high magnetic rigidity. This approximation can be effectively exploited to characterize the radiation emitted by a wide class of magnetic devices in proton accelerators, such as the case of the LHC.

2.2.1 Weak undulator radiation

A plane undulator is a magnetic device that consists of a series of N_u alternating poles with a period of λ_u. This device generates a periodic magnetic field that can be written as

$$B(z) = B_0 \,\mathrm{rect}\left(\frac{z}{N_u \lambda_u}\right) \cos\left(\frac{2\pi}{\lambda_u} z\right), \tag{2.10}$$

where the cosine term represents the ideal harmonic component of the field whereas the rect function defines the finite longitudinal extension of the device. Within the undulator, the periodic field induces a sinusoidal motion with maximum angular deflection $\delta = B_0 q \lambda_u / 2\pi\gamma m_0 c$. The undulator *deflection parameter* K is defined as the maximum deflection angle normalised by the typical SR opening angle $1/\gamma$

$$K \triangleq \frac{B_0 q}{m_0 c} \frac{\lambda_u}{2\pi}. \tag{2.11}$$

In the limit $N_u \gg 1$, the particle motion can be well approximated as purely sinusoidal. This scenario of infinitely long undulator serves as a prototypical case to discuss the weak magnet approximation, as the Fourier transform of the field involves only a single harmonic component. The solution to the equation of motion for the emitter in an infinite sinusoidal field is given by

$$x(t') = \frac{K}{\gamma k_u} \sin\left(k_u c t'\right), \tag{2.12}$$

being $k_u = 2\pi/\lambda_u$ the wavevector associated with the undulator period. The apparent transverse motion $x(t)$ can be computed applying the time transformation of Eq. 2.2. The numerical computation of the apparent motion for different values of the deflection parameter is shown in Fig. 2.3.

In the small deflection case ($K = 0.1$), the apparent motion remains a sinusoid with an apparent period of $\lambda_u/(2\gamma^2)$. This result represents the essence of the weak magnet model, as it shows the apparent transverse motion of the emitter is squeezed without distortions by the constant time scale change factor κ. An undulator with $K \ll 1$ is referred to as *weak plane undulator* and the corresponding radiation is characterized by a single fundamental harmonic, determined by the undulator period. As the deflection parameter increases, the emitter trajectory becomes more distorted. In the case of $K = 10$, sharp cusps appears, causing a sequence of strong apparent accelerations of the particle. A large deflection parameter also leads to a longer

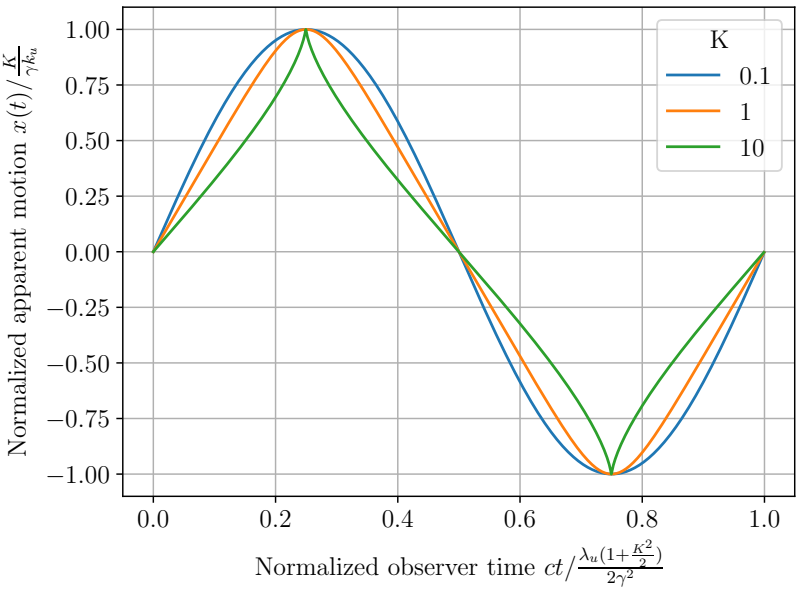

Figure 2.3: Apparent motion of a particle within one period of an infinitely extended plane undulator, numerically computed for different values of the deflection parameter K along the undulator axis $\vartheta = 0$. The scaling factor of the vertical axis normalize the displacement by the maximum amplitude of the oscillation. The horizontal axis is instead scaled to normalize the duration of the apparent motion within the single period.

duration of the single period motion because of the longer curvilinear trajectory the particle has to travel, approximately given by $\lambda_u(1 + K^2/2)$. The case of $K \gg 1$ corresponds to a *strong plane undulator*. This example highlights that while the real motion of the particle is purely harmonic, the apparent motion deviates from pure harmonic behavior. As a result, the radiation emitted by a strong undulator necessarily features a spectrum with higher-order harmonics.

Figure 2.4 provides further insights into the origin of such distortion in the apparent trajectory [27]. The real motion $x(t')$ of the particle is a sinusoid corresponding to the transverse displacement within an undulator period. The apparent trajectory follows from the time transformation of Eq. 2.2. The constant propagation delay is omitted as it does not induce any motion distortion, and the time coordinates can be conveniently shifted to set $t = t' = 0$ at the centre of the undulator period. If the particle is travelling towards the observer, positions with negative t' are farther compared to the positive ones. The distance $r_p(t')$ is therefore positive for $t' < 0$ and viceversa. Under the time transformation of Eq. 2.2, this condition implies that the emitter positions $x(t')$ at $t' < 0$ are delayed by $r_p(t')/c$ in the observer time frame, whereas emitter positions $x(t')$ at $t' > 0$ are advanced by the same amount in the observer time frame. Consequently, the sinusoidal trajectory in the emitter frame is compressed in the observer frame, leading to the sharp cusps in the apparent motion.

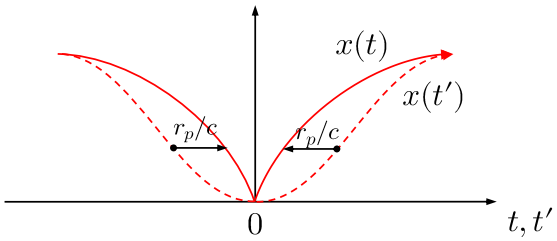

Figure 2.4: Sketch illustrating the appearance of sharp cusps in the apparent motion of a strong undulator. The emitter trajectory $x(t')$ (dashed red line) and the apparent trajectory $x(t)$ (solid red line) are plotted as functions of their respective times. The transformation between the two is discussed in the text.

For typical values of the magnetic field $B_0 \approx 1\,\mathrm{T}$ and undulator period $\lambda_u \approx 10\,\mathrm{cm}$, the deflection parameter for hadron beams is always much smaller than one. Therefore, the weak undulator approximation is always valid.

To obtain the radiated field, it is necessary to compute the Fourier transform of the field profile $B(z)$. By applying the convolution theorem, the Fourier transform of Eq. 2.10 can be analytically determined as

$$\tilde{B}(k_{wm}) = \frac{1}{\sqrt{2\pi}} \frac{L_u}{2} \left[\mathrm{sinc}\left(\frac{L_u}{2}(k_{wm} + k_u) \right) + \mathrm{sinc}\left(\frac{L_u}{2}(k_{wm} - k_u) \right) \right] \tag{2.13}$$

being $L_u = N_u \lambda_u$ the undulator magnetic length and $k_u = 2\pi/\lambda_u$ the wavevector associated with the undulator period. This expression is then evaluated at $k_{wm} = \kappa\omega/c$ and substituted into Eq. 2.8 to obtain the field radiated at the angular frequency ω

$$\tilde{\mathbf{E}}(\omega) = \frac{2r_0\gamma}{r_p} \frac{\left[1 - \gamma^2\vartheta^2\cos(2\varphi), -\gamma^2\vartheta^2\sin(2\varphi)\right]}{(1+\gamma^2\vartheta^2)^2} \frac{1}{\sqrt{2\pi}} \frac{L_u}{2} \left[\mathrm{sinc}\left(\pi N_u \frac{\omega + \omega_1}{\omega_1} \right) + \mathrm{sinc}\left(\pi N_u \frac{\omega - \omega_1}{\omega_1} \right) \right]. \tag{2.14}$$

The quantity ω_1 is the undulator *proper angular frequency*, defined as $\omega_1 \triangleq k_u c/\kappa$. The proper frequency can be conveniently expressed as a wavelength, resulting in the undulator *proper wavelength*

$$\lambda_1 = \kappa\lambda_u = \frac{\lambda_u}{2\gamma^2}\left(1 + \gamma^2\vartheta^2\right), \tag{2.15}$$

which corresponds to the period of the apparent sinusoidal motion of the particle. Let us discuss this result. The field of Eq. 2.14 is peaked around the angular frequency $\omega = \omega_1$, meaning that the radiation is predominantly emitted at the proper wavelength $\lambda = \lambda_1$. In this condition, the undulator is said to be *tuned* as the observation wavelength matches the periodicity of the apparent sinusoidal trajectory. The subscript convention for λ_1 is derived from the context of

strong undulators. In a strong undulator, the emitted radiation consists of a discrete set of harmonics given by $\lambda_n = \lambda_1/n$. However, in a weak undulator, where the purely harmonic apparent motion is preserved, only the fundamental wavelength λ_1 satisfies the tuned condition.

The radiation spectrum exhibits a central lobe, whose characteristic width is determined by the length of the undulator

$$\frac{\Delta\lambda}{\lambda_1} \propto \frac{1}{N_u}, \tag{2.16}$$

Secondary lobes with decreasing intensity appear due to the oscillatory behavior of the sinc function. Undulators installed in synchrotron light sources are typically designed with a large number of periods, resulting in $N_u \approx 100$. These devices possess a significant intrinsic monochromaticity due to the narrow bandwidth of the main lobe. In order to observe radiation from the undulator, the observation wavelength must be close to the proper wavelength, and the first sinc function of Eq. 2.14 is often negligible for $\omega \neq \omega_1$. In contrast, shorter undulators provide a broader radiation spectrum, allowing the use of off-resonance wavelengths. In this case, both sinc contributions of the field are needed to accurately describe the radiation spectrum, which is asymmetric with respect to the proper frequency.

The number of periods also determines the width of the radiation emission angle. The sinc function of $\mathbf{E}(\omega)$ can be approximated by a Gaussian distribution[1], whose standard deviation yields

$$\sigma' \simeq \frac{1}{2\gamma}\sqrt{\frac{1}{N_u}} \tag{2.17}$$

at the tuned condition $\lambda = \lambda_1$. This result is compatible with the rough estimate of $1/\gamma$ as a typical SR opening angle. Since light divergence plays a major role in determining the spatial coherence properties of a source of light, this estimation for σ' will be recalled when discussing this subject.

The polarization of undulator radiation is predominantly linear in the horizontal direction, corresponding to the particle's wiggling motion in the horizontal plane. The peak of the horizontal polarization occurs on-axis, where the apparent transverse acceleration projection is maximized. On the other hand, the vertical polarization exhibits a node on the undulation plane, as the apparent trajectory seen from this plane is characterized by no vertical accelerations. Quantitative examples of the weak undulator spectrum and intensity distribution will be provided in the characterization of the LHC undulators.

[1]The approximation is performed by assuming an equal area for the two intensity distributions.

2.2.2 Edge radiation

Edge radiation is a peculiar type of synchrotron radiation, emitted when a particle traverses the fringe field at the edge of a dipole [28]. It arises from the abrupt transverse acceleration caused by the magnet edge, resulting in an emission that contains enhanced high-frequency components. In cases where the synchrotron radiation emitted by the magnet core is primarily concentrated at a much lower frequency than the observation frequency, edge radiation becomes the prevailing contribution of the radiated field.

The longitudinal profile of the magnetic field at the entrance edge of a dipole can be described as a piecewise function

$$B(z) = B_0 \left[H(z) + H(-z) e^{z/l_{edge}} \right] = \begin{cases} B_0 \, e^{z/l_{edge}} & z \leq 0, \\ B_0 & z > 0. \end{cases} \tag{2.18}$$

Here, B_0 represents the strength of the uniform magnetic field inside the dipole. The function $H(z)$ denotes the Heaviside step function, and the fringe field of the magnet is modeled as an exponentially decaying tail with a characteristic length of l_{edge}. In an ideal dipole without a fringe field, referred to as hard edge dipole, the edge length is considered to be zero. In real scenarios, the diameter of the yoke aperture provides a reasonable initial guess for the extent of the fringe field [29].

Regardless of the strength of the dipole, the edge of the magnet is a relatively short region that induces a negligible deflection of the particle. The weak magnet approximation can be applied, as the observation angle ϑ remains conserved throughout the fringe field region. This allows for a simplified analysis and modeling of the radiation emitted in the vicinity of the magnet edge. The magnetic field profile $B(z)$ can be Fourier-transformed[2] to obtain the expression for $\tilde{B}(k_{wm})$ required in Eq. 2.8

$$\tilde{B}(k_{wm}) = \frac{1}{\sqrt{2\pi}} \frac{iB_0}{k_{wm}} \left(1 - \frac{il_{edge}k_{wm}}{1 + il_{edge}k_{wm}} \right) \triangleq \tilde{B}_{hard}(k_{wm}) \cdot f(l_{edge}). \tag{2.19}$$

This expression shows that the effect of the fringe field can be represented as the contribution of the ideal hard-edge $B(z) = B_0 \, H(z)$, multiplied by a function of the decaying tail $f(l_{edge})$. The modulus of $f(l_{\text{edge}})$ is always less than unity, indicating that the presence of a smooth fringe field

[2] The Fourier transform of the Heaviside's step function reads $\tilde{H}(k_{wm}) = \frac{1}{\sqrt{2\pi}} \frac{i}{k_{wm}} + \sqrt{\frac{\pi}{2}} \delta(k_{wm})$ where we omit the δ term neglecting the singularity at $k_{wm} = 0$.

suppresses the intensity of the radiated field, which is proportional to $|\tilde{B}|^2$. This observation is consistent with the physical interpretation of the weak magnet approximation, as a sharper field profile corresponds to a higher frequency content in the emitted radiation. The contribution from the fringe field becomes negligible when $l_{\text{edge}} \ll 1/k_{wm}$, and in such cases, the emitted radiation can be well approximated using only the hard-edge model. Recalling Eq. 2.9, we can express this limit as $\lambda \gg \kappa l_{\text{edge}}$, emphasizing that the specific form of the fringe field is not significant as long as the observation wavelength λ is significantly larger than the characteristic extension of the fringe tail l_{edge}, compressed by the time-scale change factor κ. To provide a numerical example, the wavevector corresponding to a typical visible wavelength of $\lambda \approx 500\,\text{nm}$ and relativistic factor $\gamma \approx 1000$ ($E_{proton} \approx 1\,\text{TeV}$) is in the order of $\lambda_{wm} \approx 1\,\text{m}$. The hard edge model is always valid for realistic values of $l_{edge} \approx 1\,\text{cm}$. We conclude that, at these energies, the fine features of the fringe field can be resolved only by working with wavelengths much shorter than the visible range.

The complete expression for the Fourier-transformed field becomes

$$\tilde{\mathbf{E}}(\omega) = \frac{2r_0\gamma}{r_p} \frac{\left[1-\gamma^2\vartheta^2\cos(2\varphi), -\gamma^2\vartheta^2\sin(2\varphi)\right]}{(1+\gamma^2\vartheta^2)^2} \frac{1}{\sqrt{2\pi}} \frac{iB_0}{\omega} \frac{2\gamma^2 c}{1+\gamma^2\vartheta^2} \left[1 - \frac{1}{1-\frac{2\gamma^2 c}{1+\gamma^2\vartheta^2}\frac{i}{\omega l_{edge}}}\right]. \tag{2.20}$$

The weak magnet approximation for the edge radiation is self-consistent when describing the high-frequency behaviour of the emitted field. A problem exists in the opposite limit where Eq. 2.19 diverges for low observation frequencies ($\omega \to 0$). The inconsistency comes directly from the field profile used to derive the edge radiation. The step function of Eq. 2.18 represents an infinitely long magnet which inevitably cannot induce a negligible deflection. The expression derived for the edge radiation is only suitable to describe the high-frequency components of the emitted radiation, dominated by the abrupt variation of the magnet fringe field. An alternative model is required to accurately describe the low-frequency emission, which arises from the continuous deflection of particles within the uniform magnetic field of the magnet core. In the next section, we will focus on the radiation emitted by the magnet core. This type of radiation exhibits a broad spectrum of frequencies centered around a characteristic frequency, called critical frequency. The critical frequency depends on the particle energy and the bending radius of the magnet. To operate in a regime dominated by edge radiation and make use of Eq. 2.20, it is important to ensure that the observation frequency significantly exceeds the critical frequency of the dipole.

The field profile described by Eq. 2.18 corresponds to a rising magnet edge, and the derived expression for $\tilde{\mathbf{E}}(\omega)$ is suitable for describing the radiation emitted by a particle entering a dipole. In the case of a falling edge, we can simply invert the spatial coordinate, $B(z) \rightarrow B(-z)$ and apply the reversal property of the Fourier transform, $\tilde{B}(k_{wm}) \rightarrow \tilde{B}(-k_{wm})$. This property simplifies the treatment of radiation emitted by both entrance and exit dipole edges. The result is particularly helpful for studying the case of two consecutive dipoles bonding a straight section. The radiation emitted at the exit edge of the upstream magnet overlaps with the entrance edge radiation of the downstream magnet, resulting in interference effects. If the magnets are identical, the emitted wavefronts have the same magnitude but opposite phase, which must be taken into account in the interference description. Further details about the interference of synchrotron radiation emitted by different sources will be discussed in Sec. 2.4.

2.3 Ordinary synchrotron radiation

The last analytical model presented in this chapter pertains to the synchrotron radiation emitted by a particle travelling on a circular orbit. This model describes one of the most common situations of a particle bent by a uniform magnetic field and the resulting radiation is referred to as *ordinary synchrotron radiation* or *core radiation* of a dipole magnet. The weak magnet approximation does not apply to this case as the observation angle eventually spans 2π over the full turn. The circular trajectory is nonetheless one of the few cases for which the radiated field can be analytically computed. Due to the specific geometry of the problem, the radiation field exhibits symmetry with respect to the orbit plane and axial symmetry around the revolution axis. For a horizontal orbit plane, the synchrotron radiation field depends only the latitudinal angle ϑ. The problem of computing the radiation emitted along a circular trajectory was first solved by Schwinger and the resulting field distribution is named after him [30]. The derivation is quite tedious, with the difficulties stemming more from the extensive computations required rather than the physics of the emission process. The final result for the radiated field is

$$\tilde{\mathbf{E}}(\omega) = \frac{-\sqrt{3}q\gamma}{(2\pi)^{3/2}\epsilon_0 c r_p}\frac{\omega}{2\omega_c}(1+\gamma^2\vartheta^2)\left[K_{2/3}(\xi), -i\frac{\gamma\vartheta}{\sqrt{1+\gamma^2\vartheta^2}}K_{1/3}(\xi)\right] \tag{2.21}$$

where K_ν represents the modified Bessel function of second kind of order ν and $\xi = \frac{\omega}{2\omega_c}(1 + \gamma^2\theta^2)^{3/2}$ an auxiliary variable. ω_c is the radiation *critical angular frequency*, defined as

$$\omega_c \triangleq \frac{3}{2}\frac{c\gamma^3}{\rho}, \tag{2.22}$$

being ρ the radius of the circular orbit. The critical frequency is an important parameter to characterize ordinary synchrotron radiation as it divides the spectrum in two regions of equal power. The primary limitation of this model is the small angle approximation required to derive this result. The Schwinger distribution provides an accurate estimate for the field at $\vartheta \lesssim 1/\gamma$ whereas the exponential decay of the Bessel functions underestimates the background radiation at larger polar angles. It is worth mentioning that the weak magnet approximation can still be applied to describe the radiation at large angle observations [31]. When the observer is positioned at significant latitude angles, the observation angle does not change significantly over the particle revolution. This behavior can be understood by considering the limit where the observer is positioned above the revolution orbit, resulting in an observation angle that remains approximately constant at $\vartheta \approx \pi/2$ throughout the entire orbit. As a result, the conservation of the observation angle allows the application of the weak magnet approximation for large angle radiation, regardless of the actual strength of the magnet.

Figure 2.5 presents some examples of intensity curves computed using the Schwinger model. The Schwinger distribution can be conveniently generalized using normalized units defined as $\gamma\vartheta$ for the polar angle, and ω/ω_c for the observation frequency.

The angular distributions presented in Figure 2.5 provide information on the characteristic opening angle of the radiation. At the critical frequency $\omega = \omega_c$, the Schwinger profile closely resembles a Gaussian distribution with a standard deviation of $1/\gamma$. As the observation frequency increases, the opening angle becomes narrower, indicating a more focused radiation. Conversely, for frequencies below the critical value, the characteristic angle is larger than the $1/\gamma$ prediction. Using the same approach presented for undulator radiation, the divergence of ordinary synchrotron radiation can be approximated by the trend [25]

$$\sigma' \simeq \begin{cases} \frac{1}{\gamma}\left(\frac{\omega}{\omega_c}\right)^{-1/3} & \text{if } \omega < \omega_c, \\ \frac{1}{\gamma} & \text{if } \omega \approx \omega_c, \\ \frac{1}{\gamma}\left(\frac{\omega}{\omega_c}\right)^{-1/2} & \text{if } \omega > \omega_c. \end{cases} \tag{2.23}$$

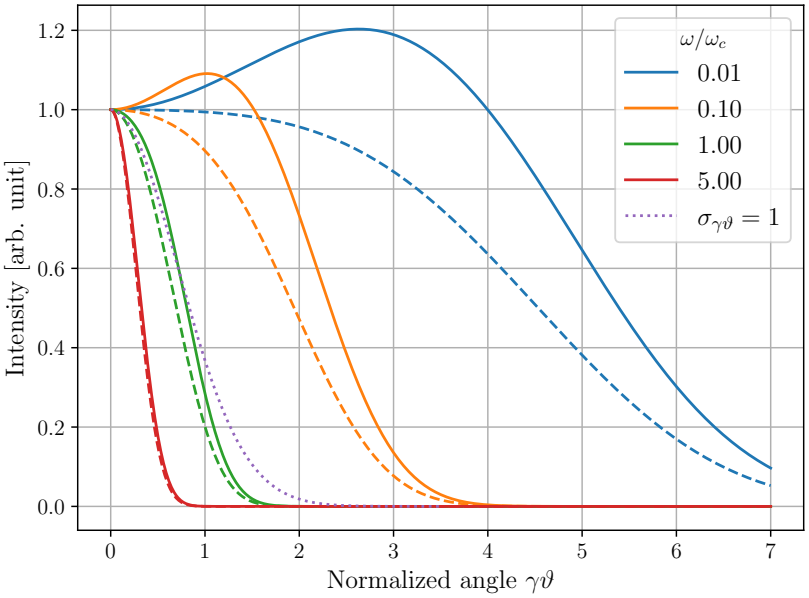

Figure 2.5: Schwinger distributions of the total (solid lines) and horizontal (dashed lines) polarization components of the core radiation field, computed at different observation frequencies. The polar angle is normalised by the characteristic SR opening angle $1/\gamma$. A simple Gaussian with angular aperture $\sigma' = 1/\gamma$ is plotted for reference (purple dotted line).

All estimations are consistent, within a reasonable range of frequencies, with the usual value of $\sigma' \approx 1/\gamma$. This result highlights another property of the critical frequency ω_c as it corresponds to the best approximation of $1/\gamma$ for the light opening angle. It is important to note that the radiation opening angle exhibits a relationship with the radiation wavelength that is less than linear. This means that as the wavelength increases, the increase in the opening angle is not as rapid. This relationship between the angular spread and the wavelength is particularly relevant when evaluating the performance of optical systems, as the achievable resolution is determined by a combination of these two parameters.

To conclude, let us discuss the polarization properties of the core radiation. The horizontal component is the most intense as it is aligned with the direction of maximum transverse acceleration. Similar to the undulator case, when an observer is positioned on the orbit plane, the apparent motion of the particles does not exhibit a vertical component. As a result, no vertically polarized radiation is emitted at $\vartheta = 0$. The intensity of vertical polarization is not negligible out of the orbit plane, especially at observation frequencies lower than the critical one. The field of the vertical polarization changes sign across the orbit plane, as E_y is an odd function of the latitude angle. The phase of the vertical polarization is therefore antisymmetric across the orbit plane whereas the phase of the horizontal component is symmetric. This different behaviour

needs to be taken into account in interferometry and eventually requires the presence of a linear polarizer to eliminate one of the two polarization components.

2.4 Synchrotron Radiation interference

Synchrotron radiation emitted by magnetic devices propagates along the particle beam. Due to its narrow opening angle, the radiation can travel long distances inside the accelerator vacuum chamber without experiencing significant intensity dissipation. Consequently, it is common for the radiation emitted from multiple devices to overlap, resulting in interference effects in the extracted light. The multi-source interference is a relevant phenomenon in SR-based diagnostics. Let us examine the simplest scenario involving only two sources situated along a straight section, as depicted in Fig. 2.6.

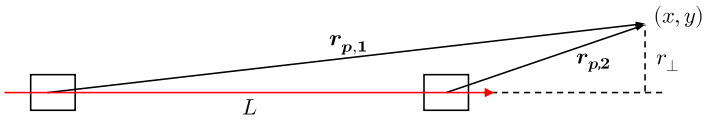

Figure 2.6: Interference of two synchrotron radiation sources. The field emitted by the farthest source propagates along the beam direction for a distance L and reaches the second source. The two-source interference is recorded by an observer placed at the position (x, y) on a plane perpendicular to the main propagation direction.

The manifestation of interference effects crucially depends on the correlation between the single-source fields. In optics, this correlation is quantified by the degree of coherence of the radiation, a subject that will be extensively discussed in Chapter 4. In summary, the narrower the radiation spectrum, the stronger the tendency for fields emitted by the same particle passing through different sources to produce interference effects. Since the treatment in space-frequency domain assumes strictly monochromatic conditions, the correlation of the single-particle radiation is always preserved during the propagation and the total field is the sum of the single-source fields[3]

$$\tilde{\mathbf{E}}(\omega, x, y) = \tilde{\mathbf{E}}_1(\omega, x, y) + \tilde{\mathbf{E}}_2(\omega, x, y) \cdot e^{i\Delta\phi(\omega,x,y)}. \tag{2.24}$$

In this expression, $\Delta\phi$ represents the phase difference between the two interfering fields. The coordinate dependence (x, y) is explicitly written to emphasize that the relationship is point-specific, indicating that the phase of the interference varies with the observer position. The phase difference $\Delta\phi$ can be determined by separately tracking the phase advance for particles

[3]In the opposite scenario of complete lack of correlation, the quantity to be summed is the optical intensity.

and light along their respective paths [32], yielding

$$\Delta\phi = \frac{\omega}{c}\left(\frac{L}{\beta} + r_{p,2} - r_{p,1}\right), \tag{2.25}$$

where $r_p = |\mathbf{r_{p,i}}(x, y)|$ represents the distance between the center of each source and a transverse observer position (x, y). Let $\bar{r}_{p,1} = |\mathbf{r_{p,1}}(0, 0)|$ and $\bar{r}_{p,2} = |\mathbf{r_{p,2}}(0, 0)|$ be the longitudinal distances of the source centres from the observer plane and $r_\perp \triangleq \sqrt{x^2 + y^2}$ the radial coordinate on the observer plane. Under ultrarelativistic, $\beta \approx 1$, and paraxial, $r_\perp \ll \bar{r}_p$, approximations, the quantities can be Taylor-expanded and rearranged to obtain

$$\Delta\phi \approx \frac{\omega}{c}\left(\frac{L}{2\gamma^2} + \frac{r_\perp^2}{2\bar{r}_{p,2}(L + \bar{r}_{p,2})}L\right) \triangleq \frac{\omega}{c}(\Delta\phi_{beam} + \Delta\phi_{sphere}). \tag{2.26}$$

The interference phase consists of two contributions. The term $\Delta\phi_{beam}$ remains constant across the observation plane but varies with the beam energy, while the second term $\Delta\phi_{sphere}$ is independent of beam properties and exhibits a quadratic scaling with the radial coordinate. The contribution $\Delta\phi_{sphere}$ is purely geometric, representing the phase difference between two spherical wavefronts radiated from the source centres. On the other hand, $\Delta\phi_{beam}$ is specific to synchrotron radiation as it quantifies the phase slippage between the particle and the light propagating along the straight section L. Because of the relativistic motion, the source distance is squeezed by the recurring factor $1/2\gamma^2$ and the corresponding phase difference varies slowly with L. The intensity distribution resulting from the interference of the two sources is given by the square modulus of Eq. 2.26, leading to

$$I(\omega, x, y) = I_1 + I_2 + 2\sqrt{I_1 I_2}\cos\left(\phi_1 - \phi_2 - \Delta\phi\right). \tag{2.27}$$

This expression is a specific case of the general law of interference discussed in Chapter 4, applied to fully coherent sources. The light distribution is the sum of the intensities from each individual source and an interference term. The interference term is directly proportional to the product of the electric field strengths and is modulated by the phase characteristics of the sources. The phase modulation term has been separated for convenience into the phase difference $\Delta\phi$, due to the propagation effects of Eq. 2.26, and the contributions originating from the intrinsic phase of the single-source wavefronts, represented by $\phi_1 = \arg(\tilde{\mathbf{E}}_1)$ and $\phi_2 = \arg(\tilde{\mathbf{E}}_2)$. When the sources are identical, $\phi_1 - \phi_2$ is zero. The interference pattern created by the superposition

of the two sources exhibits distinct characteristics associated with $\Delta\phi_{sphere}$ and $\Delta\phi_{beam}$. The $\Delta\phi_{sphere}$ term gives rise to concentric fringes in the pattern, with the fringe spacing decreasing quadratically as a function of the radial coordinate $r_\perp$. On the other hand, $\Delta\phi_{beam}$ determines the initial phase of these intensity oscillations.

2.5 Simulation framework

The analytical formulas presented in the previous sections can be used to characterize the radiation emitted by rather simple magnetic structures, within the limitations of the underlying approximations. For more complex scenarios, such as the SR source used for diagnostics at the LHC, analytical models continue to provide valuable insights into the physical properties of the radiation. However, numerical simulations are necessary to perform accurate and quantitative analyses of the radiated field.

The simulations presented in this thesis are performed using a code based on Synchrotron Radiation Workshop (SRW) [33, 34]. SRW is a standard tool for synchrotron radiation simulations, initially developed at the European Synchrotron Radiation Facility and constantly upgraded by the synchrotron radiation community. The code takes the source magnetic field as input and computes the Fourier-transformed field $\tilde{\mathbf{E}}(\omega, z_p, \mathbf{r}_{\perp,p})$ radiated by a single particle traversing the magnetic structure, where z_p and $\mathbf{r}_{\perp,p}$ define the longitudinal and transverse positions of the observer, respectively. The computation of the emitted wavefront involves integrating the solution of the Helmholtz equation, which describes the transverse components of the electromagnetic field radiated by a charged particle in the frequency domain. This yields the expression for the electric field [35]

$$\begin{aligned}\tilde{\mathbf{E}}(\omega, z_p, \mathbf{r}_{\perp,p}) = \frac{i\omega q}{c^2}\int_{-\infty}^{z_p}\frac{1}{z_p-\bar{z}}\left(\beta_\perp(\bar{z})-\frac{\mathbf{r}_{\perp,p}-\mathbf{r}_\perp(\bar{z})}{z_p-\bar{z}}\right)\\ \cdot\exp\left[i\frac{\omega}{c}\left(\frac{|\mathbf{r}_{\perp,p}-\mathbf{r}_\perp(\bar{z})|^2}{2(z_p-\bar{z})}+\int_0^{\bar{z}}\frac{\mathrm{d}\hat{z}}{2\gamma_z^2(\hat{z})}\right)\right]\mathrm{d}\bar{z},\end{aligned} \tag{2.28}$$

where $\bar{z}$ and $\mathbf{r}_\perp(\bar{z})$ represent the longitudinal and transverse positions of the particle, in the emitter time frame. This approach is equivalent to the one based on the solution of retarded potentials but it is computationally more efficient. Despite being formally more complicated than Eq. 2.1, Eq. 2.28 offers a formula that can be directly integrated to obtain the field radiated at each point of the observation mesh defined by the user. First, the code computes the trajectory of the particle under the effect of the magnetic structure. The instantaneous transverse velocity

$\beta_\perp(\bar{z})$ and the longitudinal component of the relativistic factor $\gamma_z(\bar{z})$ are then derived from the trajectory. Finally, the evolution of these functions along the particle trajectory are numerically integrated, according to Eq. 2.28, to obtain the field $\tilde{\mathbf{E}}(\omega, z_p, \mathbf{r}_{\perp,p})$.

The computation time scales linearly with the longitudinal discretization of the particle trajectory and the size of the mesh at the observation plane. On a standard desktop computer, a detailed mapping of the field radiated by a single particle may take several minutes. The simulation of a finite emittance beam becomes impractical as it typically requires a few thousands particles to accurately reproduce the beam phase space. The code was adapted to perform the parallel computation of the radiated wavefront and the simulation time was drastically reduced by running simulations on a dedicated multi-core server. In addition to the wavefront computation, SRW allows the propagation of the field through an arbitrary optical system, defined as a sequence of drifts or standard optical components (lenses, apertures or obstacles). The computation is performed using standard algorithms of Physical Optics Propagation (POP), based on Fourier optics principles. SRW is a powerful framework for simulations of complete SR beamlines, from the magnetic source to the final image at the detector plane. As with all numerical codes, SRW relies on a set of approximations. The expression of Eq. 2.28 only accounts for the transverse components of the radiated field because the longitudinal component of Helmholtz's equation Laplacian is neglected. This condition is equivalent to the already mentioned paraxial approximation of synchrotron radiation, satisfied as long as the observation angle is small $\vartheta \simeq 1/\gamma$. The field computation is valid in the far field regime, i.e. at observation distances much larger than the radiation wavelength. This second assumption is also verified working in the optical domain. Finally, the particle shall travel in ultrarelativistic regime. The range of LHC energies, from 450 GeV to 6.8 TeV, fulfills this last requirement.

Chapter 3

Spatial and spectral properties of the LHC synchrotron radiation source

This chapter presents the synchrotron radiation source currently used for beam diagnostics at the LHC. The source layout is illustrated and the magnetic devices are individually characterized, using simulations to determine the spatial and spectral distributions of the emitted synchrotron radiation. Simulation results are compared with analytical predictions to provide a physical interpretation of the synchrotron radiation emission process. The spatial distribution of the entire source is then characterized as a function of the accelerator energy, highlighting the notable change of the emitted wavefront during the energy ramp. The accuracy of SRW simulations is confirmed through a comparison between the simulated spatial distribution of the synchrotron radiation intensity and the experimentally observed light distribution at various beam energy. The spatial and spectral properties of the radiated wavefront are comprehensively analyzed through single-particle simulations, which reveal the essential features of the radiation. The chapter concludes by addressing the impact of finite emittance beams, which consist of multiple particles, on the distribution of the emitted light.

3.1 Source layout

The SR monitors of the LHC are installed at Point 4, in the long straight section between the sectors 34 and 45. In this particular section of the accelerator, the nominal beam separation of 19.4 cm is increased to 42 cm to accommodate the accelerating cavities (RF). The separation increase is achieved by means of dipole magnets arranged in a dogleg configuration [36], illustrated in Fig. 3.1a. It involves the use of D4-type dipole magnets to deflect the beams in opposite directions. The diverging beams travel the distance required to obtain the desired separation for the RF cavities and the parallelism is eventually restored by another special magnet, the D3, which compensates for the kick induced by the D4. The same sequence of D4 and D3 is replicated on both sides of the RF cavity section. The layout of the accelerator at Point 4 makes it an ideal location for the installation of SR monitors, as the light emitted by the magnetic devices can be readily extracted along the empty drift sections.

Above a beam energy of 1 TeV, the D3 and D4 dipoles emit synchrotron radiation with a high photon flux in the optical range, making them suitable for non-invasive beam diagnostics. The D3 was selected as the source for the operational SR monitors [37], while the potential use of the D4 dipoles for an additional diagnostics line is being investigated for the upcoming HiLumi LHC era [38]. Neither of these dipoles is suitable for visible diagnostics at the injection energy of 450 GeV, as their typical emission wavelengths are in the far-infrared. A dedicated superconducting undulator, optimized for beam diagnostics purposes at injection energy, was designed and included in the machine lattice [39].

The resulting SR source consists of multiple devices, whose contribution to the radiated wavefront depends on the accelerator energy. Considering Beam 1 as example, particles coming from the left side of Point 4 are first deflected by the $D3_L$, traverse the RF section and reach the opposite side of the straight section where the undulator and the $D3_R$ are located. At injection energy, visible light is only emitted by the undulator. Above 1 TeV the $D3_R$ becomes the most intense source, with a non-negligible contribution from the upstream $D3_L$. The light emitted by these devices is intercepted by an in-vacuum mirror, located approximately 27 m downstream of the undulator centre. Part of the radiation is extracted and directed to an optical table, installed beneath the beam pipe, housing the instrumentation. The extraction system significantly influences the performance of the SR monitors by limiting the horizontal acceptance of the optical systems. The configuration is symmetrical for Beam 2, with its extraction system

and instrumentation situated on the left-hand side of the long straight section.

To conclude the description of the source layout, it is useful to define a coordinate system that can describe the geometry of the source and map the radiated wavefront. The undulator axis is conventionally taken as the reference optical axis, with the undulator centre serving as the origin of the longitudinal coordinate system, denoted by z. The radiated field $\tilde{\mathbf{E}}(\omega, x, y)$ is always computed on planes perpendicular to this axis. The coordinate origin in the transverse plane corresponds to the intersection with the optical axis. The analysis of the spatial properties of the emitted SR involves computing the intensity distribution $I(x, y)$ at a specific wavelength λ. Unless otherwise specified, the intensity is evaluated at the position of the extraction system, which serves as the reference plane for assessing the light distribution.

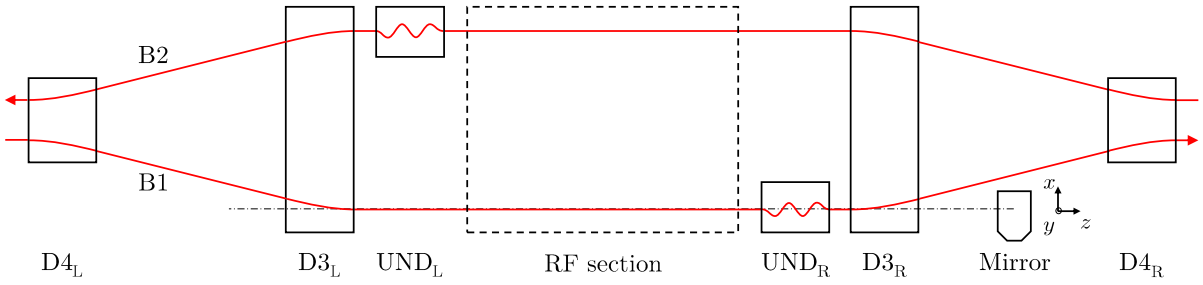

(a)

(b)

Figure 3.1: Schematic diagram (a) illustrating the layout of the synchrotron radiation source used for beam diagnostics at the LHC. The vertical scale is exaggerated to emphasize the beam deflections within the magnetic devices. The extraction system is shown for Beam 1 only. In (b), a picture of the superconducting undulator (green) and the D3 dipole (blue) installed on the right-hand side of the long straight section located at Point 4.

3.2 Light extraction system

The light extraction system is a key element of the LHC SR diagnostics and one of the most technologically challenging aspects. It consists of a mirror placed inside the beam chamber that intercepts part of the light and sends it to the beam instrumentation. The geometry of the extraction tank is displayed in Fig. 3.2. The mirror is installed in an extremely harsh environment, in the ultra-high vacuum of the LHC beam pipe and in close proximity to the particle beam. The design has been optimised over the years of LHC operation. The current solution consists of a monolithic fused silica substrate with a fully dielectric reflecting coating. This design minimises the device impedance and thus reduces the impact on beam stability and RF heating, which may significantly degrade the optical quality of the surface [40]. In addition to beam-induced damage, the mirror is also constantly exposed to the high-frequency components of the SR spectrum which may create local blackening or detachment of the reflecting coating, as already occurred in run 2 [19]. The extraction mirror is the most critical optical component to manufacture and represents the limiting factor for the achievable optical performance of the SR monitors. The present mirror features a $\lambda/5$ wavefront error with a 20-10 scratch-dig surface quality, making it a suitable component for both imaging and interferometry applications.

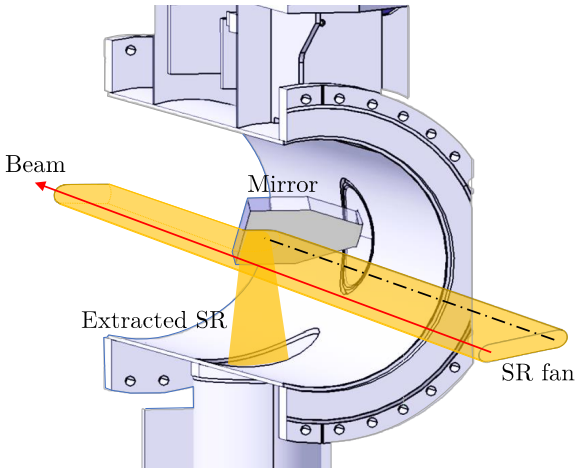

Figure 3.2: Sketch of the LHC synchrotron radiation extraction system. Light emitted by the source devices propagates alongside the particle beam. A tilted mirror inserted in the vacuum chamber intercepts a portion of this radiation and reflects it downward, where the SR diagnostic systems are installed in an optical enclosure under the accelerator beam pipe. The dash-dotted line in figure represents the undulator axis, used as the reference of the SR coordinate system.

In addition to the technological aspects, the extraction mirror is also the main constraint for the angular acceptance of the downstream systems, in particular in the horizontal direction. On the extraction plane, located at $z = 27.4\,\mathrm{m}$, the distance between the beam and the undulator

axis is 34 mm. For machine protection reasons, the edge of the mirror is positioned approximately 22 mm away from the beam. This position provides a safe distance of 20 beam size units at injection energy. As a result, only a portion of the emitted light can be extracted, and the vertical mirror edge behaves as an unavoidable source of diffraction affecting the horizontal direction. On the remaining three sides, the mirror extends beyond the size of the light spot, allowing for the extraction of the entire intensity. The optical acceptance of the extraction system is ultimately limited to a size of 50 mm × 50 mm, corresponding to a physical mirror dimension of 50 mm × 70 mm when projected at an angle of 45°. The mirror centre lies at $x \approx -13$ mm, resulting in a mirror edge located at $x_{edge} \approx 12$ mm on the side facing the beam. Due to the characteristic opening angle of synchrotron radiation, in the order of $1/\gamma$, only a small region of the mirror surface, typically a few millimeters, is effectively used at flat-top energy. However, the mirror surface is almost entirely illuminated by the broad emission of the undulator radiation at injection energy.

3.3 Superconducting undulator

The undulator used for beam diagnostics at the LHC consists of four superconducting poles arranged to create a two-period vertical field with periodicity $\lambda_u = 0.28$ m. The coil assembly and the resulting magnetic profile at the gap centre are illustrated in Fig. 3.3. The main design parameters of the device are listed in Tab. 3.1. The undulator is housed in a cryostat that is directly connected to the adjacent D3, which maintains the superconducting coils at 4.5 K. The assembly of undulator and D3 is shown in Fig. 3.1b.

Parameter	Value	Unit
Period length λ_u	0.28	m
Period number N_u	2	
Operating current (nominal)	400 (450)	A
Operating peak field B_0 (nominal)	4.5 (5)	T
Deflection parameter K	0.064	
On-axis proper wavelength λ_1 at 450 GeV	610	nm
On-axis proper wavelength λ_1 at 6800 GeV	2.7	nm

Table 3.1: Parameters of the LHC superconducting undulator.

Under operating conditions, the undulator generates a peak magnetic field of 4.5 T at the centre of the magnet gap. Despite the strength of the field, the relatively large mass of the protons yields an undulator deflection parameter $K = 0.064 \ll 1$. As a result, the weak

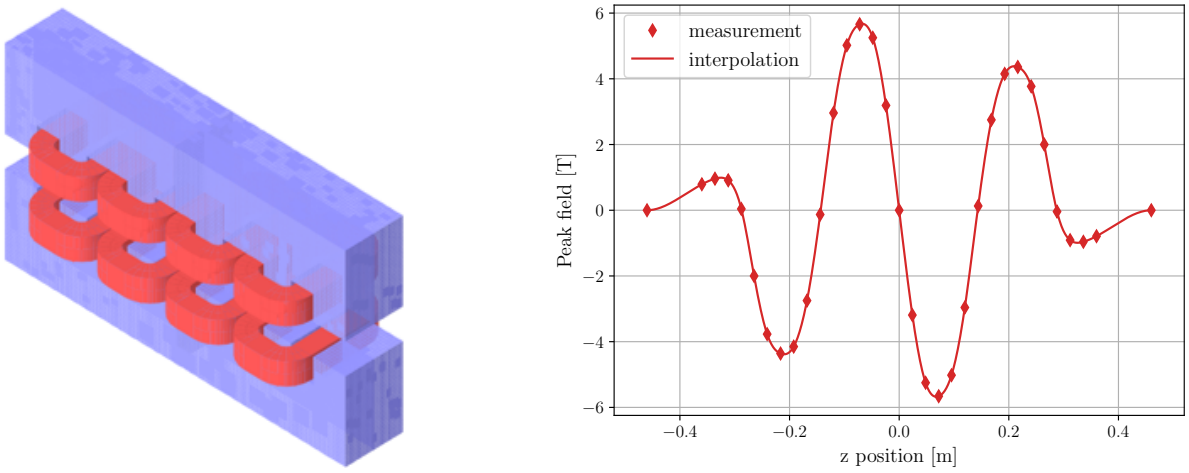

(a) (b)

Figure 3.3: Coil assembly of the LHC superconducting undulator (a) and the corresponding magnetic field profile created at the gap centre (b). The magnetic measurements are interpolated to obtain the continuous field profile implemented in simulations.

magnet approximation discussed in the previous chapter is applicable to this undulator, since the deflection induced by the magnetic field is much smaller than the typical opening angle of the emitted radiation. An important consequence of the weak undulator model is that the spectral and spatial properties of the emitted radiation depend only on the undulator period λ_u and the number of periods N_u. The high magnetic field is necessary to ensure an adequate photon flux but B_0 has no impact on the shape of the radiation spatial distribution and its spectrum.

The spectral distribution of the radiation can be obtained by calculating the square modulus of the weak undulator field, as described in Eq. 2.14. Along the undulator axis ($\vartheta = 0$), the spectrum is peaked at the proper wavelength $\lambda_1 = \lambda_u/2\gamma^2$. The undulator is specifically designed to maximize the synchrotron radiation emission in the visible range at the injection energy. It has a magnetic field period of 28 cm, which corresponds to an on-axis proper wavelength of 610 nm at 450 GeV. According to the weak magnet model, the radiation spectrum is determined by the Fourier transform of the longitudinal profile of the magnetic field. Figure 3.4 shows the on-axis spectrum at injection energy. The spectrum resulting from the numerical simulation of the measured magnetic profile is compared to the analytical spectrum of the corresponding ideal undulator, as defined by Eq. 2.10. The central lobe of the spectral distribution appears similar in both models because it is primarily determined by the undulator periodicity, which does not depend on the exact shape of the magnetic field profile. The asymmetry of the central lobe arises from the presence of two sinc functions in Eq 2.14, where the term dependent on

$\omega + \omega_1$ cannot be neglected due to the limited number of periods of the device. The small number of periods also contributes to the broadening of the main peak in the spectrum. The characteristic width of the peak $\Delta\lambda$ spans a range of a few hundred nanometers, consistent with the estimation $\Delta\lambda/\lambda \simeq 1/N_u$ stated in Eq. 2.16. The two magnetic profiles exhibit significant differences in the tails of the spectrum, where the analytical profile greatly overestimates the intensity decay. This discrepancy can be attributed to the underlying principles of the weak magnet model. The ideal field, defined as a cosine function truncated by a rectangular window, possesses sharper spatial features than the smooth profile of the real undulator field. Since the weak magnet model relates the frequency content of the magnetic field profile to the spectrum of the radiated field, the less intense tails in the spectrum of the real undulator are expected.

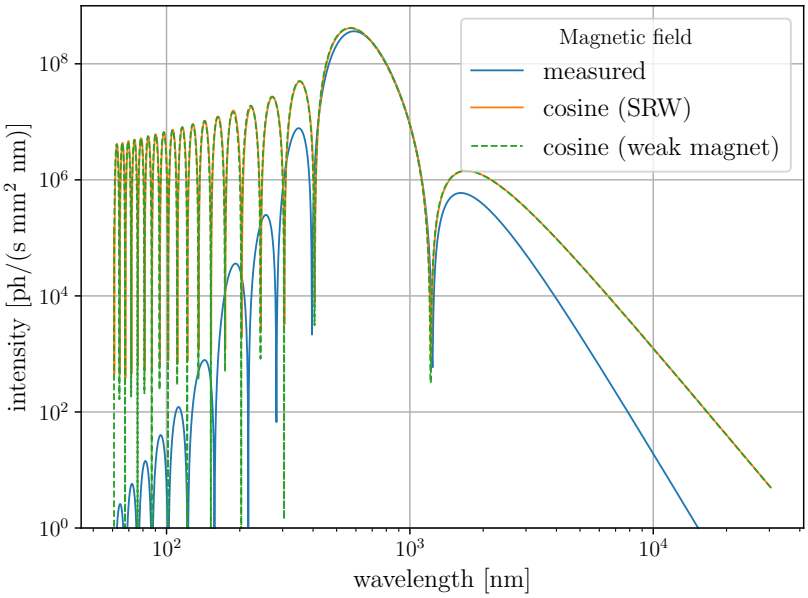

Figure 3.4: Simulation of the on-axis undulator spectrum at injection energy. The measured magnetic field of Fig. 3.3b is used as input for the numerical computation of the spectrum with SRW (blue curve). The result is compared to the spectrum simulated in SRW using the ideal sinusoidal profile defined in Eq. 2.10 (orange curve). The spectrum of the weak undulator is reported (dashed curve), validating the agreement between the numerical SRW simulation and the analytical result of the weak magnet approximation.

The evolution of the undulator on-axis spectrum as a function of the beam energy is reported in Fig. 3.5. As the beam energy increases, the proper wavelength of the undulator decreases to shorter values. Additionally, the on-axis photon flux increases quadratically with the energy due to the weak undulator field being proportional to γ. Between 450 GeV and 800 GeV, the on-axis radiation drifts outside of the visible range and the proper wavelength reaches the far UV domain. Visible undulator radiation can be still observed off-axis, where the undulator period observed

at larger angles produces SR with longer proper wavelength $\lambda \approx (1 + \gamma^2\vartheta^2)/2\gamma^2$. Above 1 TeV, the emission of visible undulator radiation is limited to observation angles that are significantly larger than the acceptance of the extraction system. At this stage, the D3 dipoles become the most intense source of visible synchrotron radiation.

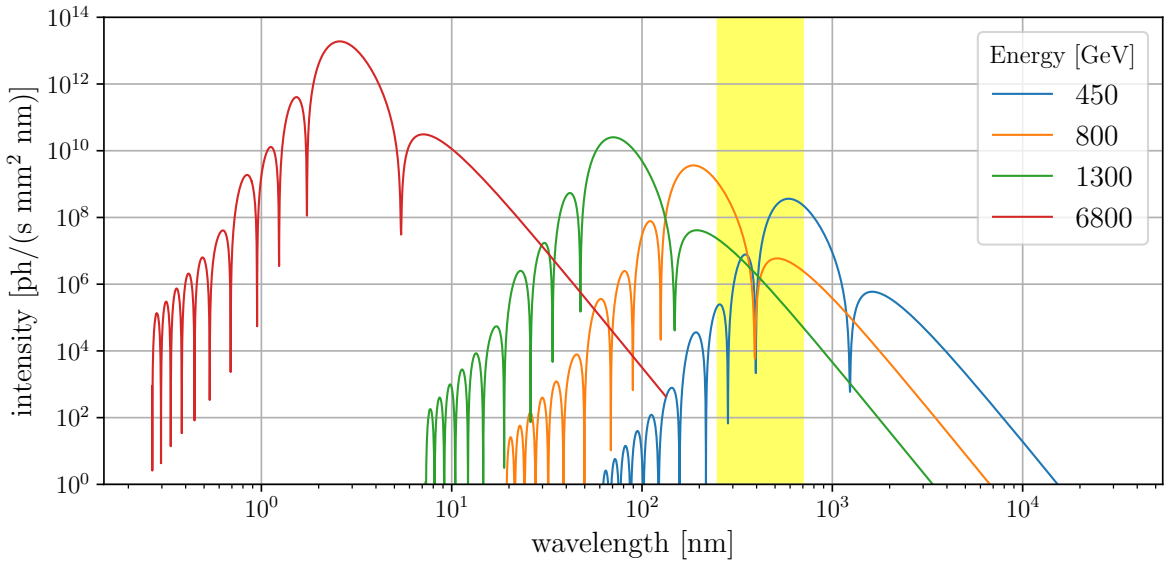

Figure 3.5: Simulation of the on-axis spectrum emitted by the LHC undulator at several beam energies. The yellow band highlights the UV-VIS range currently exploited for SR diagnostics. Notice that in a logarithmic plot, the energy evolution of the radiated spectrum corresponds to a rigid shift of the curve to shorter wavelengths and higher photon fluxes.

At high beam energy, the undulator on-axis emission has its peak at wavelengths as short as a few nanometers. This radiation has the potential to be exploited for accurate diagnostics at flat-top in the soft X-ray domain, for example by means of a pinhole camera [41]. However, it currently acts as a parasitic effect, negatively impacting the lifetime of the extraction mirror. The optical coating is constantly irradiated by a narrow and intense beam of soft X-rays. During LHC run 2, mirrors installed in the system experienced a surface damage caused by a local detachment of the dielectric coating at the location of the undulator axis [19]. Starting from run 3, the undulator is turned off during the energy ramp to mitigate the issue of coating degradation. The device is gradually powered down, and it is completely off by the time the beam has reached the energy of 3.3 TeV. As a consequence, the actual evolution of the spectrum during the accelerator energy ramp should take into account the decrease in intensity caused by the reduction in the device's peak field.

3.4 D3 dipole

The D3 is a special type of superconducting dipole, consisting of two independent single-aperture magnets housed within a cryostat similar to the one used for the LHC main dipoles. The internal structure of this magnet is depicted in the cross-section view of Fig. 3.6 and the properties relevant to synchrotron radiation emission are summarised in Tab. 3.2. The distinctive feature of this magnet is that the deflection of the two beams acts in opposite directions, as required to increase the inter-beam separation. The magnetic field is therefore aligned in the two beam pipes. This configuration imposes certain limitations on the achievable magnetic field strength, resulting in a larger bending radius compared to the main dipoles of the LHC arcs. The larger bending radius has direct implications for the spectral properties of the emitted synchrotron radiation, as the critical wavelength of the dipole is proportional to the bending radius $\lambda_c = \frac{4\pi}{3}\frac{\rho}{\gamma^3}$. The D3 dipole magnet is characterized by a peak field strength of 3.9 T and induces a deflection with a bending radius exceeding 6 km. In comparison, the LHC main arc dipoles generate a higher field of 8.3 T within the gap, resulting in a smaller bending radius of approximately 2.8 km.

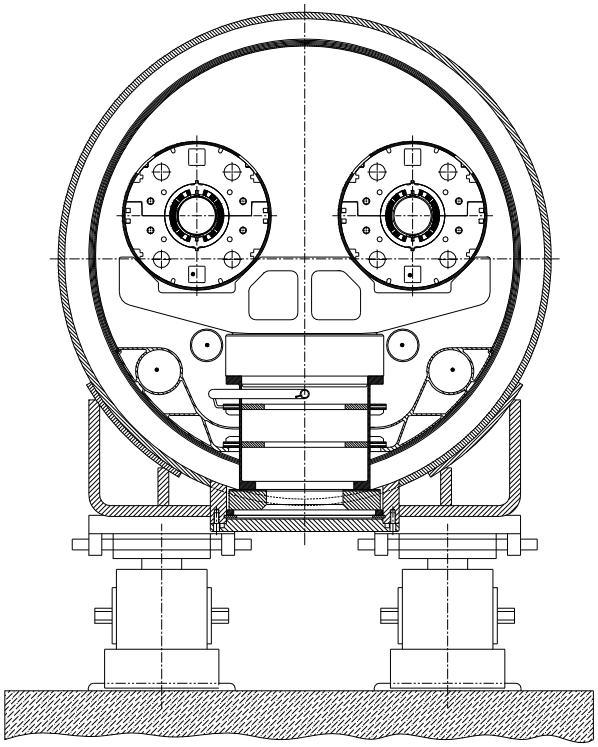

Figure 3.6: Cross-section displaying the internal structure of a D3-type dipole. Illustration taken from the D3 design report [36].

Since no detailed measurements of the magnetic field profile are available for this magnet,

Parameter	Value	Unit
Magnetic length l_{core}	9.45	m
Coil inner diameter d_{coil}	0.08	m
Maximum magnetic field B_0	3.85	T
Bending radius ρ	6013	m
Critical wavelength λ_c at 450 GeV	230	µm
Proper wavelength λ_c at 6800 GeV	66	nm

Table 3.2: Parameters of the D3-type dipole.

we assume a uniform magnetic field ranging for l_{core} with exponential tails of characteristic length $l_{edge} \approx d_{coil} = 80\,\text{mm}$, consistent with the model of Eq. 2.18. This realistic field profile is compared with the ideal hard-edge dipole with a uniform field inside the magnet core which suddenly drops at the dipole edges, with no field tails extending beyond.

The radiation emitted by the D3 dipole is in general more complicated than the weak undulator case, as there is no unique model that comprehensively describes the entire wavefront. Significant differences arise in the radiation emitted when particles traverse the region of the magnet edge compared to the light radiated by the circular motion inside the magnet core. While both forms of radiation share the same physical origin, it is convenient to analyze them separately using the analytical models presented in Sec.2.2 and Sec.2.3 for edge and core radiation, respectively. The distinction between edge and core radiation is a conceptual framework useful to describe some specific features of dipole radiation. In reality, the particle undergoes a continuous transverse acceleration across the entire region of uniform field, and there is no fundamental difference in the emission process between the edge and core locations. The spectral-spatial properties of the D3 dipole are characterized focusing on the D3_R, which provides the main contribution to the high energy radiation in the diagnostics line of the Beam 1. Since the two D3 dipoles of the LHC SR sources are identical, the same considerations apply to the D3_L provided that the different arrangement in the source layout is taken into account. The magnetic device is characterized individually, while the next section is entirely dedicated to the interference effects that arise from the presence of both magnets.

The spatial distribution of the D3 at flat-top energy is shown in the central plot of Fig. 3.9. The distribution exhibits two broad circular spots, centred at $(x, y) = (0, 0)$ and $(x, y) \approx (34, 0)$mm. Between these centres, there is a region characterized by significantly higher radiation intensity and narrower vertical aperture of the light. With reference to the source geometry of Fig. 3.1, the two circular spots are aligned along the entrance and exit axes of the

dipole and they represent the edge radiation contribution of the magnet. The radius of the spot corresponding to the exit edge radiation is smaller since it is closer to the observation plane. The high-intensity region in the centre is the dipole core radiation, emitted tangentially to the beam deflected inside the dipole, which resembles the pattern produced by a sweeping searchlight. Due to the different spatial distribution of core and edge radiation, it is possible to separately study each contribution by properly selecting the observation point.

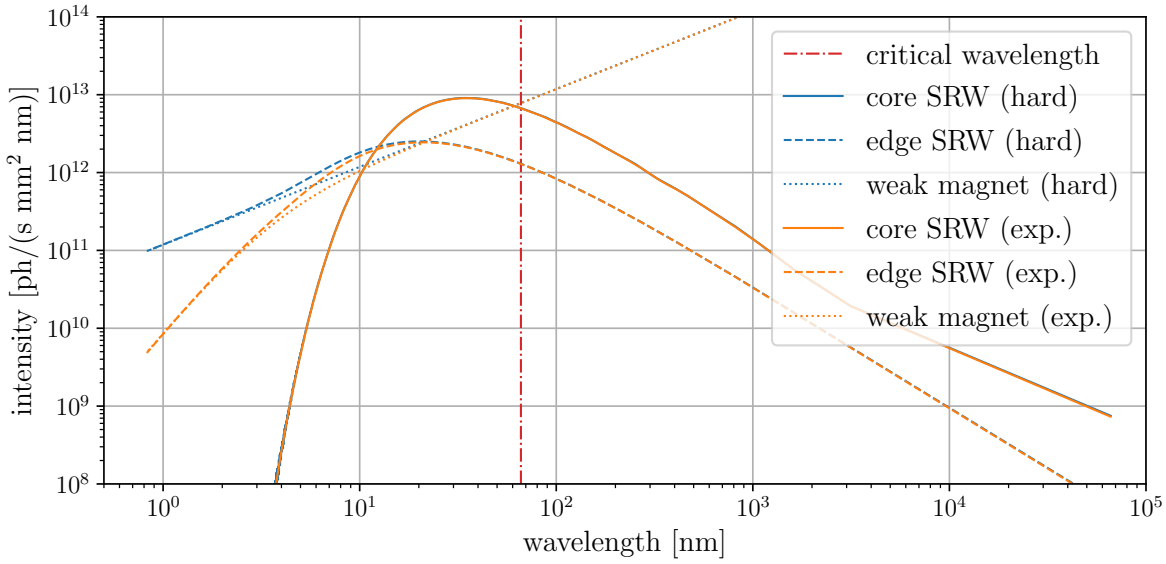

Figure 3.7: Spectra of the $D3_R$ dipole at 6.8 TeV, simulated with a hard-edge model (blue curves) and an exponentially decaying field tail (orange curves). The solid lines describe the spectrum of the radiation emitted from the magnet core whereas the dashed lines are the spectra computed along the axis of the entrance edge. The edge radiation spectrum computed with the weak magnet approximation of Eq. 2.14 is plotted in dashed lines for both models of the fringe field.

Figure 3.7 shows the spectra of dipole SR, simulated in the region of edge and core radiation, and comparing the hard-edge model to the more realistic case of a field profile with exponentially decaying fringe field. Dipole radiation is characterized by a much broader spectral distribution when compared to typical undulator radiation, even in the case of the relatively large spectrum of the LHC mini-undulator. This characteristic is due to the lack of periodicity in the magnetic field, which does not favor the emission of a specific range of frequencies. The spectrum of the core radiation is the typical distribution resulting from the Schwinger's field of Eq. 2.21. The core emission is peaked near the dipole critical wavelength. The spectral distribution exhibits a characteristic tail towards longer wavelengths, and a relatively fast decay as we move towards shorter wavelengths. Despite the asymmetry of the curve, the integrated power on both sides of the spectral distribution is equal due to the higher energy associated with shorter wavelength

photons. The spectrum of the core radiation exhibits a perfect overlap between the hard and exponential models for the edge field. This outcome is expected since the shape of the fringe field has a negligible influence on the properties of the radiation originating from the dipole core.

The distribution changes when simulating the spectrum for the radiation emitted from the magnet edge, obtained by sampling along the direction of the beam entering the dipole. The long wavelength tail of the edge radiation follows a similar trend to the core radiation, but with lower intensity. This is because the deflection under a uniform magnetic field, i.e. the constant part of the step function, still dominates in the long wavelength regime but only half of the magnet contributes to the emission, hence the lower intensity compared to the core spectrum. On the other hand, the edge radiation exhibits a significantly higher intensity in the high frequency region. This is the most distinctive feature of edge radiation and it is perfectly described by the sudden change in the magnetic field, as confirmed by the perfect overlap between the analytical model presented for the edge radiation and the high-frequency limit of the simulated curve. In the edge spectral distribution is it also possible to appreciate the difference between the different fringe field models. The hard-edge profile features the sharpest field profile and therefore provides the most intense radiation at high frequency. The intensity of radiation decreases as the fringe field becomes smoother, such as in the case of an exponential decay of the field. This behavior is consistent with the fact that the modulus of the fringe field modulation factor $f(l_{edge})$ of Eq. 2.20 is always smaller than one.

To complete the characterization of the D3 spectral properties, let us consider the evolution of the spectrum during the accelerator energy ramp. The core and edge curves simulated at various beam energies are reported in Fig. 3.8. Below 1 TeV, there is minimal radiation emitted by the dipole in the visible range. As the energy increases, the high-frequency tail of the edge radiation gradually extends into the visible spectrum and becomes dominant over the undulator radiation. By reaching 1.3 TeV, the dipole radiation is completely dominated by the edge contribution. Above 2 TeV, the visible core radiation becomes significant, and at 3 TeV, the critical wavelength of the dipole reaches the centre of the visible range and core radiation becomes the most intense contribution, although the broader edge radiation remains as background in the peripheral regions of the observation plane. As the beam energy further increases, the critical wavelength drifts beyond the UV range and the light emission in the optical domain remains essentially stable. In contrast to the behavior observed in undulators, the dipole spectrum evolves differently as the beam energy increases. While undulator spectra rigidly shift towards

shorter wavelengths with increasing intensity, in the case of dipoles, the long-wavelength tails remain largely unaffected and the intensity curve expands towards shorter wavelengths. This phenomenon can be interpreted as the additional radiation produced at higher beam energies being predominantly emitted as more energetic photons. The emission at a fixed observation wavelength, longer than the critical wavelength, is marginally affected by further increase of the beam energy. Beyond the energy threshold of 4 TeV, the D3 radiation exhibits minimal changes in the visible domain. This leads to the relevant conclusion that, for wavelengths longer than the critical one, the characteristics of dipole radiation remain essentially constant regardless of variations in beam energy.

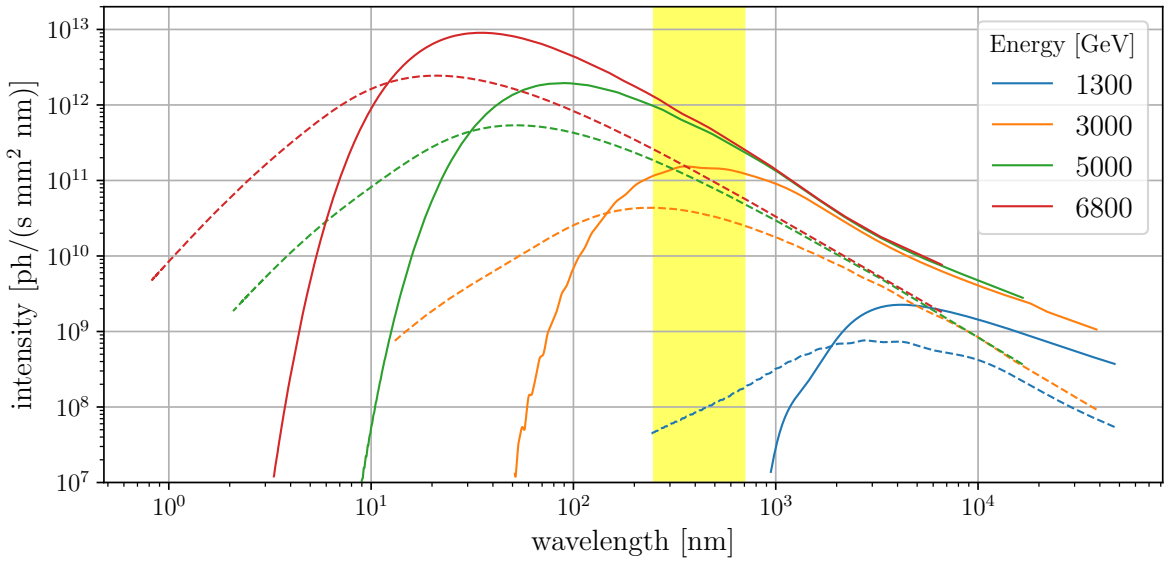

Figure 3.8: Simulation of the spectrum emitted by a D3 dipole at several beam energies. For each energy, the spectrum of the core radiation (solid curves), simulated at the centre of the core radiation region, is compared to the one simulated along the reference undulator axis (dashed curves), representing the edge radiation contribution. The yellow band highlights the UV-VIS range currently exploited for SR diagnostics.

The individual characterization of the D3 dipole is not sufficient to fully characterize the spatial-spectral properties of the LHC SR source at flat-top energy. The presence of two identical dipoles in the source layout introduces interference effects, which produce characteristic features in both the radiation spectrum and spatial distributions.

3.5 Dipole interference effects

The synchrotron radiation emitted by the $D3_L$ originates over 130 m upstream of the extraction mirror. Due to its narrow emission angle of a few milliradians, it traverses unperturbed the RF

cavity section and it is extracted alongside the light from the nearest $D3_R$. As anticipated in Sec. 2.4, the emission from the same particle in different source devices is perfectly coherent under monochromatic conditions. As a result, interference phenomena arise from the coherent overlap of the two D3 wavefronts. Fig. 3.9 illustrates the contributions of each dipole at the extraction plane and the spatial distribution resulting from their overlap.

The contribution from the single $D3_L$ is identical to the $D3_R$ one, thoroughly discussed in the previous section. However, due to the greater distance from the observer plane, the spatial distribution of the $D3_L$ dipole is broader compared to the $D3_R$. Additionally, the two patterns are mirrored due to the opposite bending of the two dipoles. As a result, the interference mainly involves the radiation emitted by the exit edge of the $D3_L$ and the entrance edge of the $D3_R$. The radiation from the cores, despite being much more intense at high energy, does not spatially overlap significantly, resulting in less intense interference effects. The simulated SR intensity, including both dipoles, is depicted in the bottom plot. The extracted light is characterized by three distinct regions: a bright spot of $D3_R$ core radiation, an almost uniform and less intense background of core radiation from the downstream $D3_L$, and a pattern of interference rings centred along the axis of the dipoles' edges. In a regime where edge radiation prevails over the core radiation, such as at lower beam energies or higher observation frequencies, the interference rings become the most prominent feature. The concentric ring pattern originates from the phase difference between the two wavefronts, as calculated in Eq. 2.26. The periodicity of the fringes is determined only by the observation wavelength, while the initial phase of the intensity modulation is influenced by the beam parameters.

The interference between the two D3 dipoles affects also the spectrum of the LHC radiation. Figure 3.10 presents a summary of the edge and core radiation spectra when both dipoles are included in the simulations.

The on-axis spectra have the same intensity distribution as they both represent the central peak of the edge radiation. Light from the $D3_L$ is more attenuated by the larger distance to the observer, hence the different amplitude of the spectrum. The spectrum of the interfering edges is governed by Eq. 2.27 and, in particular, its upper and lower envelopes are given by $I(\lambda)^{\pm} = I_1(\lambda) + I_2(\lambda) + 2\sqrt{I_1(\lambda)I_2(\lambda)}$, being $I_i(\lambda)$ the single-magnet radiation intensity at a given wavelength. The overall spectrum is a modulation of the more intense $D3_R$, because of the intensity imbalance between the two dipoles. The spectrum fluctuates within this envelope with a wavelength-dependent period, in agreement with the interference phase of Eq. 2.26. The

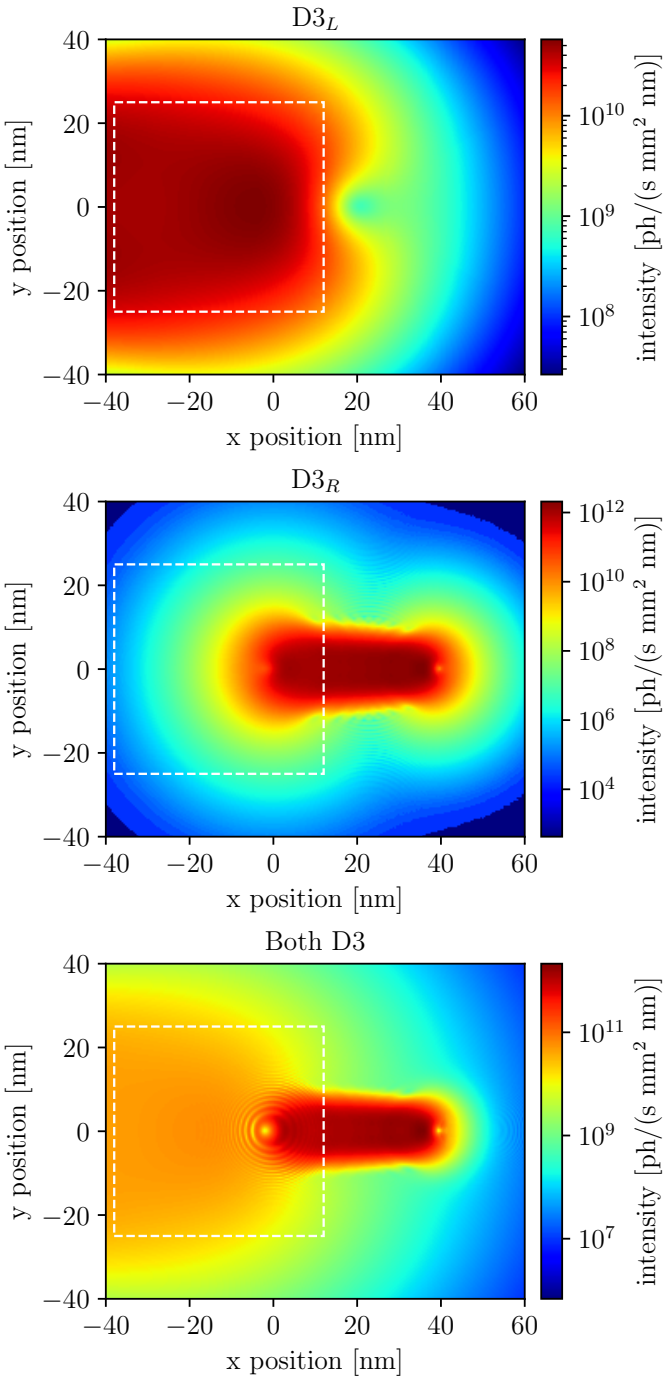

Figure 3.9: Spatial distribution of the radiation emitted by the single $D3_L$ (top), the single $D3_R$ (centre) and both dipoles (bottom), simulated at the plane of the extraction mirror. The beam energy is 6800 GeV and the observation wavelength 400 nm. The dashed square marks the extension of the extraction mirror, which defines the acceptance of the SR monitors. The colour map is in logarithmic scale to cope with the high dynamic range of the intensity distribution.

interference effect is conceptually the same for the spectra of the core radiation. The difference is that the core radiation of the two dipoles is not spatially overlapping as the region of core radiation from the $D3_R$ corresponds to a peripheral region of the edge radiation of the $D3_L$. The two contributions exhibit different spectra and, as a consequence of the scarce spatial overlap,

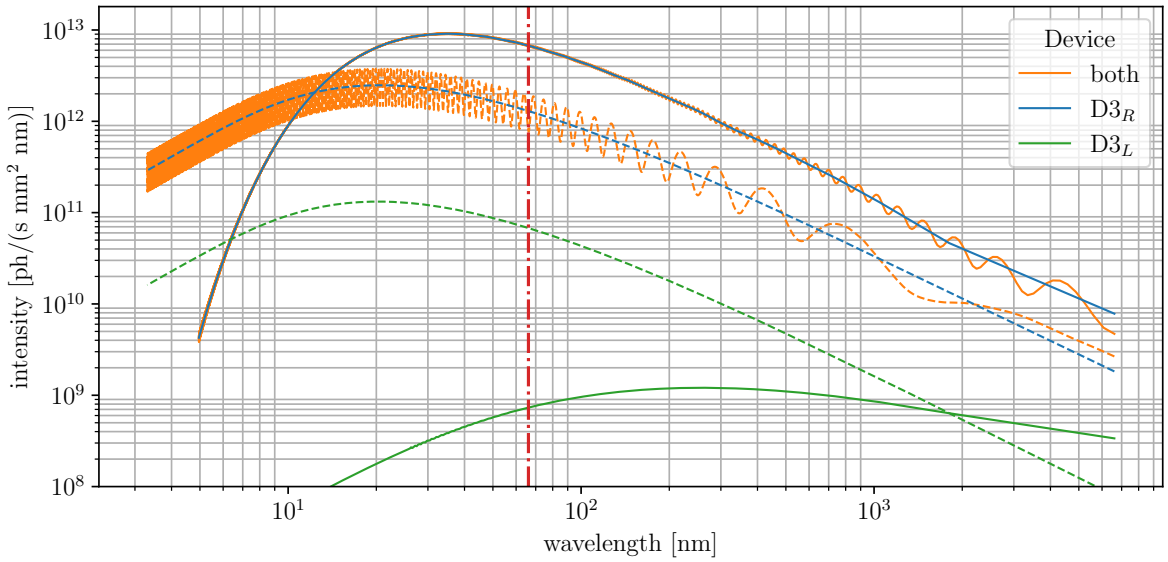

Figure 3.10: Simulation of the SR spectra of the D3 dipoles at 6.8 TeV. Solid curves refer to the spectrum computed at $(x, y) = (14, 0)$ mm, corresponding to the region of core radiation from the $D3_R$. Dashed curves are simulated on-axis and represent the spectrum of the edge radiation for both magnets. The curves computed individually for each magnet are reported for comparison. The vertical red dashed line marks the radiation critical wavelength.

the modulation effect of the $D3_L$ is much less significant than in the on-axis region.

To conclude this section on dipole interference effects, it is important to address the experimental conditions necessary for observing this phenomenon. A rigorous treatment of this problem involves the study of the radiation temporal coherence, which will be presented in more detail in the Sec. 4.1. Here, we provide a concise overview of the concept and present a practical criterion for observing interference fringes. The light emitted by the upstream source reaches the observer before the light radiated by the second source, due to the slower particle propagation in the straight section between the magnets. Interference occurs only if the correlation between the two emissions is preserved throughout the propagation. In the case of perfectly monochromatic radiation, this condition is automatically satisfied as the correlation is fully preserved along an infinitely extending sinusoidal wave. However, in reality, the finite bandwidth of the radiation leads to a reduction in correlation. The propagating radiation maintains its correlation for a distance on the order of $\lambda^2/\Delta\lambda$, where $\Delta\lambda$ represents the bandwidth of the radiation [42, p. 356]. To observe interference effects, it is necessary for this distance to be greater than the optical path difference between the radiation from the two sources. The optical path difference can be directly determined from the phase difference at the observer plane, as presented in Eq. 2.26,

and can be expressed as

$$\Delta l \approx \frac{L}{2\gamma^2} + \frac{r_\perp^2}{2\bar{r}_{p,2}(L + \bar{r}_{p,2})} L. \tag{3.1}$$

With realistic values for parameters $\gamma \approx 2000$, $L \approx 100\,\text{m}$, $r_{p,2} \approx 30\,\text{m}$, and a typical observation range of $r_\perp \approx 10\,\text{mm}$, the optical path difference yields approximately 1.5 µm. At a typical visible wavelength of 500 nm observed with a filter of 5 nm bandwidth, the radiation correlation is preserved for a distance in the order of 50 µm. In this typical scenario, interference effects between the two magnets can be observed. The interference persists at higher beam energies since the optical path difference decreases due to the shorter delay caused by beam propagation. However, it is worth noting that if a bandpass filter is not used and the synchrotron radiation is directly observed on a viewing screen, the broad spectrum of the dipole radiation leads to a much shorter correlation length and the interference effects are completely suppressed.

3.6 Polarization effects

The spatial distribution of synchrotron radiation significantly depends on the selected polarization component. The majority of the radiation intensity is emitted with a polarization parallel to the orbit plane, where the transverse deflection takes place. However, for an observer positioned outside the orbit plane, the apparent motion of the particles includes a non-zero vertical projection, resulting in the emission of vertically polarized radiation. The spatial distributions of the two transverse polarization components, simulated at injection and flat-top energies, are reported in Fig. 3.11.

At injection energy, the undulator radiation is strongly polarized along the horizontal direction, with a two order of magnitude less intense vertical polarization. In practice, the vertical polarization component can be neglected at injection energy. At high beam energy, the typical features of edge and core radiation are clearly distinguishable in both polarisation components as well as the fringes created by the two dipole interference. In the region of core radiation, the light distribution in the vertical direction follows the Schwinger profiles of Fig. 2.5. At flat-top energy, the light profile is broader than the Gaussian approximation with $1/\gamma$ opening angle because the dipole critical wavelength of 66 nm, is shorter than visible wavelengths. Additionally, the spatial distribution of the unpolarized light exhibits significant secondary lobes due to the vertical polarization component, symmetric with respect to the orbit plane. These lobes are clearly visible in Figure 3.11d. Quantitatively, the vertical polarization of the core radiation in

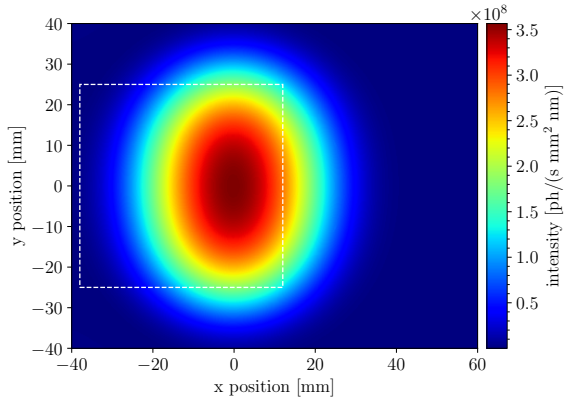

(a) Horizontal polarisation at 450 GeV.

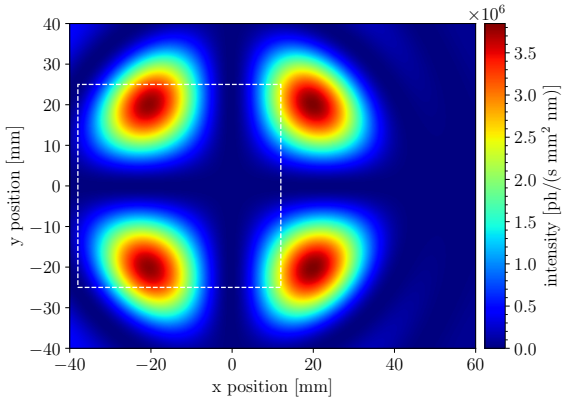

(b) Vertical polarisation at 450 GeV.

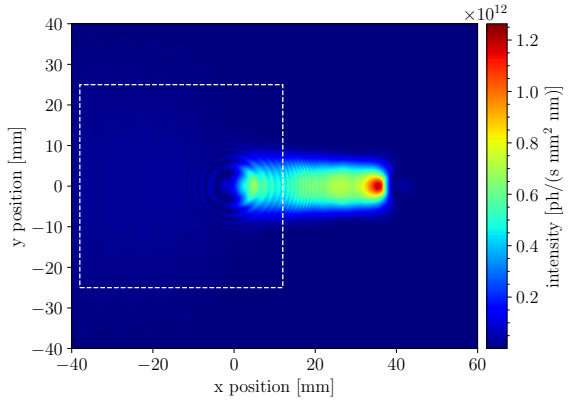

(c) Horizontal polarisation at 6800 GeV.

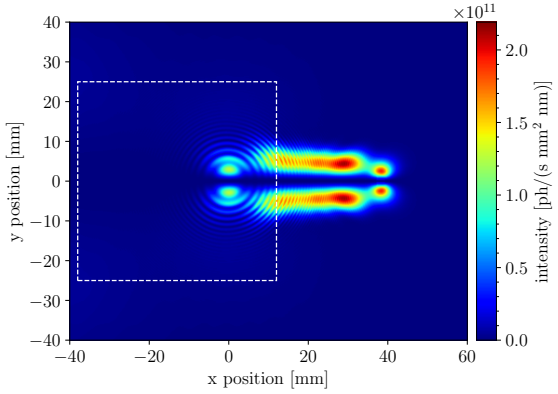

(d) Vertical polarisation at 6800 GeV.

Figure 3.11: Spatial distribution at injection and flat-top energies, computed separately for the horizontal and vertical polarization components. Injection distributions are simulated at the undulator proper wavelength of 610 nm while at flat-top the simulation wavelength is 400 nm. The white dashed square defines the acceptance of the extraction mirror.

the visible domain is only slightly weaker than the horizontal polarization, with a difference of less than an order of magnitude. Interferometric measurements require a defined polarization state, which cannot be achieved with the intrinsic horizontal polarization of the light at flat-top energy alone. Therefore, a linear polarizer is necessary to fully suppress the vertical component.

Finally, the flat-top intensity distributions exhibit a distinct characteristic of the $D3_R$ core radiation. Moving from the region of the entrance edge to the exit edge, the radiation intensity increases while the vertical width decreases. This behavior can be described by the "sweeping searchlight" analogy, where the emitted light corresponds to different longitudinal positions along the dipole. This allows to define an effective source distance for the longitudinally undefined position of the $D3_R$ source. This finding is particularly useful for interferometry, where a well-

defined distance of the source is required to retrieve the information on the source transverse distribution.

3.7 Finite emittance beams

The results discussed in the previous sections rigorously describe the radiation emitted by a filament beam travelling along the nominal accelerator orbit. A real accelerator beam comprises many particles organized in bunches, characterized by finite longitudinal and transverse extensions. In general, both distributions impact on the properties of the emitted synchrotron radiation [43, p. 30].

The longitudinal bunch length determines the correlation properties of radiation from different particles[1]. If the bunch is shorter than the observation wavelength, the radiation emission simultaneously occurs for all the particles and the field intensity is the coherent sum of the single particle fields, proportional to the square of the number of particles. Conversely, if the bunch length is much longer than the wavelength, the radiation from each particle has a random initial phase and the total wavefront is proportional to the particle number, as an incoherent sum. This regime in which there is no correlation between the radiation emitted by different particles is commonly known *incoherent synchrotron radiation*. Given the nominal LHC bunch length of $\sigma_l \approx 1\,\mathrm{ns}$, SR in the visible domain is always incoherent and the radiation intensity scales linearly with the bunch population.

On the other hand, the transverse distribution of the particles determines the spatial coherence properties of the SR. This subject will be discussed in depth in the next chapter, dedicated to this property essential to SR interferometry. In this paragraph, we briefly discuss the impact of a finite transverse emittance on the spatial distribution of emitted SR. Under the aforementioned assumption of incoherent SR, the total beam intensity is the sum of the single-particle contribution, shifted and titled according to the (x, x', y, y') coordinate of the particle in the transverse phase space. The result is essentially a convolution of the single-particle radiation pattern over the transverse distribution of the beam, propagated to the observation plane. This equivalence is rigorous as long as no quadrupoles are present in the beamline, ensuring that the centroids of the light distribution propagate in the same manner as the beam particles. The finite emittance beam features a smoother light distribution compared to the filament beam,

[1] Notice that the correlation discussed here, related to the longitudinal bunch length, is different from the correlation between the radiation emitted by the same particle in different magnetic devices, as mentioned discussing the dipole interference effects in Sec. 3.5.

with the sharp spatial features blurred by the convolution operation. This effect is negligible for undulator radiation at injection energy, due to the already uniform single-particle pattern. However, it becomes more evident in the case of dipole radiation, especially for the fringe pattern of two-dipole interference. Figure 3.12 illustrates the impact of a finite transverse emittance on the spatial distribution of synchrotron radiation at flat-top energy.

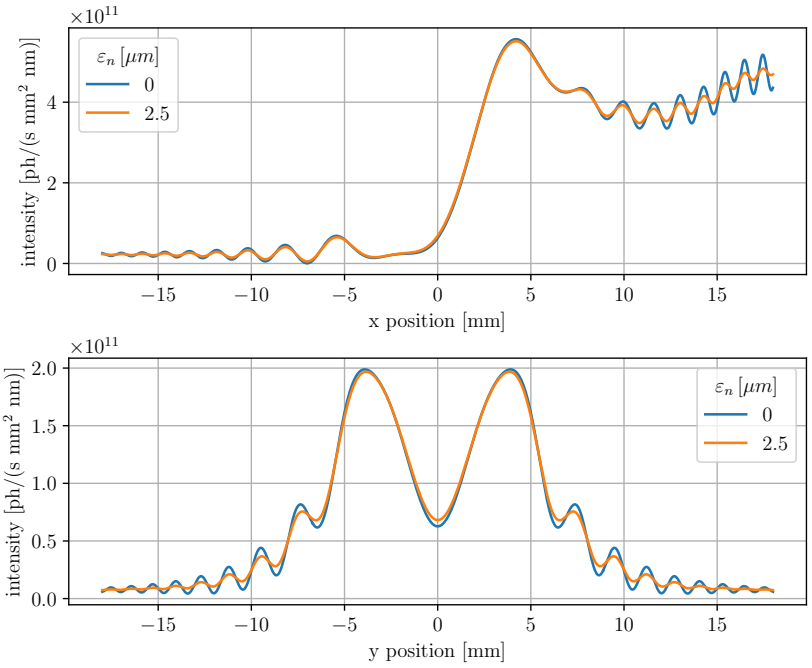

Figure 3.12: Cross-cuts of the SR intensity distribution simulated at a beam energy of 6800 TeV and observation wavelength $\lambda = 400\,\text{nm}$. The zero-emittance case (single particle or filament beam) is compared to a beam with the nominal LHC 2.5 µm normalised emittance.

As expected, the convolution effects have a negligible impact in regions where the initial single-particle distribution is already smooth. However, they noticeably dampen the high-frequency fluctuations of the interference pattern. The reduction in fringe contrast due to the beam emittance can be exploited for non-invasive transverse diagnostics in cases where the source radiation displays sufficiently sharp interference effects [44]. In the case of the LHC, the significant spacing between dipoles results in dipole interference fringes that cause only a mild modulation of the more intense D3_R distribution. The fringes at zero emittance already have a relatively low contrast, making the technique insufficiently sensitive to resolve the emittance-dependent loss of contrast.

3.8 Spatial distribution evolution during the energy ramp

In this section, we analyze the evolution of the SR spatial distribution as a function of beam energy. During the accelerator energy ramp, the emitted radiation undergoes significant changes, transitioning from the regime dominated by the undulator at injection energy to the predominance of dipole radiation as the beam passes the 2 TeV energy level. Special attention is given to the transition between these two regimes, which poses a challenging scenario for synchrotron radiation-based diagnostics.

The evolution of the spatial distribution of synchrotron radiation is illustrated in Fig. 3.13. The figure presents a comparison between the simulated SR distribution at various beam energies and the images of the extracted light, captured by a camera on a viewing screen during an accelerator energy ramp. The observation wavelength is fixed at 560 nm, which is the primary operating wavelength of the synchrotron radiation interferometer. In Fig. 3.14, the evolution of the photon flux, integrated over the extraction acceptance, is reported for various wavelengths within the UV-VIS range, of interest for the whole family of SR monitors.

At injection energy, the 560 nm observation wavelength is close to the undulator on-axis proper wavelength and the spatial distribution is a bright spot of light with the maximum emission along the undulator axis. Due to the limited number of periods of the LHC undulator, the radiation has a rather broad opening angle and the most of the extraction acceptance is illuminated. As the energy increases, the on-axis proper wavelength drifts to shorter values and the resonance condition is satisfied at larger observation angles, according to Eq. 2.15. The on-axis region of the intensity spatial distribution is depleted and the amount of light available for diagnostics drops, as confirmed by the steep decrease of the integrated photon flux of Fig. 3.14. At 800 GeV, the main lobe of the undulator radiation is outside of the extraction acceptance. Nevertheless, the central region is illuminated by the secondary lobe of the sinc function of the undulator spectral distribution. This is consistent with the spectrum simulation of Fig. 3.5. In terms of absolute intensity, although the increased energy produces more intense radiation, this secondary peak is a factor of 50 less intense than the original on-axis emission at 450 GeV. The undulator radiation intensity monotonically decreases after this energy value as no other relevant peaks are present in the spectrum. In addition to the intrinsic decrease due to the spectral properties of undulator radiation, the available light is also reduced by the ramp-down of the device current, performed to mitigate the undulator damage to the extraction mirror

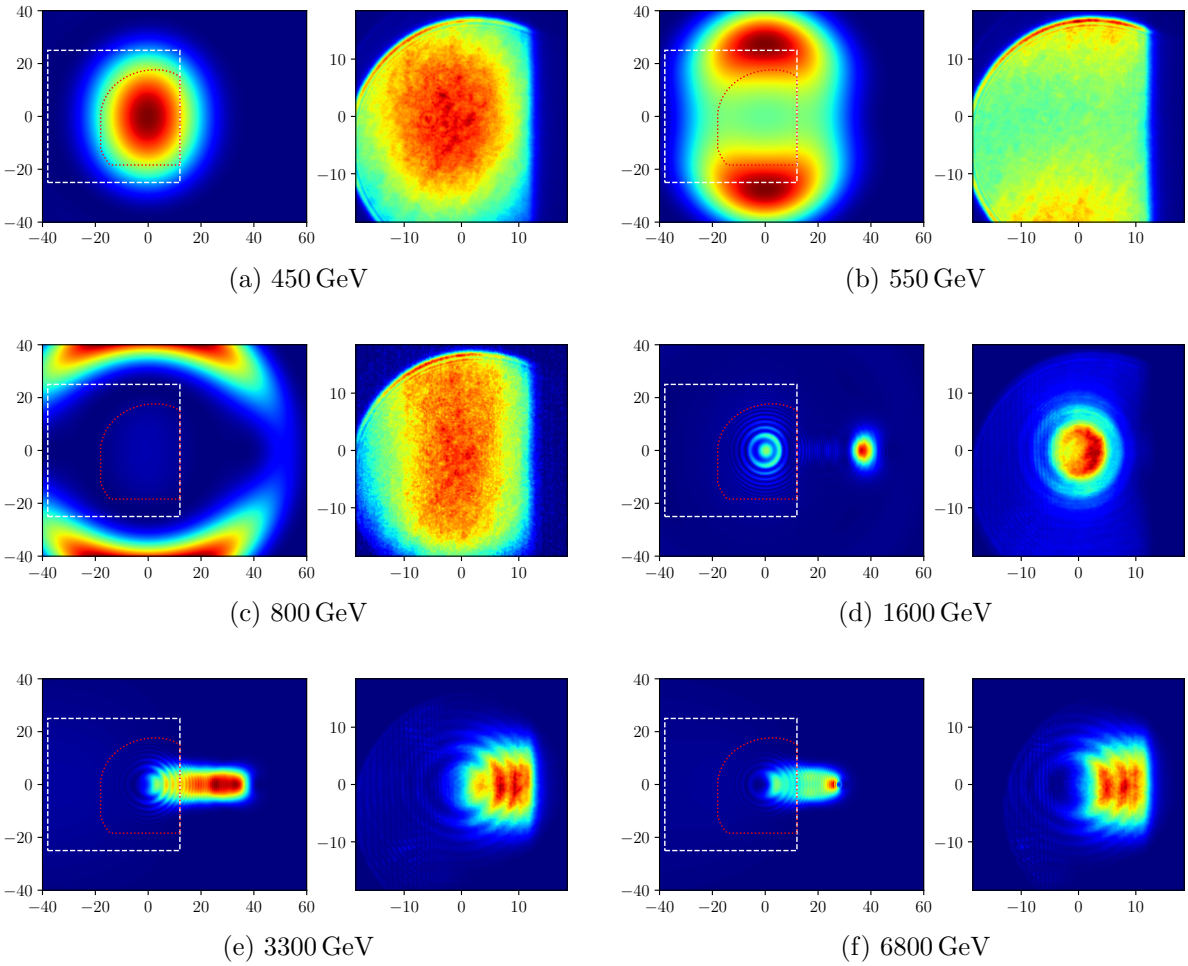

(a) 450 GeV (b) 550 GeV

(c) 800 GeV (d) 1600 GeV

(e) 3300 GeV (f) 6800 GeV

Figure 3.13: Evolution of the SR spatial distribution during the accelerator energy ramp. For some relevant values of the beam energy, the intensity map simulated with SRW (left) is compared to the one observed with a camera on a white screen (right). The simulation and observation wavelength is 560 nm. The white dashed square in the simulation marks the extraction mirror acceptance. The experimental images are further limited by the acceptance of a circular 50 mm bandpass filter, required to have a quasi-monochromatic observation. The effective aperture of the experimental observation is reported, for comparison, as a dotted red path on the simulated distribution. Simulated and observed intensities are not directly comparable as the colour scale is adapted to the full dynamic range of each picture. The position axes are in units of mm for all plots.

coating at high beam energies. Synchrotron radiation diagnostics in the energy range just below 1 TeV are limited by the available amount of light and the fact that most of this radiation is emitted at the peripheral region of the system's acceptance.

Above 2 TeV, the D3 dipoles become the brightest source of light in the visible domain. Light from the dipoles initially appears in form of edge radiation, due to the harder spectrum compared to the core contribution. Around 1.6 TeV, the on-axis radiation from the dipoles equals the photon flux of the undulator at injection energy. The spatial distribution in the regime of pure edge radiation is displayed in the picture corresponding to 1.6 TeV. The on-axis

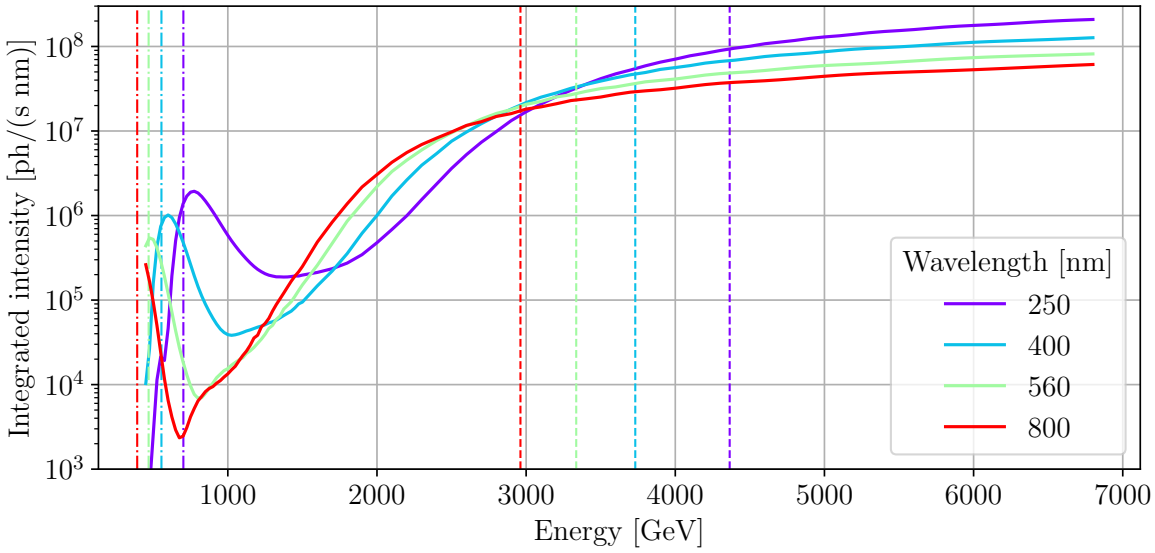

Figure 3.14: Evolution of the photon flux emitted by the LHC source, integrated over the full acceptance of the extraction mirror, simulated at various visible wavelengths. The energy at which the wavelength is the proper wavelength of the undulator and the critical wavelength of the dipole is marked by vertical dash-dotted lines and dashed lines respectively.

region features the concentric rings due to the interference between the two D3 edges. Radiation from the exit edge of the $D3_R$ can be observed in the simulated spatial distribution. This region is not affected by interference because radiation from the exit edge of the $D3_R$ does not spatially overlap with other emissions. The radiation emitted from the exit edge of the $D3_R$ is not practically useful since it cannot be extracted due to its proximity to the beam. The dipole interference pattern is rapidly evolving in this regime. Recalling the expression for the phase difference of Eq. 2.26, the on-axis phase of the interference pattern decays as L/γ^2. The result is a pattern of concentric rings characterised by a fixed periodicity, dictated by the observation wavelength, and a rapidly varying initial phase. This situation persists until this phase term due to the dipole separation reduces to a sufficiently small value and the fringe pattern stabilizes.

Finally, the last major change in the SR distribution is the appearance of core dipole radiation that fills the space gap between the two edge regions. Figure 3.13 reports the interesting case of 3.3 TeV, corresponding to the beam energy at which the dipole critical wavelength matches the observation wavelength. The extracted portion of SR remains significantly affected by the dipole interference effects. The average vertical profile is Gaussian, characterised by an opening angle of $1/\gamma \approx 280\,\mu\text{rad}$. Above the critical energy, the light distribution remains relatively stable. The spatial distribution shows a behaviour similar to the one noticed for the dipole spectrum. An energy increase affects the situation at short photon wavelengths leaving almost unchanged the

distribution at wavelengths longer than the critical one. This argument provides an explanation for the similarity between the simulated (and observed) light distribution at 3.3 TeV and the final distribution at flat-top energy. It also clarifies why the curves of the integrated photon flux exhibit a flat trend above the energy at which the observation wavelength matches the dipole critical wavelength. In this regime, the most noticeable change is the deviation of the vertical profile of the core radiation from the Gaussian distribution to a flatter profile described by the Schwinger functions. However, despite this change in shape, the vertical opening angle remains almost unchanged. This is consistent with the low-frequency trend of Eq. 2.23, as the light divergence does not depend on γ at a fixed observation frequency.

The example discussed in this paragraph focuses on the SR distribution at 560 nm since most of the interferometric measurements presented in this thesis are conducted at this wavelength. However, the considerations regarding the SR evolution as a function of beam energy can be extended to all wavelengths. The only notable difference is the energy at which the reported turning points occur, which varies depending on the specific observation wavelength, and are essentially determined by the proper wavelength of the undulator and the critical wavelength of the dipoles.

In conclusion, it is important to emphasize the dynamic nature of the synchrotron radiation emitted by the LHC source throughout the accelerator energy ramp. This mutability poses significant challenges for all SR-based diagnostics. At present, the SR telescopes are unable to provide reliable beam size measurements during the energy ramp. Emittance measurements in the ramp are only available in low-intensity fills, when the wire scanners are available. The ability to accurately measure beam sizes during the energy ramp becomes a crucial requirement for any candidate instrument for transverse diagnostics. Despite its potential advantages, SR interferometry encounters similar challenges as SR imaging due to the complex nature of the LHC source. Consequently, achieving accurate measurements during the energy ramp remains a persistent challenge.

Chapter 4

Spatial coherence properties of the LHC synchrotron radiation source

This chapter aims to comprehensively investigate the coherence properties of the synchrotron radiation (SR) emitted by the LHC source, focusing on their relevance for diagnostic applications in interferometric techniques. The concept of optical coherence is introduced in space-time domain, where it naturally emerges as a correlation within the radiated field. The fundamental quantities for characterizing spatial and temporal coherence are rigorously defined and compared with their counterparts in the space-frequency domain, commonly discussed in simulations and theoretical models. The following sections describe how the coherence state of an optical field originates from the properties of the source, emphasizing the dependence on the source transverse distribution. The Van Cittert and Zernike (VCZ) theorem is presented as a fundamental model that relates the spatial coherence of a field with the transverse profile of the radiating source. The quasi-homogeneous model is then introduced as a generalization of the VCZ theorem to a wider class of light sources, including relevant cases of SR emitted by relativistic beams. Finally, the chapter presents the results of numerical simulations performed to accurately quantify the LHC SR degree of coherence. These studies aim to investigate the applicability of the VCZ theorem as a model for retrieving the transverse beam size from the coherence of the emitted SR.

4.1 Optical coherence

In optics, coherence is the study of the correlation between different points of a wavefront. The coherence of a wavefront is related to its tendency to exhibit interference effects. Constructive or destructive interference of electromagnetic waves can occur only if the interfering fields are sufficiently correlated. Optical coherence is commonly defined using the concepts of *temporal* and *spatial* coherence. Temporal coherence refers to the correlation properties of a signal as it evolves over time, while spatial coherence involves the correlation between different points on a wavefront sampled at the same instant in time. In practice, all sources of light are characterized by finite spatial and temporal coherence, which means that interference effects eventually vanish over a wavefront area that is too large or a time delay that is too long. Two quantities are introduced to quantify the coherence of a light wavefront: the *coherence length*[1] and the *coherence area*.

The coherence length serves as a measure of temporal coherence. It represents the distance over which a wavefront can propagate without experiencing a significant loss of correlation. This concept was previously introduced in Sec. 3.5 to discuss the conditions necessary for observing interference effects between two sources of synchrotron radiation. The coherence length can be determined based on the spectral bandwidth of the light, following the relation $l_{coh} \approx \lambda^2/\Delta\lambda$ [45]. Despite being a crucial property of an optical field, temporal coherence is marginally addressed in the following as it does not convey direct information about the transverse distribution of a source of light. The primary focus of this thesis is on spatial coherence. In analogy with the coherence length, the coherence area describes the spatial extent of a transverse region on the wavefront where the field correlation is preserved. The objective of this chapter is to discuss the relationship between the transverse distribution of a source of light and the coherence properties of the emitted field and present the fundamental results that allow inferring the source transverse size from the radiation coherence area. It is worth emphasizing that in real experiments, both temporal and spatial coherence coexist and jointly contribute to the loss of interference capability in the radiation. Therefore, it is crucial to minimize the impact of temporal coherence and ensure that it does not affect the measurement of spatial coherence. The coherence length is a useful parameter in this regard, as it provides an immediate estimation of the temporal coherence and defines the conditions under which it can be neglected. The results presented in the following sections pertain to the theory of second-order coherence of scalar fields, where the term "second-

[1] Depending on the context, it may be more convenient to define a *coherence time* τ_{coh}. The two quantities are equivalent as they are one-to-one related by the speed of light as $l_{coh} = c\tau_{coh}$.

order" refers to the correlations between two variables, specifically space-time or space-frequency. Additionally, in scalar fields, the polarization components are treated individually, excluding any cross-polarization interference.

4.1.1 Coherence in space-time domain

To quantify optical coherence and relate it to physical observables, we need to introduce the relevant variables that characterize the correlation properties of an optical field.

Let $E(t, \mathbf{r})$ be the complex representation of a scalar component of an optical field at the time instant t and spatial point $\mathbf{r}$. This representation encompasses both the phase and amplitude information of the field. The real part of $E(t, \mathbf{r})$ corresponds to the observable quantity that characterizes the radiation field and can be ideally measured using a detector with infinite time and spatial resolution. If the process is stationary, the optical intensity associated with the field $E(t, \mathbf{r})$ is defined as [42, p. 562]

$$I(\mathbf{r}) = \langle E(t, \mathbf{r}) E^*(t, \mathbf{r}) \rangle. \tag{4.1}$$

Typically, radiation emission processes are ergodic, meaning that the time-average of the field corresponds to the ensemble-average of multiple realizations of the field generated by the individual emitters that constitute the source. Under this assumption, the notation $\langle \dots \rangle$ represents either average operation. Let us now isolate two points of the wavefront, $E(t, \mathbf{r_1})$ and $E(t, \mathbf{r_2})$, and compute the intensity resulting from the superposition of the propagated fields at a point $\mathbf{r}'$. This situation can be created by placing two narrow pinholes in $\mathbf{r_1}$ and $\mathbf{r_2}$ and detecting the intensity at the point $\mathbf{r}'$ on a screen downstream. The resulting field reads

$$E(t, \mathbf{r}') = K_1 E\Big(t - \frac{s_1}{c}, \mathbf{r_1}\Big) + K_2 E\Big(t - \frac{s_2}{c}, \mathbf{r_2}\Big), \tag{4.2}$$

where $s_i = |\mathbf{r}' - \mathbf{r_i}|$ is the distance from the two sampled points and K_i are pure imaginary numbers that describe the propagation from $\mathbf{r_i}$ to $\mathbf{r}'$, which can be derived applying the Huygens-Fresnel principle [42, p.417]. Recalling Eq. 4.1, the optical intensity associated with the resulting field becomes

$$I(\mathbf{r}') = |K_1|^2 I(\mathbf{r_1}) + |K_2|^2 I(\mathbf{r_2}) + 2|K_1 K_2| \,\mathrm{Re}\Big\{\Big\langle E\Big(t + \frac{s_2 - s_1}{c}, \mathbf{r_1}\Big) E^*(t, \mathbf{r_2})\Big\rangle\Big\}. \tag{4.3}$$

The stationarity of the process implies that the only significant time dependence is the time difference due to the propagation, $\tau = (s_2 - s_1)/c$, irrespective of the specific absolute time instance at which the fields are sampled. Let us introduce the quantity

$$\Gamma_{12}(\tau) \triangleq \left\langle E\left(t + \frac{s_2 - s_1}{c}, \mathbf{r_1}\right) E^*(t, \mathbf{r_2}) \right\rangle, \tag{4.4}$$

which can be conveniently normalized by an intensity factor

$$\gamma_{12}(\tau) \triangleq \frac{\Gamma_{12}(\tau)}{\sqrt{I(\mathbf{r_1})I(\mathbf{r_2})}}. \tag{4.5}$$

Redefining $I_i(\mathbf{r}') = |K_i|^2 I(\mathbf{r_i})$ as the intensity from the field in $\mathbf{r_i}$ propagated to $\mathbf{r}'$, Eq. 4.3 can be rewritten in more compact form as

$$I(\mathbf{r}') = I_1(\mathbf{r}') + I_2(\mathbf{r}') + 2\sqrt{I_1(\mathbf{r}')I_2(\mathbf{r}')}\,\mathrm{Re}\{\gamma_{12}(\tau)\}. \tag{4.6}$$

This equation is a prominent result of optics and it is referred to as *general interference law* of stationary fields. Under very general conditions, it states that the superposition of two optical fields can be interpreted as the sum of the two fields' intensities, modulated by an interference term. The key quantity to describe the interference effect is $\Gamma_{12}(\tau)$ which is defined as the *mutual coherence function* of the field. It represents the correlation of the wavefront between the two points $\mathbf{r_1}$ and $\mathbf{r_2}$ over a time interval τ [46]. Its normalized form $\gamma_{12}(\tau)$, known as the *complex degree of coherence*, satisfies the inequality conditions $0 \leq |\gamma_{12}(\tau)| \leq 1$. A value of $|\gamma_{12}(\tau)|$ equal to zero indicates complete lack of correlation, or incoherence, between the wavelets originating from the sampled points. In this case, the intensity resulting from the field superposition reduces to the sum of the two independent field intensities. On the other hand, a value of $|\gamma_{12}(\tau)|$ equal to unity signifies perfect correlation, or coherence, between the wavelets. The intensity is then bounded by $I(\mathbf{r}')^{\pm} = I_1(\mathbf{r}') + I_2(\mathbf{r}') \pm 2\sqrt{I_1(\mathbf{r}')I_2(\mathbf{r}')}$ and exhibits oscillations based on the phase of the complex quantity $\gamma_{12}(\tau)$. In cases where the correlation between the wavefronts is neither fully coherent nor completely incoherent, the fields are referred to as *partially coherent*. In such intermediate situations, the intensity profile exhibits oscillations that are confined within narrower envelope functions given by

$$I(\mathbf{r}')^{\pm} = I_1(\mathbf{r}') + I_2(\mathbf{r}') \pm 2\sqrt{I_1(\mathbf{r}')I_2(\mathbf{r}')}|\gamma_{12}(\tau)|. \tag{4.7}$$

Equation 4.6 is a generalization of the interference law presented in Eq. 2.27 to describe the interference between wavefronts emitted by the same particle as it traverses different magnetic devices. In the case of Eq. 2.27, the elemental sources were assumed to be fully coherent, since the particle preserved the correlation during propagation. The phase was dictated by the propagation delay $\Delta\phi = kc\tau$, which corresponds to a "pure phase" complex degree of coherence $\gamma_{12}(\Delta\phi) = e^{i\Delta\phi}$, whose real part reduces to $\cos(\Delta\phi)$. In the context of more general interference between partially coherent fields, the quantity $\gamma_{12}(\tau)$ assumes complex values. Its absolute value provides a measure of the interference capability of the radiation, while the phase governs the positions of the interference fringes' maxima and minima.

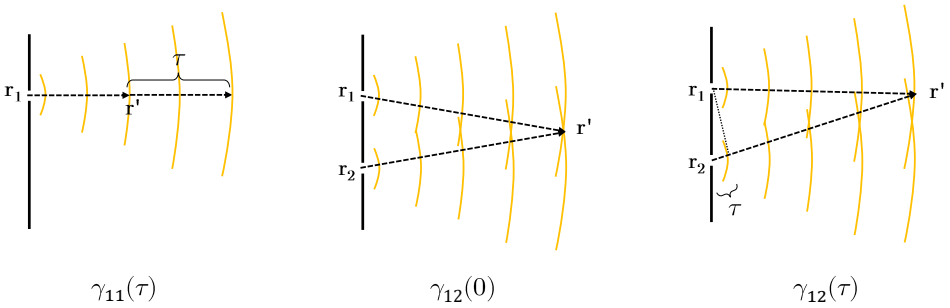

Figure 4.1: Spatial and temporal coherence of a wavefront. On the left, the correlation of a wavefront propagating from a single point is evaluated across a time interval τ to assess its temporal coherence. In the centre, the correlation between two wavelets sampled at different locations is measured with no propagation delay, to assess their spatial coherence. On the right, the same measurement is repeated by introducing a time delay between the two fields, thus also introducing a temporal component in the coherence measurement.

The complex degree of coherence can be decomposed into temporal and spatial components. The temporal correlation of a field can be quantified by fixing the sampling point and scanning the time delay, hence $\gamma_{11}(\tau)$ represents the temporal coherence of the field. In a complementary way, spatial coherence can be probed by sampling two distinct points at zero relative time delay $\gamma_{12}(0)$. In practical scenarios, complete isolation of the temporal and spatial components is challenging because spatial coherence measurements are often performed at a point $\mathbf{r'}$ that is not equidistant from both $\mathbf{r_1}$ and $\mathbf{r_2}$. This difference in distance introduces a corresponding time difference, leading to deviations from a $\tau = 0$ condition. In spatial coherence measurements, it is crucial to verify that the optical path differences involved, given by τc, are always shorter than the coherence length of the radiation, assessed as $l_{coh} \approx \lambda^2/\Delta\lambda$. Since l_{coh} is inversely proportional to the spectral bandwidth, temporal coherence effects vanish for quasi-monochromatic fields. This requirement can be fulfilled by working with quasi-monochromatic sources or by

applying narrow filtering to a broadband spectrum to enhance the radiation temporal coherence.

4.1.2 Degree of coherence in space-frequency domain

The concept of optical coherence has been introduced in the space-time domain, where the complex degree of coherence naturally emerges to quantify the space-time correlation of an optical field. Working with analytical models or numerical simulations, it is more convenient to describe the radiation field in the space-frequency domain. In this framework, the radiation is characterized in terms of the Fourier-transformed field $\tilde{E}(\omega, \mathbf{r})$ extensively discussed in Sec. 2.1. Different quantities are defined to study the optical coherence in the space-frequency domain. Although we will eventually show the equivalence, under certain assumptions, between the space-time and space-frequency treatment of the optical coherence, it is worth discussing this subject further as the comparison is not immediately apparent.

The wavefront correlation in space-frequency domain is quantified by its *cross-spectral density function* [47]. The cross-spectral density between two points of a Fourier-transformed field $\tilde{E}(\omega, \mathbf{r})$ is defined[2] as

$$W_{12}(\omega) \triangleq \langle \tilde{E}(\omega, \mathbf{r_1}) \tilde{E}^*(\omega, \mathbf{r_2}) \rangle, \tag{4.8}$$

where $\langle \dots \rangle$ represents the ensemble average of the field and $*$ the complex-conjugate operation. The cross-spectral density is closely related to the mutual coherence function through a Fourier transform operation [45, p.170]

$$W_{12}(\omega) = \int \Gamma_{12}(\tau) e^{-i\omega\tau} \mathrm{d}\tau. \tag{4.9}$$

When the sampling points coincide, i.e. $\mathbf{r_1} = \mathbf{r_2} = \mathbf{r}$, Eq. 4.9 reduces to

$$I(\omega) = \int I(\tau) e^{-i\omega\tau} \mathrm{d}\tau., \tag{4.10}$$

indicating that the *spectral density* $I(\omega)$, i.e. the spectrum of the radiation, corresponds to the Fourier transform of the radiation intensity in the space-time domain. For a pair of distinct points, $W_{12}(\omega)$ describes the correlation of the radiation spectrum across the wavefront and

[2] Following an approach completely symmetric to what presented in space-time domain, we should evaluate the correlation between two different frequencies ω_1 and ω_2. The complete computation [48] leads to a Dirac delta $\delta(\omega_1 - \omega_2)$ factor in the correlation integral, meaning that field components with different frequencies are completely uncorrelated. This explains why the cross-spectral density is defined at a fixed frequency for both points.

complements the information provided by $\Gamma_{12}(\tau)$. Similarly to the definition of $\gamma_{12}(\tau)$, the cross-spectral density can also be normalized to obtain a quantity whose modulus ranges between zero and a unitary value

$$\mu_{12}(\omega) \triangleq \frac{W_{12}(\omega)}{\sqrt{I(\mathbf{r_1},\omega)I(\mathbf{r_2},\omega)}}. \tag{4.11}$$

This quantity is called *spectral degree of coherence* and quantifies the degree of correlation of the spectral components of the radiation. Despite the similar definition, the spectral degree of coherence differs in general from the complex degree of coherence $\gamma_{12}(\tau)$. The exact relationship between the two quantities writes [49]

$$\gamma_{12}(\tau) = \int_0^\infty \sqrt{\bar{I}(\mathbf{r_1},\omega)\bar{I}(\mathbf{r_2},\omega)}\,\mu_{12}(\omega)\,e^{-i\omega\tau}\mathrm{d}\omega, \tag{4.12}$$

being $\bar{I}(\mathbf{r_i},\omega) \triangleq I(\mathbf{r_i},\omega)/\int I(\mathbf{r_i},\omega)\mathrm{d}\omega$ the normalized spectral density at $\mathbf{r_i}$. Let us notice that the normalized spectral density is not affected by a constant scaling of the entire spectrum. If the radiation spectrum $I(\omega)$ has the same distribution in both points, then $\bar{I}(\mathbf{r_1},\omega) = \bar{I}(\mathbf{r_2},\omega)$, irrespective of the absolute intensity of the radiation at the two locations. An optical field satisfying this condition is defined as *cross-spectrally pure* [48]. Typically, synchrotron radiation wavefronts are not cross-spectrally pure because they feature different spectral distributions as a function of the sampling point. The cases presented in Chapter 3 provide clear examples of this property as the undulator spectrum is highly dependent on the observation angle, and the dipole radiation spectrum displays distinct distributions for edge and core contributions. Since Eq. 4.12 is not an identity, $\mu_{12}(\omega)$ and $\gamma_{12}(\tau)$ are in general not immediately comparable. However, it is intuitive to expect that the space-time and the space-frequency approaches yield the same result when the radiation is quasi-monochromatic. To conclude the comparison between space-time and space-frequency domain, let us consider the quasi-monochromatic scenario.

If the radiation is quasi-monochromatic, one can assume a constant spectral degree of coherence $\mu_{12}(\omega) \approx \mu_{12}(\omega_0)$ over the narrow bandwidth $\Delta\omega$, being ω_0 the average frequency within the range. In space-time domain, the narrow bandwidth implies a long coherence time $\tau_{coh} \approx 1/\Delta\omega$. This corresponds to a scenario where temporal coherence is high enough to not affect the complex degree of coherence, so we can neglect the propagation delay and assume $\tau = 0$. Moreover, if the radiation spectrum can be approximated as uniform over the considered bandwidth, the filtered spectrum is essentially dominated by the narrowband selection and the radiation becomes cross-spectrally pure, yielding $\int \sqrt{\bar{I}(\mathbf{r_1},\omega)\bar{I}(\mathbf{r_2},\omega)}\mathrm{d}\omega = 1$. In quasi-monochromatic conditions,

Eq. 4.12 reduces to

$$\gamma_{12}(0) \approx \mu_{12}(\omega_0), \tag{4.13}$$

thus confirming the equivalence between the two definitions of degrees of coherence. This result allows the direct comparison between the (spatial) degree of coherence $\gamma_{12}(0)$, estimated from experiments, and the spectral degree of coherence $\mu_{12}(\omega_0)$, obtained from theoretical models or numerical simulation of the Fourier-transformed fields. Since in the following we will consistently assume quasi-monochromatic conditions to suppress temporal coherence effects, the distinction between $\gamma_{12}(0)$ and $\mu_{12}(\omega_0)$ becomes irrelevant. For this reason, we will informally refer to the combined quantity as the "degree of coherence", understanding that $\gamma_{12}(0)$ represents the measurable field coherence while $\mu_{12}(\omega_0)$ is the quantity assessed in simulations.

4.1.3 Van Cittert and Zernike theorem

An optical field radiated by a source necessarily carries some information about the source properties. Part of such information is encoded in the correlation properties of the radiation across the emitted wavefront, hence the spatial degree of coherence. This section presents a fundamental result of classical optics, the Van Cittert and Zernike theorem [50, 51], which relates the degree of coherence of the wavefront to the transverse distribution of the source.

Let us assume a fully incoherent planar source Σ, characterized by a transverse two-dimensional distribution $f(\xi, \eta)$, normalized such that $\int_\Sigma f(\xi, \eta)\, \mathrm{d}\xi \mathrm{d}\eta = 1$. The prototypical example of a fully incoherent source is a thermal source, where the radiation originates from numerous point-like elemental emitters, such as excited atoms, whose decay processes occur independently and lack correlation. The intensity radiated by the infinitesimal source element $\mathrm{d}\xi \mathrm{d}\eta$ to the point $\mathbf{r_i}$ writes $\chi_i I_\Sigma f(\xi, \eta) \mathrm{d}\xi \mathrm{d}\eta$, being I_Σ the total source intensity and χ_i an illumination factor, quantifying the fraction of light delivered to $\mathbf{r_i}$. In general, $\chi_i = \chi_i(\xi, \eta)$ as different emitters may differently illuminate the considered points. For isotropic emission, χ_i reduces to the geometric attenuation $1/s_i^2$. Finally, let us assume that the radiation is observed in a narrow spectral band, centred at $\omega = ck = c2\pi/\lambda$, and that the phase of the elemental emitter wavefront can be described by a spherical wave.

Since the source is fully incoherent, the mutual intensity function can be computed as the sum of contributions across the source extension, each radiating a spherical wavefront according

to the Huygens-Fresnel principle

$$\Gamma_{12} = \int_{\Sigma} E(\mathbf{r_1})E^*(\mathbf{r_2}) = I_{\Sigma} \int_{\Sigma} \sqrt{\chi_1\chi_2} f(\xi,\eta) e^{ik(s_1-s_2)} \mathrm{d}\xi\mathrm{d}\eta. \tag{4.14}$$

The quasi-monochromatic assumption allows neglecting any temporal coherence effects. The resulting Γ_{12} represents only the spatial component of the mutual intensity function. The complex degree of coherence is derived upon normalization by the intensity at the two points

$$\gamma_{12} = \frac{\int_{\Sigma} \sqrt{\chi_1\chi_2} f(\xi,\eta) e^{ik(s_1-s_2)} \mathrm{d}\xi\mathrm{d}\eta}{\sqrt{\int_{\Sigma} \chi_1 f(\xi,\eta)\mathrm{d}\xi\mathrm{d}\eta \cdot \int_{\Sigma} \chi_2 f(\xi,\eta)\mathrm{d}\xi\mathrm{d}\eta}}. \tag{4.15}$$

To simplify the expression, let us assume that χ_i is constant over the source. A constant illumination factor does not necessarily mean that the source globally delivers the same absolute intensity to $\mathbf{r_1}$ and $\mathbf{r_2}$. It implies instead that the fractions of light delivered to the two points are the same for each emitter, even though the total intensity arriving at the two points may differ. We refer to this condition as *even illumination* of the two points. To provide a practical example, let us consider a thermal source consisting of independent elemental emitters that radiate an isotropic wavefront. The intensity delivered at two points $\mathbf{r_1}$ and $\mathbf{r_2}$, sufficiently far from the source, is in general different unless they are at the same distance from the source. Nevertheless, the condition of even illumination is satisfied as the fractions of intensity arriving at $\mathbf{r_1}$ and $\mathbf{r_2}$ are the same for all emitters.

Under the assumption of even illumination, the complex degree of coherence reduces to

$$\gamma_{12} = \frac{\int_{\Sigma} f(\xi,\eta) e^{ik(s_1-s_2)}\, \mathrm{d}\xi\mathrm{d}\eta}{\int_{\Sigma} f(\xi,\eta)\, \mathrm{d}\xi\mathrm{d}\eta}. \tag{4.16}$$

This equation already embodies the essence of the Van Cittert and Zernike theorem. It shows that the complex degree of coherence of the source can be decomposed into a sum of pure phase terms, weighted according to the source distribution, which depend only on the path difference between the infinitesimal component of the source and the two sampled points. Under small angle approximation, this path difference can be made explicit [42, p. 574]

$$s_1 - s_2 \approx \frac{(x_1^2 + y_1^2) - (x_2^2 + y_2^2)}{2r_p} - \frac{(\Delta x\xi - \Delta y\eta)}{r_p}, \tag{4.17}$$

where x_i and y_i are the transverse components of $\mathbf{r_i}$, $\Delta x = x_1 - x_2$ and $\Delta y = y_1 - y_2$, and

$r_p \approx s_1 \approx s_2$ is the first order approximation of the source distance. The first term represents the phase difference of a spherical wave propagating from the source centre. Since it does not depend on the transverse position of the emitters, it can be taken out of the integral and gives rise to a constant phase offset ψ. The complex degree of coherence finally reads

$$\gamma_{12} = e^{i\psi} \frac{\int_\Sigma f(\xi,\eta) e^{-i2\pi(\nu_x \xi - \nu_y \eta)} \, \mathrm{d}\xi \mathrm{d}\eta}{\int_\Sigma f(\xi,\eta) \, \mathrm{d}\xi \mathrm{d}\eta}. \tag{4.18}$$

where (ν_x, ν_y) are conveniently introduced as *spatial frequencies*, proportional to the transverse distance of the points at the observation plane

$$\begin{cases} \nu_x = \frac{\Delta x}{r_p \lambda}, \\ \nu_y = \frac{\Delta y}{r_p \lambda}. \end{cases} \tag{4.19}$$

The spatial frequencies represent a set of coordinates useful to map the transverse space of the observer. Their utility extends beyond the VCZ theorem as they are in fact a general concept of Fourier optics, often involved in problems concerning the physical optics propagation (POP) of a wavefront [52, Sec. 2.2].

The Van Cittert and Zernike (VCZ) theorem states that the complex degree of coherence is, apart from a non-important phase term, the two-dimensional Fourier transform of the source profile, evaluated at the spatial frequencies defined in Eq. 4.19. The theorem is strictly valid for purely transverse and fully incoherent sources, under quasi-monochromatic conditions and in small-angle approximation.

Let us consider, for future reference, the VCZ prediction for the degree of coherence generated by a Gaussian-distributed source. Writing the normalized two-dimensional source distribution as

$$f(\xi,\eta) = \frac{1}{2\pi\sigma_\xi\sigma_\eta} e^{-\frac{1}{2}\left(\frac{\xi^2}{\sigma_\xi^2} + \frac{\eta^2}{\sigma_\eta^2}\right)}, \tag{4.20}$$

the VCZ expression for the complex degree of coherence yields

$$\gamma_{12}(\Delta x, \Delta y) = e^{-\frac{1}{2}\left[\left(\frac{2\pi\sigma_\xi}{\lambda r_p}\right)^2 \Delta x^2 + \left(\frac{2\pi\sigma_\eta}{\lambda r_p}\right)^2 \Delta y^2\right]}. \tag{4.21}$$

This result is based on the symmetry of the Gaussian distribution under a Fourier transform operation, for which a Gaussian distributed source with standard deviation σ produces a

Gaussian degree of coherence with standard deviation σ_{coh}, the two being related by

$$\sigma_{coh} = \frac{\lambda r_p}{2\pi\sigma}. \tag{4.22}$$

The above equation shows that the coherence area σ_{coh} of a Gaussian source expands linearly as light propagates, is proportional to the radiation wavelength and it is inversely proportional to the transverse size of the source distribution. The first two behaviours are very general and not limited to the Gaussian case as they are a direct consequence of the definition of the spatial frequencies of Eq. 4.19, which are invariant under distance and wavelength scaling. The exact inverse proportionality on the source size, as well as the 2π factor, are instead specific to the Gaussian function. Nevertheless, the reciprocity between the source size and coherence area can be extended, in a qualitative way, to other source distributions. It is a well-known property of the Fourier transform to preserve the product of the characteristic widths of a function and its transform. Once a characteristic width of the coherence area is defined, such as the full width at half maximum (FWHM) of the degree of coherence, it is legitimate to assume that this quantity scales as the inverse of the source size.

4.2 Partially coherent sources

The Van Cittert and Zernike theorem is based on the assumption of a fully incoherent emission from the source. Synchrotron radiation does not typically satisfy this condition as the source is characterized by an intrinsic finite coherence, ultimately related to the narrow emission angle of the elemental emitters, which make it a *partially coherent source*. The partial coherence at the source location has important consequences on the spatial coherence of the propagating field, which may deviate from the VCZ model. The exact characterization of the LHC SR source coherence requires numerical simulations as no analytical models can cope with the complexity of this scenario. The results of numerical simulations are presented in Sec. 4.3. This section aims at providing a physical insight into the subject of partially coherent sources and introduces an analytical model, the quasi-homogeneous source, that confirms the validity of the VCZ prediction of the degree of coherence for a particular class of partially coherent sources.

To address the scenario of SR, the primary assumption of the VCZ theorem that needs to be relaxed is the one of isotropic radiation from the elemental emitter. To take into account the finite opening angle, we consider an elemental emitter featuring a Gaussian angular distribution

of the radiated intensity, with standard deviation σ'_l, as illustrated in Fig. 4.2. This model offers a realistic approximation of the SR emitted by the single particle, without the need to account for the complexity of the actual angular distribution of SR.

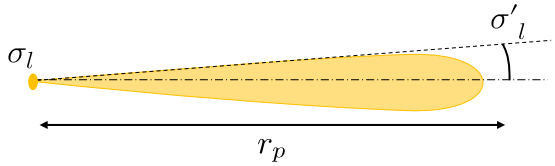

Figure 4.2: Elemental emitter radiating light with an opening angle of σ'_l. The finite emission angle implies a finite extension of the emitter σ_l, the two being constrained by the uncertainty principle $\sigma'_l \cdot \sigma_l \approx \lambda$. The subscript means that these quantities refer to properties of the light and help to distinguish them from the size and divergence of the extended source, σ and σ'.

The finite opening angle σ'_l of the light implies a finite "effective" transverse size σ_l of the elemental emitter, the two being constrained by

$$\sigma_l \approx \frac{1}{4\pi} \frac{\lambda}{\sigma'_l}, \tag{4.23}$$

where λ is the observation wavelength. This relationship arises from the wave nature of light and is a consequence of the position-momentum uncertainty principle applied to the emitted photons. According to the principle, the position and momentum of a particle have uncertainties constrained by $\Delta x \cdot \Delta p_x \approx \hbar/2$, where $\hbar$ is the reduced Planck constant. In the case of photons, the momentum uncertainty is related to the angular spread of the radiation[3], as $\sigma'_l \triangleq \lambda/h\, \Delta p_x$, and the position uncertainty corresponds to the "effective" size of the emitter, as $\sigma_l \triangleq \Delta_x$. The effective size of the elemental emitter is also referred to as *diffraction size* of the radiation [25], because the finite opening angle of the radiation can be described as the diffraction pattern generated by a hypothetical pupil of characteristic width σ_l. Equation 4.23 is a fundamental result of physical optics that has relevant implications on the coherence of the source wavefront. Photons emitted within the diffraction size are indistinguishable, implying that the elemental emitter possesses a finite intrinsic extension. The finite size of the elemental emitter affects the coherence properties of the radiated field as the radiation from the elemental emitter is, by definition, perfectly coherent. The presence of areas of perfect coherence within an extended source undermines one of the fundamental assumptions of the VCZ theorem, which requires complete incoherence across the source plane. The impact of the intrinsic source coherence on

[3]We use the De Broglie relationship for the photon momentum $p = h/\lambda$ and take its projection $p_x \approx p\theta$ to relate the momentum uncertainty with the angular spread

the coherence of the radiated field necessarily needs to be studied. The quasi-homogeneous model was introduced to extend the validity of the VCZ theorem, taking into account a partial degree of coherence at the source plane.

4.2.1 Quasi-homogeneous sources

The coherence properties of a wavefront obey propagation laws similar to the ones that govern the propagation of the field and the radiation intensity. In particular, knowing the cross-spectral density distribution at a given plane $W(\mathbf{r_1}, \mathbf{r_2}, \omega)$, it is possible to propagate the same quantity to downstream planes according to [45, p. 229]

$$W(\mathbf{r_1'}, \mathbf{r_2'}, \omega) = \iint W(\mathbf{r_1}, \mathbf{r_2}, \omega) \frac{e^{ik(s_2 - s_1)}}{s_1 s_2} \mathrm{d}\mathbf{r_1} \mathrm{d}\mathbf{r_2}, \tag{4.24}$$

being $s_i = |\mathbf{r_i'} - \mathbf{r_i}|$ the distance between the considered pair of points and $k = \omega c$ the usual radiation wavevector. The VCZ theorem can be derived as a particular case of this general expression[4], writing the cross-spectral density at the initial plane as $W(\mathbf{r_1}, \mathbf{r_2}, \omega) = I(\mathbf{r_1}, \mathbf{r_2}, \omega)\delta(\mathbf{r_1} - \mathbf{r_2})$, to represent a fully incoherent field at source [45, p. 377].

The assumption of full incoherence can be relaxed by assuming a cross-spectral density of the form

$$W(\mathbf{r_1}, \mathbf{r_2}, \omega) = \sqrt{I(\mathbf{r_1}, \omega)} \sqrt{I(\mathbf{r_2}, \omega)} g(\mathbf{r_2} - \mathbf{r_1}, \omega), \tag{4.25}$$

where $I(\mathbf{r_i}, \omega)$ represents the usual optical intensity at a given point $\mathbf{r_i}$ on the initial plane and g is a generic function of the distance between the pair of points. Let us now assume that both I and g are Gaussian functions, with σ and σ_g as standard deviation respectively and that $\sigma_g \ll \sigma$. Comparing this expression with the definition of Eq. 4.11, this cross-spectral density represents a field with a Gaussian distributed intensity of width σ and characterised by a degree of coherence $\mu_{12}(\omega) = g(\mathbf{r_2} - \mathbf{r_1}, \omega)$ which depends only on the distance between two points. This model is referred to as a *Gaussian Schell quasi-homogeneous* source. In particular, in a Schell source the coherence depends only on the relative distance between two points [53] while the quasi-homogeneous condition requires that the areas of coherence within the source are much smaller than the overall source extension [54], consistently with the assumption $\sigma_g \ll \sigma$. For brevity, we omit the Gaussian Schell attributes and refer to this model as a "quasi-homogeneous" source.

[4] The small-angle approximation of Eq. 4.17 is still needed to obtain a Fourier transform from the resulting integral.

The degree of coherence of the wavefront radiated by a quasi-homogeneous source is still Gaussian and its standard deviation can be analytically computed as

$$\sigma_{coh} = \frac{\lambda r_p}{4\pi\sigma}\sqrt{1+\left(\frac{\sigma_g}{2\sigma}\right)^2}. \tag{4.26}$$

From this result, it is apparent that the quasi-homogeneous model is a generalization of the VCZ theorem as the VCZ expression for the coherence area of Eq. 4.22 is recovered in the limit of fully incoherent source, i.e. for $\sigma_g \to 0$. The important consequence of the quasi-homogeneous model is that, even if the source is characterised by a certain intrinsic coherence, the VCZ result may still apply provided that the source coherence involves areas smaller than the source extension. Under these conditions, the correction factor due to σ_g is negligible. The validity of the quasi-homogeneous model is not guaranteed when the intrinsic degree of coherence σ_g involves areas on the same order of the source transverse size σ. In the case of interest, the intrinsic coherence of the source involves areas on the same order as the diffraction size of the elemental emitters, i.e. $\sigma_g \simeq \sigma_l$. We can therefore conclude that the VCZ theorem is still applicable, through the quasi-homogeneous model, when the source size is much larger than the light diffraction size. However, the situation is not straightforward when the source size approaches the diffraction size. This condition is commonly referred to as the *diffraction limit*, indicating that the properties of light are significantly influenced by the intrinsic diffraction resulting from the finite size of the elemental emitter. Such a scenario can arise in synchrotron radiation sources, where the small opening angle leads to a diffraction size that may be comparable to or smaller than the beam size. In these cases, the assumption of a quasi-homogeneous model may not hold.

4.2.2 Spatial coherence of synchrotron radiation

The quasi-homogeneous model includes a wider class of sources than the simple VCZ. However, it still has some limitations when it comes to synchrotron radiation. The primary limitation of the quasi-homogeneous model is that its validity is not guaranteed when the beam is sufficiently small to approach the diffraction limit. Additionally, describing the SR source only by its transverse spatial distribution is insufficient since the SR elemental emitters are distributed according to the four-dimensional transverse phase space of the beam. Finally, Eq. 4.26 is derived assuming a Gaussian distribution of the intensity radiated by the elemental emitter. However, SR is typically emitted with specific angular distributions, for which a Gaussian model provides only

a qualitative approximation.

More advanced theories have been developed to describe the coherence of SR, based on the complete beam phase-space distributions [55, 56, 57] and at the diffraction limit, taking also into account the effects due to a non-Gaussian shape of the radiated intensity [58]. A detailed discussion of these models is beyond the scopes of this thesis as they mainly focus on the coherence properties of X-ray beams generated by undulators in third-generation light sources. However, some concepts have general validity and can be effectively applied to the case of the LHC SR source.

According to these theories, the validity of the quasi-homogeneous model is always confirmed when the source distribution is much larger than the light diffraction size, irrespective of the particle divergence. The exact angular distribution of the radiation also plays a minor role in these cases. This implies that the analytical expression of the VCZ remains applicable far from the diffraction limit for $\sigma_l \ll \sigma$. This result concerns standard scenarios of light emitted by single devices, such as undulators or dipole magnets. The coherence properties of SR can be influenced by the presence of multiple source devices and their interference. While it is important to include these effects in our study, we will show that, similar to the spatial-spectral distributions, the degree of coherence in the presence of interfering fields still follows the trend predicted by the Van Cittert-Zernike theorem, modulated by the interference effects.

A more complicated scenario occurs when the beam approaches the diffraction limit $\sigma_l \gtrsim \sigma$, even in case of individual devices. The degree of coherence of the radiated field cannot be described by a simple formula and the VCZ does not provide in general an accurate prediction of the coherence area.

The scenarios of quasi-homogeneous and diffraction limit beams are represented in Fig. 4.3.

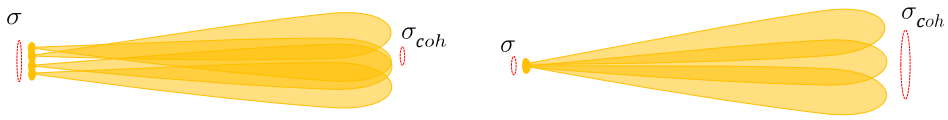

(a) $\sigma'_l \lesssim \sigma'$, $\sigma_l \ll \sigma$ (b) $\sigma'_l \lesssim \sigma'$, $\sigma_l \lesssim \sigma$

Figure 4.3: Sketch to illustrate the coherence properties of quasi-homogeneous SR source (a) and a source close to the diffraction limit (a).

Figure 4.3a illustrates the first scenario where the spatial distribution of the beam is much larger than the width of the single-particle diffraction size. This condition is sufficient to satisfy the quasi-homogeneous model, irrespective of the beam divergence and the exact intensity profile

of the single particle radiation. In fact, recalling the reciprocal relation between source size and coherence area of the emitted field, a large source produces radiation with a narrow coherence area. Although the beam angular distribution may prevent some emitters from illuminating the coherence area, the average effect is that the small coherence area receives light from the entire beam spatial distribution. This scenario is particularly relevant in the field of third-generation light sources, where the coherence properties of synchrotron radiation are primarily studied. It specifically describes the coherence along the horizontal direction, where the beam size exceeds the typical diffraction size. In the context of the LHC SR source, this situation occurs at injection energy, where the beam size is considerably larger than the diffraction size associated with a single emitter.

The opposite case of a source size comparable to the width of the single-particle diffraction size is depicted in Fig. 4.3b. Despite the source being characterized by a high-degree of intrinsic coherence, the coherence area of the radiation is typically narrower than the VCZ prediction [58]. This counter-intuitive result can be qualitatively justified recalling the argument of even illumination, which was introduced in the derivation of the VCZ theorem. The combined effect of a small source size and a narrow opening angle, occurring at the diffraction limit, results in a coherence area larger than the spot of light from the single emitter. Consequently, the emitters do not evenly illuminate the entire coherence area. The uneven illumination leads to an increased value in the denominator of Eq. 4.15, causing the degree of coherence to be smaller than the VCZ prediction. In Section 5.1, we will present an explicit example illustrating this behavior, focusing on the practical case of a Young's interferometer experiment. The phenomenon of coherence loss at the diffraction limit is commonly observed in the vertical direction of third-generation light sources, where the VCZ theorem tends to overestimate the degree of coherence due to this effect. Similarly, this issue may arise in the SR source of the LHC at flat-top energy, where the validity of the quasi-homogeneous model is not guaranteed. In such cases, simulations are necessary to accurately assess the applicability of the VCZ theorem.

4.2.3 Imaging and interferometry resolution at diffraction limit

The finite diffraction size of the elemental emitter is an intrinsic property of the source that inevitably affects the performance of any optical system attempting to resolve the source transverse distribution. This intrinsic diffraction poses a theoretical limit on the resolution of imaging and interferometry techniques.

In imaging systems, the diffraction size sets an intrinsic lower limit for the width of the achievable Point Spread Function (PSF), which represents the system's response to the elemental emitter. The response of the system to the extended source corresponds to a proper convolution between the PSF and the source distribution. However, when the size of the extended source approaches or becomes smaller than the σ_I of the individual emitter, the system sensitivity becomes saturated by the PSF itself, making it challenging to accurately reconstruct the actual distribution of the extended source. Equation 4.23 illustrates that, for a fixed light opening angle, the only way to enhance resolution in the diffraction limit is by reducing the observation wavelength. This explains why the LHC SR telescopes operate in the far-UV range at flat-top energy [13], aiming to increase the resolution margin by minimizing the theoretical width of the PSF.

The diffraction limit also affects the performance of interferometric techniques that rely on the coherence properties of light to reconstruct the transverse profile of the source. Let's first consider the case of a collimated beam with negligible particle divergence, where the radiation divergence is primarily determined by the single-particle opening angle. When approaching the diffraction limit, the large coherence area tends to extend beyond the size of the available light spot. Consequently, the intrinsic coherence of the source saturates the degree of coherence within the limited available light, resulting in a reduced sensitivity to the source's transverse size. To overcome this limitation, it is necessary to decrease the width of the coherence area so that it fits well within the available light spot. In complete analogy with the imaging case, the only effective strategy to achieve this is by reducing the operating wavelength.

In the case of a divergent beam, the manifestation of the diffraction limit is less apparent. If the inverse relationship between the coherence area and the source size held true, a highly divergent beam could potentially fully illuminate an arbitrarily large coherence area without losing its resolution capabilities. However, this apparent violation of the diffraction limit is resolved by the non-validity of the VCZ theorem in this regime. As the source size approaches the diffraction size, the coherence area becomes narrower than the prediction of the VCZ theorem. Increasing the aperture of the available light by increasing the beam divergence would not improve the system's resolution. In essence, the non-validity of the VCZ theorem for small beam sizes directly stems from the fundamental diffraction limit, which cannot be overcome.

4.3 Relevant parameters for the coherence characterization of the LHC synchrotron radiation source

As discussed in the preceding section, the coherence characteristics of a SR wavefront are heavily influenced by the interplay between the parameters of the beam transverse phase space and the properties of the single-particle light. Specifically, the ratio between the beam size and the light diffraction size assumes a crucial role in assessing the validity of the VCZ theorem. This section aims to provide a comprehensive overview of the relevant parameters associated with the elemental emitter light and the extended beam distributions, which are necessary for characterizing the spatial coherence of the LHC SR source. The scenarios of injection and flat-top energy are considered separately, due to differences in beam and light parameters.

4.3.1 Beam and light parameters

The beam parameters relevant to the characterization of the source transverse distributions are summarized in Tab. 4.1. The values reported are representative of nominal conditions for both the beam and the machine, although they may vary in different operational scenarios. In the subsequent discussion, we present some fundamental considerations that are universally applicable to the transverse diagnostics of any LHC beam. The size and divergence of the particle distribution are then compared to the parameters of SR, namely the diffraction size and the opening angle of the light, to provide a preliminary assessment of the spatial coherence properties of the radiated field.

The LHC features rather round beams at the SR source locations, characterized by horizontal and vertical transverse sizes on the same order of magnitude. The symmetry in the beam transverse distribution translates to comparable coherence areas in both directions of the emitted SR. This is a significant difference compared to a typical third-generation light source, where the beams are much larger in the horizontal plane, and transverse diagnostics must cope with a completely asymmetric extent of the SR degree of coherence. The nominal source size at injection is larger than 1 mm in both directions and reduces to values in the order of 300 µm at high energy, as a consequence of the adiabatic damping process described in Sec. 1.2. Assuming that the normalized emittance is preserved during the acceleration process, the beam size at any point of the energy ramp can be assessed from the $\simeq 1/\sqrt{E}$ scaling law. The most relevant parameters in the table are those pertaining to the undulator and the $D3_R$, as they represent the primary

Parameter	$D3_L$	Und	$D3_R$	Unit
Magnetic length L	9.45	0.56	9.45	m
Position s_{centre}	-92.9	0	10.7	m
Horizontal Twiss $(\alpha, \beta)_x$	(0.74, 298)	(0.26, 205)	(0.20, 200)	(rad, m)
Vertical Twiss $(\alpha, \beta)_y$	(-0.15, 218)	(-0.59, 287)	(-0.68, 300)	(rad, m)
Horizontal dispersion D_x	-0.09	-0.10	-0.11	m
Vertical dispersion D_y	-0.07	-0.01	0	m
Emittance ε_n		2.5		µm
Energy spread $\delta E/E$		1.3×10^{-4}		-
		Injection (450 GeV)		
Beam size σ_x	1.25	**1.03**	1.02	mm
Beam divergence $\sigma_{x'}$	5.21	5.21	5.21	µrad
Covariance $\sigma_{xx'}$	-3.86	-1.34	-1.05	mm µrad
Beam size σ_y	1.07	**1.22**	1.25	mm
Beam divergence $\sigma_{y'}$	4.95	4.95	4.95	µrad
Covariance $\sigma_{yy'}$	0.79	3.07	3.33	mm µrad
		Flat-top (6800 GeV)		
Beam size σ_x	328	272	**269**	µm
Beam divergence $\sigma_{x'}$	1.37	1.37	1.37	µrad
Covariance $\sigma_{xx'}$	-268	-92.9	-72.9	µm µrad
Beam size σ_y	281	322	**329**	µm
Beam divergence $\sigma_{y'}$	1.30	1.30	1.30	µrad
Covariance $\sigma_{yy'}$	54.8	212	230	µm µrad

Table 4.1: Nominal parameters of the LHC beam at the locations of the SR source devices. Values are reported for Beam 1 as the interferometer test setup is currently installed on this beam. In bold font, the values of the source size that define the typical operating conditions at injection and flat-top regimes.

sources of SR for Beam 1 diagnostics at the injection and flat-top energy, respectively. Since no quadrupoles are present in the region of the LHC SR source, the beam divergence is conserved, and the transverse size is transported through the source devices using the relationships for free propagation. The absence of quadrupoles in the straight section also justifies the rather smooth betatron function β and the corresponding small value of the divergence of the beams at all source devices. Finally, given the small values of $D_{x,y}$ and momentum spread, another legitimate approximation concerns the impact of dispersion. The correction to the transverse size due to dispersion effects, represented by the second term of Eq. 1.15, yields values much smaller than 1% in all cases. These corrections are beyond the resolution capability of the LHC transverse diagnostics and are therefore neglected in the following discussion.

The beam parameters can be compared with the characteristics of the emitted light to assess the expected spatial coherence properties in different scenarios. Table 4.2 provides a summary of the light parameters. The calculations are performed at two standard wavelengths, 560 nm and 400 nm, which are commonly used in the LHC SR monitors and currently exploited by the

experimental setup of the SR interferometer. At the injection stage, only values for 560 nm are reported, as 400 nm falls outside the main lobe of the undulator spectrum. The light opening angle σ'_l is estimated using Eq.2.17 for undulator radiation and the low-frequency limit of Eq.2.23 for dipole radiation. The diffraction size is determined by the uncertainty principle $\sigma_l \cdot \sigma'_l \approx \lambda/4\pi$, as presented in Eq. 4.23. While these values provide rough estimations, they are in agreement with the more accurate quantities obtained by fitting the spatial distribution of the simulated light spot.

Parameter	Injection - 560 nm	Flat-top - 560 nm	Flat-top - 400 nm	Unit
Light divergence σ'_l	740	280	250	µrad
Diffraction size σ_l	60	160	127	µm
Light width at slits $\sigma'_l \cdot r_p$	22	7.0	6.3	mm
VCZ σ_{coh} at slits	2.5	7.4	5.3	mm

Table 4.2: Typical parameters of the SR available for diagnostics at injection and flat-top energies, evaluated at two wavelengths of interest for interferometric measurements. The source distance r_p is fixed to 30 m for the undulator and 25 m for the dipole. The coherence area is estimated for typical beam sizes of 1 mm at injection energy and 300 µm at flat-top energy.

At injection energy, the characterization of the spatial coherence properties is quite straightforward. The light spot created by the undulator is much broader than the estimated coherence area. The VCZ theorem is expected to apply strictly because, within the scale of the coherence area, the emission is essentially isotropic. The same conclusion is reached by comparing the source size and the single-emitter diffraction size, as the typical transverse beam size σ is more than an order of magnitude larger than σ_l. The quasi-homogeneous model applies to this case and the VCZ theorem is expected to provide an accurate estimation of the degree of coherence. It is worth noting that the emission angle of undulator radiation is actually broader than the acceptance of the extraction mirror. This has relevant consequences for imaging applications as the Point Spread Function at the diffraction limit is affected by the diffraction from the rectangular aperture of the mirror. The diffraction due to the mirror leads to a theoretical PSF in the order of 120 µm, thus twice as large as the intrinsic light diffraction size.

The assessment of the spatial coherence behavior becomes more complicated at high beam energy, as we observe that the expected coherence area is on the same order of magnitude as the size of the available light spot. Similarly, when comparing the beam transverse size and the diffraction size, we find that $\sigma/\sigma_l \approx 2$. This indicates that the intrinsic coherence of the source cannot be ignored, and the application of the VCZ theorem is not guaranteed. The collimated beam is a valid approximation at flat-top energy because the light divergence is two orders of

magnitude larger than the beam divergence. This indicates that the extent of the available light is primarily determined by the opening angle of the single emitter radiation. Even if the VCZ theorem is confirmed, the resolution is limited by the inability to observe the complete decay of the degree of coherence for small beam sizes within the extent of the available light. In addition to the problem of the source intrinsic coherence, the assessment of the coherence properties of the SR at flat-top is also hindered by the specific features of the dipole light, namely the peculiar angular distribution and the interference effects between the two dipoles. No theoretical model exists to deal with such a complicated scenario. Numerical simulations are therefore required to accurately study the transverse coherence properties of the radiation at high energy. Section 4.4 presents the results of the complete numerical characterization.

Double-Gaussian beam distributions

The beam parameters discussed in the previous paragraph are based on the assumption that the beam transverse distribution can be described by a two-dimensional Gaussian function with (σ_x, σ_y) as standard deviations and neglecting the covariance term σ_{xy} due to coupling between the transverse planes. This assumption is valid to describe LHC beams in nominal conditions but there are some specific cases where it was observed[5] that the beam transverse profile features a higher population in the tails that significantly differ from the Gaussian distribution. For such cases, the profile along one of the two transverse directions is better rendered by a linear combination of two Gaussian functions [59]

$$f(\xi) = c\,\frac{1}{\sqrt{2\pi}\sigma_1} e^{-\frac{1}{2}\frac{\xi^2}{\sigma_1^2}} + (1-c)\,\frac{1}{\sqrt{2\pi}\sigma_2} e^{-\frac{1}{2}\frac{\xi^2}{\sigma_2^2}}. \tag{4.27}$$

In this scenario, a fraction c of the particle population is included in a "core" distribution characterised by a standard deviation σ_1 and the remaining $1-c$ fraction of particles belongs to the beam "tails" (or "halo") with a standard deviation σ_2. We fix the convention that $\sigma_1 \geq \sigma_2$ to preserve consistency with the definition of core and tails.

The beam profile described by Eq. 4.27 is a convenient choice as it includes the non-Gaussian characteristics of the actual particle distribution while preserving the simplicity of Gaussian functions in beam propagation and evaluation of the degree of coherence. Exploiting the linearity of the Fourier transform, the degree of coherence predicted by the VCZ theorem can be

[5] Examples are shown in the chapter summarising the beam size measurement performed during the LHC emittance calibration fill.

immediately written as

$$\gamma_{12}(\Delta x) = c\, e^{-\frac{1}{2}\frac{\Delta x^2}{\sigma^2_{coh,1}}} + (1-c)\, e^{-\frac{1}{2}\frac{\Delta x^2}{\sigma^2_{coh,2}}}, \tag{4.28}$$

being $\sigma_{coh,i} = \lambda r_p/(2\pi\sigma_i)$ the coherence area associated to each component of the double-Gaussian profile. The narrower core distribution predominantly influences the high-separation limit of the coherence curve, while the beam tails primarily affect the coherence decay at short separations. As the profile distribution in Eq. 4.23 is normalized, the condition of unitary self-coherence, $\gamma_{12}(0) = 1$, is fulfilled regardless of the core fraction c value.

A relevant aspect of non-Gaussian beam distributions is their propagation along the machine lattice. This is particularly important for cross-comparison between different diagnostic instruments which are normally placed at different locations in the machine. Neglecting all intra-bunch interactions, we can assume that the two distributions propagate as independent Gaussian beams. This assumption is valid for short time intervals (a few minutes) as we will show that, in the long term, core and tails populations evolve in different manners. The emittance of core and halo populations is individually preserved and, applying the definition of Eq. 1.11, the overall beam emittance reads

$$\varepsilon_{dg} = c\,\varepsilon_1 + (1-c)\,\varepsilon_2 = c\,\frac{\sigma_1^2}{\beta}\gamma_{rel} + (1-c)\,\frac{\sigma_2^2}{\beta}\gamma_{rel}, \tag{4.29}$$

where ε_{dg} represents the normalized emittance of the beam, β is the Twiss betatron function at the location where the σ_i are evaluated, and γ_{rel} the relativistic factor. The emittance definition is highly sensitive to the presence of particles at large betatron amplitudes, whereas the performance of the machine is primarily influenced by the population in the core region. This is because particles in the tail region have minimal impact on the luminosity [60]. To provide a more practical definition of the emittance when significant tail contributions are present in the beam distribution, the emittance for a double-Gaussian profile can be evaluated based on the emittance of its simple-Gaussian fit. The beam size resulting from the simple-Gaussian fit is well approximated[6] by the weighted average of the two double Gaussian standard deviations

$$\sigma \approx c\,\sigma_1 + (1-c)\,\sigma_2, \tag{4.30}$$

[6]The approximation is obtained by requiring that the single Gaussian and the double Gaussian profiles have the same area.

to which corresponds the normalized emittance $\varepsilon = \gamma_{rel}\sigma^2/\beta$. It is important to note that this definition is merely practical and does not correspond to any physical quantification of the beam emittance. While the actual emittance in presence of double-Gaussian beam profile is represented by ε_{dg}, the emittance retrieved from the single-Gaussian fit is normally considered in most practical scenarios. Therefore, unless otherwise stated, the term "emittance" in the following will always refer to the (normalized) emittance derived from a simplified Gaussian approximation of the beam profile. Figure 4.4 shows a simulation of a double-Gaussian beam distribution and presents numerical examples of the emittance calculated using different methods.

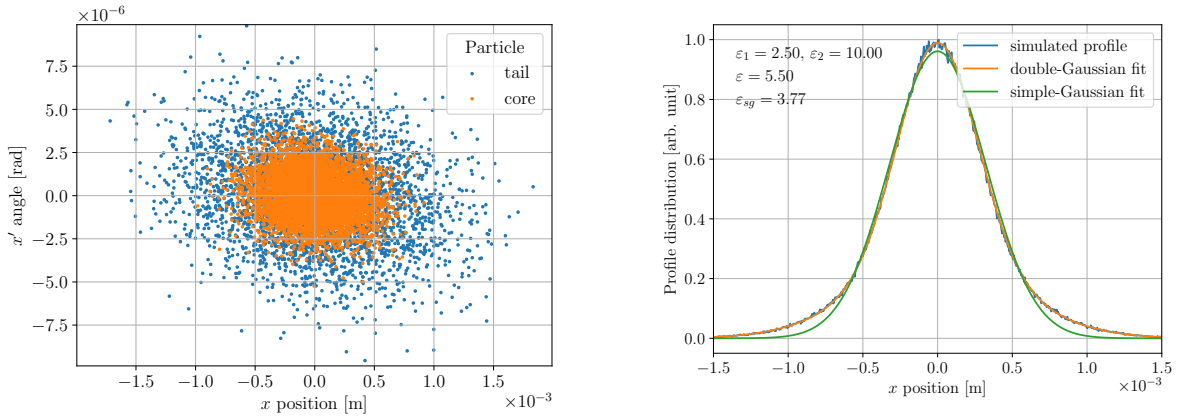

(a) (b)

Figure 4.4: Simulation of a double-Gaussian beam with $\sigma_1 = 200\,\mu\text{m}$, $c = 0.6$ and $\sigma_2/\sigma_1 = 2$. In (a), the simulated phase space and in (b) the spatial profile extracted from the distribution. The simulated profile is fitted with the complete double-Gaussian function of Eq. 4.29 and with an approximated simple Gaussian distribution. The emittance values of the core (ε_1) and tail (ε_2) contributions are annotated on the plot, along with the emittance (ε) calculated from the complete distribution and the effective emittance (ε_{sg}) assessed from the simple Gaussian fit of the profile. All values refer to the normalized emittance and expressed in units of µm. In particular, it is worth noting that σ_{sg} is smaller than σ, reflecting the underestimation of the tail contribution when the simple-Gaussian fit is adopted.

4.4 Simulations of LHC SR source degree of coherence

The spatial coherence properties of the LHC synchrotron radiation source are extensively investigated using numerical simulations performed with SRW. The characterization at injection energy is relatively straightforward due to the highly uniform coherence properties of undulator radiation. However, at flat-top energy, the situation becomes more complex as the coherence properties may deviate from the quasi-homogeneous model. Moreover, the degree of coherence is influenced by interference effects arising from the interaction between the two D3 dipoles.

The primary objective of this section is to develop a practical algorithm for extracting the transverse beam profile from the degree of coherence. The algorithm should be implementable in operational scenarios, enabling real-time transverse diagnostics while minimizing the need for extensive data processing. The VCZ theorem presents an ideal approach as it provides a direct formula for retrieving the source size from the coherence area of the radiation. Even in cases where the theorem is not globally applicable to the entire wavefront due to the specific characteristics of the radiation, our aim is to preserve the analytical formula of Eq. 4.22 by properly redefining source distance parameters to ensure an accurate reconstruction of the beam profile.

4.4.1 Simulation approach and coherence maps

The output of an SRW simulation of the radiation emitted by a single particle is a set of four matrices, which map the real and imaginary parts of each polarization component of the radiated field. In the following, we only consider the horizontal polarization as it is the more intense and thus the more suitable for measurements. Given the Fourier-transformed field $\tilde{E}_m(x, y, \omega)$ of the m-particle, the spectral degree of coherence of the finite beam reads

$$\mu(x_1, x_2, y_1, y_2, \omega) = \frac{\langle \tilde{E}_m(x_1, y_1) \tilde{E}_m^*(x_2, y_2) \rangle}{\langle \tilde{I}_m(x_1, y_1) \rangle \langle \tilde{I}_m(x_2, y_2) \rangle}, \tag{4.31}$$

where $\langle \dots \rangle$ represents the average over the simulated particles and $\tilde{I}_m(x_i, y_i) = \tilde{E}_m(x_i, y_i) \tilde{E}_m^*(x_i, y_i)$ the intensity of the single particle radiation at (x_i, y_i). The expression for the spectral degree of coherence stems directly from the definition of Eq. 4.11, under the assumption that fields from different particles are uncorrelated.

In order to implement a pure Monte Carlo approach, one would sample the four-dimensional transverse phase space of the beam at a given source location and simulate numerous single-particle trajectories. This method requires the simulation of hundreds of thousands of particles, making it a computationally heavy approach. However, since the computation of the SR field is a deterministic process, random sampling of the space phase is superfluous. An alternative and more efficient strategy is the "macroparticle" simulation. This approach involves sampling the transverse phase space with a uniform mesh and assigning a weight to each particle's contribution based on the beam's transverse distribution at the sampled location. This approach eliminates the need for simulating hundreds of thousands of particles, as only a few hundred

macroparticles are required to accurately replicate the complete beam distribution. In the case of the LHC source, the simulation effort can be further optimized by exploiting the negligible divergence of the beam. This allows the approximation of a perfectly collimated beam, which requires extracting macroparticle samples from the sole two-dimensional spatial distribution. The simulations presented in this study follow the macroparticle simulation approach, as it does not rely on any restrictive assumptions. It is worth noting that in lightweight simulations, where the precise phase space distribution is not a critical factor, the approximation of a perfectly collimated beam remains a practical and useful approach.

To fully characterize the radiation degree of coherence, one would need to evaluate the spectral degree of coherence between all possible pairs of points across the wavefront. This approach is impractical and highly redundant as it does not take advantage of any symmetry in the radiation. A more convenient solution is to define a reference axis and compute the degree of coherence between all points that are symmetric with respect to that axis. For instance, in the horizontal case, one can compute $\mu(x_0 - \Delta x, x_0 + \Delta x, y, \omega)$, where x_0 represents the coordinate of the folding axis. The resulting coherence values can be visualized as a *coherence map*, which illustrates how the degree of coherence decays as a function of the distance from the reference axis. Similarly, the vertical direction can be examined by folding the wavefront around a horizontal reference axis and computing $\mu(x, y_0 - \Delta y, y_0 + \Delta y, \omega)$. Although the position of the reference axis can be arbitrarily chosen, a convenient approach is to align it with the symmetry axes of the radiation spatial distribution.

4.4.2 Undulator radiation at injection energy

Undulator radiation exhibits symmetry in the vertical and horizontal directions with respect to a reference axis that passes through the undulator axis. The most natural approach to characterize the radiation coherence is to compute the degree of coherence between pairs of points symmetric with respect to these reference axes. The resulting coherence maps are reported in Fig. 4.5 and Fig. 4.6, for the vertical and horizontal cases respectively. The simulations are performed at the operating wavelength of 560 nm. This corresponds to the operating wavelength of the interferometer at injection and is close to the undulator proper wavelength of 610 nm.

Both coherence maps show a smooth decay as the distance from the folding axis increases. The width of the degree of coherence is uniform along the axis[7], confirming the homogeneity of

[7] One may notice a slight deviation at the positions ±38 mm along the folding axis, in both maps. This anomaly

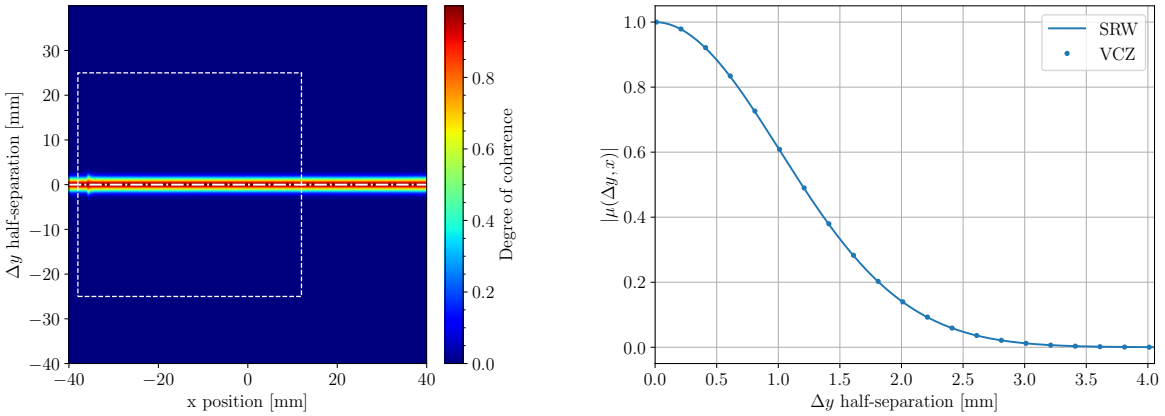

(a) (b)

Figure 4.5: Degree of coherence along the vertical direction of undulator radiation at 450 GeV and 560 nm, simulated for a nominal beam of 2.5 µm normalized emittance and evaluated at the extraction mirror plane ($z = 29.27$ m). In (a), the two-dimensional coherence map is computed with respect to a horizontal folding axis at $y_0 = 0$. The white dashed perimeter encloses the region of points allowed by the extraction mirror aperture. In (b), a profile of the degree of coherence is extracted from the coherence map at $x_0 = 0$ and compared with the VCZ prediction.

undulator radiation coherence. The agreement of the simulation result with the VCZ prediction is apparent from the plot of the coherence map cross-cut, where the simulated curve perfectly overlaps with the Gaussian decay obtained as the Fourier transform of the source profile, characterized by the coherence area of Eq. 4.22. The same result is obtained by computing the coherence map with respect to folding axes placed at different positions, for both transverse directions.

At injection energy, simulations validate the VCZ expression for the spatial degree of coherence across the entire undulator wavefront. This finding is consistent with the prediction of the quasi-homogeneous model, as the source size significantly exceeds the light diffraction size.

4.4.3 Dipole radiation at flat-top energy

As previously observed for the spatial distribution, we expect that also the coherence properties of synchrotron radiation at high beam energy are influenced by the more complicated structure of the radiated field. The degree of coherence does not exhibit the same uniformity as in the case of undulator radiation, and the appearance of the coherence maps varies significantly based on the selection of the reference axis. It is not expected that the VCZ theorem applies in its canonical form. To investigate the coherence properties of synchrotron radiation in the high

coincides with the first zero of the undulator intensity distribution, produced by a π value in the sinc function argument of Eq. 2.14. The normalization of the cross-spectral density leads to a division by zero, which in turn results in a degree of coherence that is highly susceptible to numerical errors.

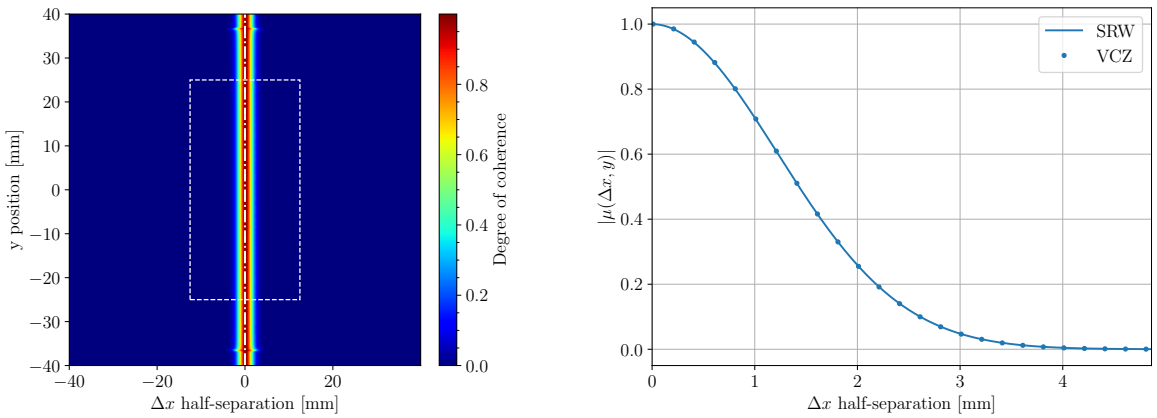

(a) (b)

Figure 4.6: Degree of coherence along the horizontal direction of undulator radiation at 450 GeV and 560 nm, simulated for a nominal beam of 2.5 µm normalised emittance and evaluated at the extraction mirror plane ($z = 29.27$ m). In (a), the two-dimensional coherence map is displayed with respect to a vertical folding axis at $x_0 = 0$. The white dashed perimeter encloses the region of points allowed by the extraction mirror aperture. In (b), a profile of the degree of coherence is extracted from the coherence map at $y_0 = 0$ and compared with the VCZ prediction.

energy regime, it is convenient to examine the horizontal and vertical directions separately, starting with the simpler vertical case.

Vertical direction

Along the vertical direction, it is possible to exploit the SR symmetry with respect to the orbit plane by placing the reference axis at $y_0 = 0$, i.e. the same as the one considered for undulator radiation. The resulting coherence map is reported in Fig. 4.7.

The aspect of the coherence map is tightly related to the spatial distribution of the two D3 at high energy, which was illustrated in the bottom plot of Fig. 3.9. The same regions identified when discussing the spatial distribution are observed in the coherence map, dominated by the $D3_L$, the $D3_R$ and their interference. In the same way as the intensity background is dominated by an almost uniform light from the upstream $D3_L$, the peripheral region of the coherence map is characterised by an almost Gaussian uniform coherence profile. In the region corresponding to the core radiation from the $D3_R$, the degree of coherence still shows a rather smooth decay characterised by a narrower width. The region around the straight section axis is marked by the usual concentric rings of dipole interference. Before quantitatively examining the width of the coherence area in different regions of the wavefront, it is worth noting that the light emitted by the far $D3_L$ dipole exhibits a significantly larger coherence area compared to the

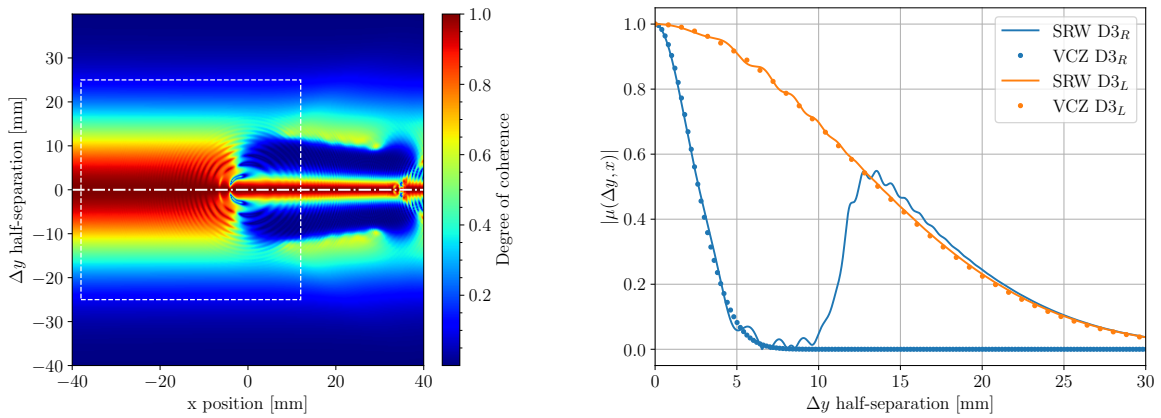

(a) (b)

Figure 4.7: Degree of coherence along the vertical direction of the LHC SR source at 6800 GeV and 400 nm, simulated for a nominal beam of 2.5 µm normalised emittance and evaluated at the extraction mirror plane ($z = 29.27$ m). In (a), the coherence map is computed with respect to the folding axis lying on the orbit plane at $y_0 = 0$. The white dashed square defines the region of points allowed by the extraction mirror aperture. In (b), a quantitative comparison of the degree of coherence decay and VCZ prediction extracting vertical cross-cuts of the coherence map at $x = 6$ mm ($D3_R$) and $x = -20$ mm ($D3_L$). A detailed description of the curves is reported in the text.

region dominated by the $D3_R$. This qualitative observation confirms the expected increase in coherence area with respect to the source distance.

A quantitative comparison of the two dipole contributions is presented in Fig. 4.7, where cross-cuts are extracted from the coherence map in the region entirely governed by the $D3_L$ light (orange solid curve) and the one dominated by radiation from the $D3_R$ (blue solid curve). The curve for the $D3_L$ well agrees with the coherence decay predicted by the VCZ theorem (orange dots) when the source position is located at the centre of the $D3_L$. This suggests that the $D3_L$ is sufficiently far from the observer to neglect the longitudinal extension of the dipole and use the average distance as r_p parameter to evaluate the σ_{coh} in the VCZ formula. It is important to notice that the conformity with the VCZ prediction is not limited only to the Gaussian shape, but the theorem precisely reproduces the width of the coherence decay. This quantitative agreement provides initial evidence to support the applicability of the VCZ theorem to the flat-top case, despite the uncertainty arising from the comparison between the source size and light diffraction size. The coherence cross-cut extracted at $x = 6$ mm exhibits two distinct behaviours. For half-separations up to 5 mm the degree of coherence is monotonically decreasing following a Gaussian trend. This part of the curve represents the coherence of the core radiation from the $D3_R$, prevailing at small latitude angles. Seeking an analytical formula to describe the

coherence decay in this region, the VCZ theorem is not immediately applicable as the source distance r_p is considerably affected by the $D3_R$ longitudinal extension. The fact that the source distance changes along the dipole is visible in the coherence map. The width of the coherence area decreases moving from $x = 0$, corresponding to the radiation emitted by the initial part of the dipole, to $x = 34\,\text{mm}$, where the incoming radiation is predominantly emitted in the last segment of the dipole close to the exit edge. To reproduce the degree of coherence decay along the dipole, let us assume that the source distance r_p is measured along the direction tangent to the beam trajectory passing through the observer position. This definition of r_p is illustrated in Fig. 4.8 and quantifies the concept of "sweeping searchlight" already discussed for dipole radiation in Sec. 3.4. With the usual small angle approximations, the source distance can be written as

$$r_p \approx (z - z_{in})\sqrt{1 - \frac{2\rho x}{(z - z_{in})^2}}, \tag{4.32}$$

being $z - z_{in}$ the distance between the observer and the dipole entrance edge, x the observer's transverse position and ρ the dipole bending radius. One can verify that r_p ranges from the entrance edge distance $z - z_{in}$, for $x = 0$, to the exit edge distance $z - z_{in} - l_{core}$, for $x = z l_{core}/\rho - l_{core}^2/(2\rho)$, being l_{core} the magnetic length of the dipole. With this definition of source distance, the simulated decay of the $D3_R$ degree of coherence perfectly overlaps with a Gaussian with σ_{coh} given by Eq. 4.22 (blue dots). The VCZ result is still applicable, provided the source distance parameter is adjusted taking into account the position where the degree of coherence is evaluated. For half-separations larger than 10 mm, core radiation from the $D3_R$ is negligible and, eventually, the $D3_L$ becomes again the prevailing contribution.

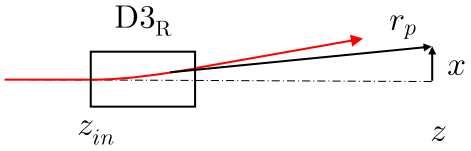

Figure 4.8: Definition of source distance r_p for SR emitted by the $D3_R$ dipole.

Although SR from the $D3_L$ exhibits a more regular coherence profile, it is not suitable for beam diagnostics because of the lower available intensity. Additionally, since this light is generated much upstream of the extraction mirror, it is more affected by spurious reflections in the vacuum chamber during propagation. It is therefore crucial to confirm that the beam size information can be reliably retrieved from the coherence properties of the experimentally available $D3_R$ light. For this purpose, the simulated degree of coherence of the $D3_R$ is fitted

with a Gaussian function to obtain the σ_{coh} as a function of the horizontal position of the coherence cross-cut. Equation 4.22 is then used to obtain the VCZ source size and the associated emittance is finally compared to the input value. The procedure is repeated to cover the full range of normalised emittance values relevant to LHC beams. The results of these simulations are summarised in Fig. 4.9.

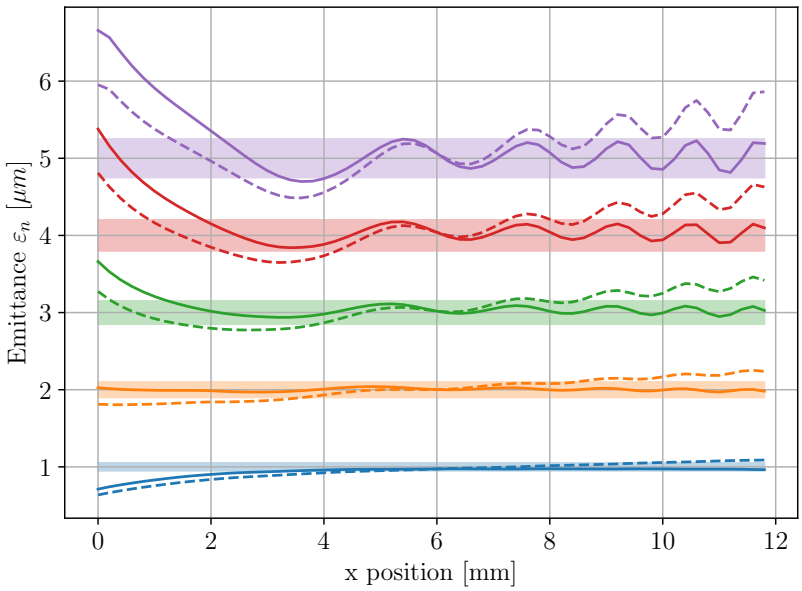

Figure 4.9: Reconstruction of the beam emittance from the simulated degree of coherence of the $D3_R$ radiation, using the VCZ theorem. The simulation is performed for various values of normalized emittance ranging from 1 to 5 µm. Colour bands represent a tolerance of ±5 % around the input value. The solid curves are obtained using the source distance defined in Eq 4.27, while an average value of r_p is fixed for the dashed curves.

The emittance reconstruction fails at horizontal positions close to the magnet edge where the interference between the two dipoles distorts the coherence decay. However, values consistent within the desired ±5 % accuracy are obtained elsewhere, regardless of the input emittance. This finding has two significant implications. Firstly, it provides a straightforward algorithm for evaluating the beam emittance from radiation coherence, using the analytical expression of the VCZ theorem with the corrected source distance. Secondly, it confirms the consistency of this correction for all emittance values, demonstrating the validity of the VCZ at high energies also for the smallest beams of interest for the LHC transverse diagnostics.

In summary, despite being more challenging than at injection, the vertical direction at flat-top energy provides a fully consistent and practical approach to retrieve the beam emittance from the degree of coherence of the sole $D3_R$ radiation. The presented algorithm relies on the analytical result of the VCZ theorem, which has been demonstrated to be applicable upon

correction for the longitudinal extension of the dipole source.

Horizontal direction

The asymmetry of the dipole synchrotron radiation significantly affects the coherence properties along the horizontal direction. Finding a suitable reference axis for computing the degree of coherence in the horizontal direction is not straightforward due to this lack of symmetry. Therefore, we opt for a folding axis that is convenient in practice. As explained in the previous paragraph, the synchrotron radiation from the $D3_R$ is the one ultimately exploitable in measurements. Referring to the high-energy SR distribution of Fig. 3.9, the core radiation from the $D3_R$ dipole is essentially confined between its entrance and exit edge directions, located at $x = 0$ and $x = 34\,\text{mm}$ respectively at the observation plane. Evaluating the degree of coherence between points symmetric to the centre of the dipole radiation would have no practical utility as none of these pairs is eventually allowed by the horizontal aperture of the extraction mirror. A more convenient position for the reference axis is at the centre of the extracted portion of the $D3_R$ radiation, i.e. for $x_0 = x_{mirror}/2 \approx 6\,\text{mm}$. This choice limits the study to the coherence properties of the sole light accessible for beam diagnostics. The resulting degree of coherence is reported in Fig. 4.10.

Similarly to the case of the vertical direction, it is possible to identify two distinct behaviours. Within the region $-10\,\text{mm} < y < 10\,\text{mm}$, where the prevailing source is indeed the $D3_R$, the degree of coherence exhibits a considerably narrower width than the background radiation, which is dominated by the more distant $D3_L$. The validity of this interpretation is supported by a quantitative analysis of the simulated degree of coherence compared to the VCZ prediction. The cross-cut of the simulated degree of coherence in the background region (orange line) is in good agreement with the VCZ Gaussian decay (orange dots) that originates from a source at the centre of the $D3_L$. On the other hand, the degree of coherence pertaining to the small-angle radiation (blue curve) is consistent with the VCZ prediction for a source situated within the $D3_R$ (blue dots). As for the vertical case, fluctuations in the coherence profiles appear as a consequence of the interference between the dipoles. The $D3_R$ coherence profile of Fig. 4.10b suggests that the VCZ theorem provides an accurate expression to predict the average trend of the coherence decay.

For a more detailed investigation of the VCZ applicability to the horizontal direction, let us assess the accuracy of the emittance reconstruction from the fit of the degree of coherence.

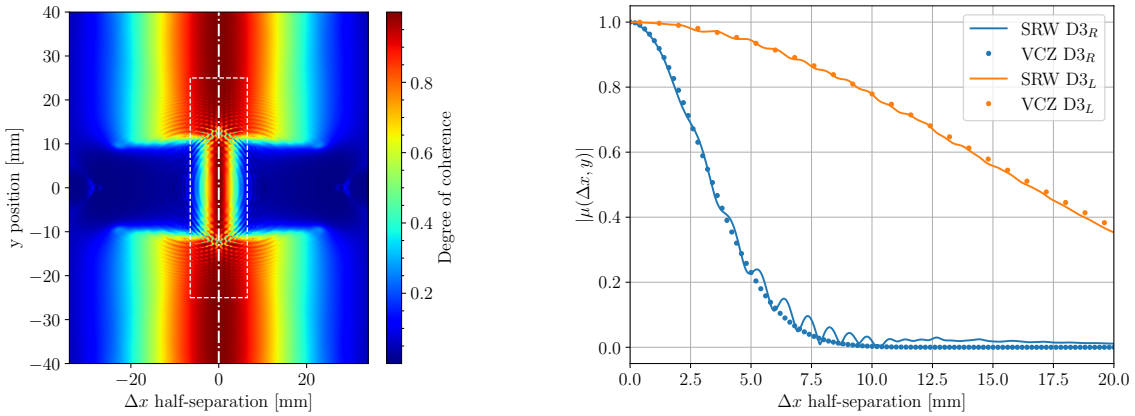

(a) (b)

Figure 4.10: Degree of coherence along the horizontal direction of the LHC SR source at 6800 GeV and 400 nm, simulated for a nominal beam of 2.5 µm normalised emittance and evaluated at the extraction mirror plane ($z = 29.27$ m). In (a), the coherence map computed with respect to a vertical folding axis at the centre of the $D3_R$ light available for extraction, i.e. at $x_0 = 6$ mm. The white dashed square defines the region of points the extraction mirror aperture allows. Note that the horizontal range of the available half-separations is limited to approximately 6 mm, the distance between the reference axis and the extraction mirror edge. In (b), a quantitative comparison of the degree of coherence decay and VCZ prediction extracting horizontal cross-cuts of the coherence map at $y = 0$ ($D3_R$) and $y = 20$ mm ($D3_L$). A detailed description of the curves is reported in the text.

The procedure is similar to the one presented for the simulation of Fig. 4.9. The result of this analysis for the horizontal direction is illustrated in Fig. 4.11. One of the main objectives of this simulation is to investigate how the reconstructed emittance varies with the horizontal position of the sampled points, which is in turn related to the longitudinal position inside the dipole where the radiation is emitted. For this purpose, the curves are computed by moving the position of the reference axis x_0 and extracting the coherence cross-cut to fit at $y = 0$. The source distance parameter required by the VCZ formula is again obtained from Eq. 4.27, where the position of the folding axis x_0 is used as the value for the x coordinate. This approach yields an average value for the parameter r_p, a trade-off between the distances associated with the two points $x_0 \pm \Delta x$. The emittance assessed using an average distance, fixed for all folding axis positions, is plotted for reference (dashed lines).

The retrieval of the input emittance is successful within the required tolerance when the folding axis position x_0 is greater than 6 mm. This is not unexpected since the coherence properties of the radiation are relatively uniform in this region, as all points are sampled from the $D3_R$ core radiation. The simulation also demonstrates that correcting for the source distance results in a more accurate emittance estimation than the value obtained using a fixed average

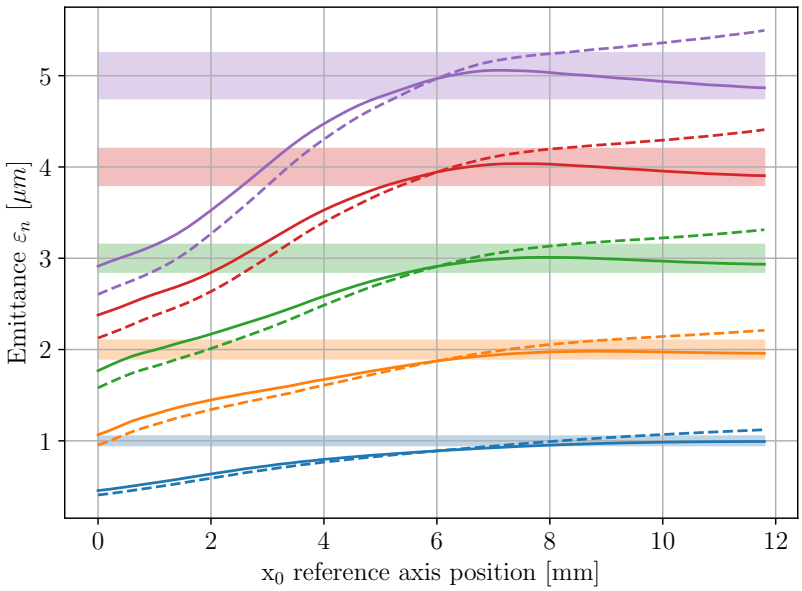

Figure 4.11: Reconstruction of the beam emittance from the simulated degree of coherence of the $D3_R$ radiation, using the VCZ theorem. The simulation is performed for various values of normalised emittance ranging from 1 to 5 µm. Colour bands represent a tolerance of ±5 % around the input value. The solid curves are obtained using the source distance defined in Eq 4.27, where the x corresponds to the position of the reference axis. An average value of r_p is fixed for the dashed curves.

distance.

A relevant issue affecting the horizontal degree of coherence is that the available range of separations approaches zero as the folding axis position approaches the mirror edge. It is therefore important to note that although the simulated curves are relatively flat for $x_0 \gtrsim 6\,\text{mm}$, it is convenient to limit the working region to $6\,\text{mm} \lesssim x_0 \lesssim 8\,\text{mm}$. This ensures that a wider range of point separations is available to resolve a sufficient coherence decay.

The retrieved emittance clearly deviates from the input value when the folding axis is placed in the edge region of the $D3_R$, i.e. for $x_0 \lesssim 6\,\text{mm}$. This discrepancy occurs because, while the points sampled at $x_0 + \Delta x$ are mostly illuminated by the $D3_R$ core radiation, the opposite points at $x_0 - \Delta x$ carry a relevant contribution from $D3_L$. The resulting coherence is affected by this heterogeneity and the method proposed for the emittance reconstruction, based on the VCZ applied to the sole $D3_R$, fails to deal with the spurious $D3_L$ contribution.

In conclusion, the assessment of the beam emittance at high beam energy is confirmed also along the horizontal direction, for all values of the LHC transverse emittance. Like the vertical case, the VCZ theorem is not exact as the SR wavefront emitted by the LHC source at flat-top does not feature a uniform degree of coherence. However, the VCZ analytical expression is

applicable, in an approximate way, for a quantitative reconstruction of the beam emittance. It is important to notice that the difficulties encountered arise essentially from the complicated structure of the LHC source at high energy. Simulations do not provide evidence of a deviation from the VCZ theorem due to the intrinsic coherence of the source, even for the smallest beams of interest. We can therefore conclude that the quasi-homogeneous model is suitable to describe the coherence properties also along the horizontal direction at high beam energy.

Chapter 5

Synchrotron radiation interferometry at the LHC

In the previous chapter, it was demonstrated that the analysis of the spatial coherence of the synchrotron radiation emitted by the LHC source allows reconstructing the transverse distribution of the particle beams. Under certain conditions, the application of the Van Cittert and Zernike theorem provides a straightforward approach to infer the source transverse profile from the degree of coherence of the emitted light. This result is very general and not limited to the specific technique used to measure the radiation coherence.

This chapter focuses on the implementation of synchrotron radiation interferometry (BSRI) at the LHC. The fundamental working principle of the Young's double slit interferometer is presented as the basis for the design of the LHC interferometer. The experimental setup currently installed at the LHC is described, along with a discussion of the simulations performed to characterize its performance. The last section showcases a collection of experimental observations which serves as a qualitative validation of the system response and provides the necessary context for discussing the performance of the BSRI as an instrument for accurate beam size measurement, which will be the central subject of the subsequent chapter.

5.1 Young's double slit interferometer

Interferometry is the branch of optics related to the measurement of the complex degree of coherence between different points of a wavefront. The general interference law of Eq. 4.6

$$I(\mathbf{r}') = I_1(\mathbf{r}') + I_2(\mathbf{r}') + 2\sqrt{I_1(\mathbf{r}')I_2(\mathbf{r}')}\,\mathrm{Re}\{\gamma_{12}(\tau)\} \tag{5.1}$$

states that the intensity $I(\mathbf{r}')$ resulting from the superposition of two points of the wavefront carries information about the coherence $\gamma_{12}(\tau)$. If the superposition occurs without introducing a time delay between the interfering points, the complex degree of coherence $\gamma_{12}(\tau)$ reduces to the spatial degree of coherence $\gamma_{12}(0)$ or, equivalently, the cross-spectral density $\mu_{12}(\omega)$. As extensively discussed in Sec. 4.1, the equivalence is guaranteed for quasi-monochromatic fields, provided that the optical path delays are always shorter than the coherence length of the radiation. A *spatial interferometer* is any optical apparatus that exploits this effect to measure the (spatial) degree of coherence of a wavefront.

Due to the virtually infinite number of configurations that can produce an overlap between two points of a wavefront, a multitude of spatial interferometer designs have been proposed [61, 62, 63, 64]. The Young's double-slit apparatus was the first proposed and conceptually the simplest [42, p.290]. The working principle of this interferometer is illustrated in Fig. 5.1.

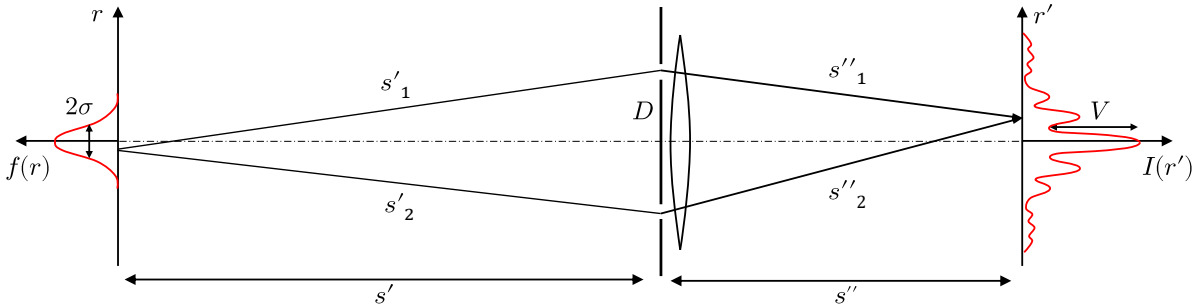

Figure 5.1: The Young's double-slit interferometer.

The light emitted by a source is sampled by two apertures, or slits, separated by a distance D. The wavelets emerging from the two slits propagate to a downstream plane where the intensity resulting from their overlap is recorded by a detector. If the detector is placed sufficiently far from the slit plane, the intensity patterns from each slit become so wide that distance between the centres, due to the slit separation, becomes negligible. Under these conditions, the intensity distributions produced by the two apertures perfectly overlap, resulting in the formation of

interference fringes. In free propagation, the superposition of the two fields requires a significant distance downstream of the slit plane. A solution to make the system more compact is to place a lens just after the slit plane, so that the single-aperture patterns overlap at the image plane, as illustrated in the figure above. Given the distance s' between the source and the slits, the distance between the slit plane and the detector s'' is determined by the thin lens equation $s'' = fs'/(s' - f)$, and can be adjusted by a proper choice of the lens focal length f.

In order to find an explicit expression for Eq. 5.1, the intensity distribution of a single-slit $I_1(\mathbf{r}')$ can be written as the diffraction function of the aperture [42, p. 425]. Under monochromatic conditions and in the far field, the intensity pattern created by an aperture follows the Fraunhofer diffraction law, which involves the Fourier transform of the aperture shape. In the case of rectangular apertures, the Fourier transform results in the product of squared sinc functions along each direction

$$I_i(\mathbf{r}') = I_i(x, y) = I_{i,0}\,\mathrm{sinc}^2\left(\frac{\pi w}{\lambda s''}x\right)\mathrm{sinc}^2\left(\frac{\pi h}{\lambda s''}y\right) \tag{5.2}$$

where $I_{i,0}$ represents the optical intensity transmitted by each aperture, (w, h) are the aperture dimensions, λ the operating wavelength and s'' the average distance between the slit and the detector planes. The Fraunhofer diffraction condition, $s'' \gg w^2/\lambda$, typically requires rather large observation distances. If a lens is added to the setup, the parameter s'' appearing in the single-aperture diffraction pattern coincides with the distance between the lens and its image plane.

When both apertures are considered, the general law of interference yields the intensity distribution

$$I(\mathbf{r}') = (I_{1,0} + I_{2,0})\,\mathrm{sinc}^2\left(\frac{\pi w}{\lambda s''}x\right)\mathrm{sinc}^2\left(\frac{\pi h}{\lambda s''}y\right)\left[1 + \frac{2\sqrt{I_{1,0}I_{2,0}}}{I_{1,0} + I_{2,0}}\,\mathrm{Re}\{\gamma_{12}(\tau)\}\right], \tag{5.3}$$

where $\gamma_{12}(0)$ is the degree of coherence of the wavefront points sampled by the two apertures. Since the degree of coherence is a complex quantity, it can be conveniently expanded as

$$\gamma_{12}(\tau) = |\gamma_{12}(0)|e^{i\frac{2\pi}{\lambda}(s_2'' - s_1'') + \phi_{12,0}}, \tag{5.4}$$

being $|\gamma_{12}(0)|$ the modulus of the degree of (spatial) coherence at the slits and $\phi_{12,0}$ a constant phase difference between the fields sampled by the two slits. Equation 5.4 is based on the

assumption of negligible temporal coherence effects. The modulus of the degree of coherence is evaluated at zero delay, $|\gamma_{12}(\tau)| \approx |\gamma_{12}(0)|$, and the path difference $s_2'' - s_1''$ implies only a phase contribution that appears as a modulation of the intensity pattern. In order to obtain an explicit expression for the intensity distribution, let us assume that the two apertures are aligned along the horizontal direction, meaning that the slit separation D is parallel to the x coordinate of the detector plane. Under the usual small angle approximation, the path difference can be expanded as $s_2'' - s_1'' \approx xD/s''$ [42, p. 291]. In case of vertical slit configuration, i.e. D parallel to the y coordinate, the same approximation holds true with $x \leftrightarrow y$.

Expanding the degree of coherence and using the small angle approximation for the path difference, Eq 5.3 can be finally written as

$$I(\mathbf{r}') = (I_{1,0} + I_{2,0}) \operatorname{sinc}^2\left(\frac{\pi w}{\lambda s''}x\right)\operatorname{sinc}^2\left(\frac{\pi h}{\lambda s''}y\right)\left[1 + \frac{2\sqrt{I_{1,0}I_{2,0}}}{I_{1,0} + I_{2,0}}|\gamma_{12}(0)|\cos\left(\frac{2\pi D}{\lambda s''}x + \phi_{12,0}\right)\right]. \tag{5.5}$$

This equation describes the intensity distribution produced by any Young's interferometer with rectangular apertures. In the following, it is referred to as the *interferogram* of the radiation. Similar to any interference pattern, it can be interpreted as the incoherent sum of the two intensity contributions $I_i(\mathbf{r}')$, modulated by an oscillating function that depends on the degree of coherence. The intensity oscillations, or *interference fringes*, are confined within the envelopes

$$I^{\pm}(\mathbf{r}') = (I_{1,0} + I_{2,0}) \operatorname{sinc}^2\left(\frac{\pi w}{\lambda s''}x\right)\operatorname{sinc}^2\left(\frac{\pi h}{\lambda s''}y\right)\left(1 \pm \frac{2\sqrt{I_{1,0}I_{2,0}}}{I_{1,0} + I_{2,0}}|\gamma_{12}(0)|\right). \tag{5.6}$$

The contrast of the interference fringes is called *visibility* and it is defined as difference between the upper and lower intensity envelopes, normalized by their sum

$$V \triangleq \frac{I^+ - I^-}{I^+ + I^-}. \tag{5.7}$$

A unitary visibility indicates that fringes exhibit maximum contrast, meaning that the waves propagating from the two apertures can interfere in a fully constructive or destructive way. Conversely, in the case of null visibility, no interference fringes appear as the interferogram represents the incoherent sum of the two intensity distributions. From the expression of the intensity envelopes, the relationship between the visibility and the degree of coherence can be made explicit as

$$V = \frac{2\sqrt{I_{1,0}I_{2,0}}}{I_{1,0} + I_{2,0}}|\gamma_{12}(0)|. \tag{5.8}$$

The fringe visibility serves as the experimental observable associated with the modulus of the degree of coherence. The proportionality factor in the last equation accounts for the intensity difference between the radiation transmitted through the two apertures. When the transmitted intensities $I_{i,0}$ are equal, the wavelets from both apertures interfere with equal strength at the detector, and the fringe contrast is solely determined by the coherence of the fields. However, if there is an imbalance in intensities, interference occurs between waves of different strengths, resulting in a fringe contrast that is always less than the modulus of the degree of coherence. Consequently, perfect coherence does not lead to complete destructive or constructive interference unless the intensities of the interfering fields are identical. While the interferogram visibility does not precisely correspond to the modulus of the degree of coherence, one should note that the correction for intensity imbalance is often negligible in most practical situations. Even in an extreme case where $I_{1,0} = 2I_{2,0}$, the fringe visibility is only reduced by a factor of approximately 6 % compared to $|\gamma_{12}(0)|$. This correction is typically insignificant for quasi-uniform wavefronts. It becomes relevant in specific scenarios, which will be discussed in the following paragraphs.

The experimental setup of a Young's double-slit interferometer closely resembles the system illustrated in Fig.5.1. One of the key advantages of the Young's apparatus is its simplicity, as it only requires the ability to block the wavefront and allow the propagation of only the two desired points to the detector. In the visible spectrum, implementing a Young's interferometer is straightforward using an opaque mask with two apertures. Due to the few optical components required, the setup is very robust and minimally affected by misalignment errors. The design of the double-slit interferometer can be adapted to measure the degree of coherence for various wavefronts, and it has found applications across a wide range of the electromagnetic spectrum. It has been employed to measure micro-metric electron beams using X-ray synchrotron radiation [65] and to determine the size of astronomical targets in the radio-wave domain [66]. The most relevant limitation of the double-slit interferometer, compared to most sophisticated spatial interferometer designs, is that it can only measure the degree of coherence for two points at a time. Mapping the degree of coherence across the entire wavefront may require lengthy measurements and necessitates a flexible setup capable of providing a large array of slit configurations.

The measurement procedure is straightforward. For a specific configuration of the slits, the interferogram captured by the detector is fitted using the expression provided in Eq. 5.5 to determine the fringe visibility. Most of the parameters in the fringe pattern equation are known

by design of the setup. The interference phase $\phi_{12,0}$ and the total amplitude $I_{1,0} + I_{2,0}$ are left as fitting parameters, along with the visibility itself. In cases where the correction for the imbalance factor is significant, two additional measurements are required. These involve separately measuring the amplitudes of the diffraction patterns produced by each aperture separately, to assess the single-slit intensities $I_{1,0}$ and $I_{2,0}$. Typically, the measurement is repeated to explore different configurations of the setup, such as varying the slit separation, adjusting the absolute position of the slits across the wavefront, or changing the operating wavelength.

If the source satisfies the Van Cittert and Zernike theorem, the degree of coherence is solely dependent on the distance between the sampled points[1]. This condition provides a simplified approach to fully characterize the coherence of the wavefront by measuring the decay of visibility as a function of slit separation, irrespective of the absolute position of the two apertures. Assuming a Gaussian-distributed source and neglecting intensity imbalance, the visibility can be directly related to the source size σ using Eq. 4.22 to obtain

$$V = e^{-\frac{2\pi^2 D^2}{\lambda^2 s'^2}\sigma^2}. \tag{5.9}$$

This equation indicates that, in theory, the visibility V measured at a single slit separation D is sufficient to determine the source size σ of a Gaussian beam. However, in practice, it is more reliable to measure the visibility at multiple slit separations to enhance measurement statistics and improve accuracy. The resulting visibility as a function of the slit separation $V(D)$ is then fitted using Eq. 5.9 to obtain the source size as a fit parameters. In the following, we will refer to this type of measurement as "slit separation scan". The slit separation scan is also the standard method to obtain more information about the actual source profile, as the decay of the degree of coherence corresponds to the Fourier transform of the source transverse distribution. In the case of non-Gaussian beams, a complete slit separation scan is necessary to reconstruct the actual beam profile and accurately assess the transverse size.

The fit of the interferogram provides additional information about the phase of the wavefront, encoded in the fringe phase $\phi_{12,0}$. The phase information becomes crucial when the complex degree of coherence is actually a complex function, as the knowledge of the modulus of $\gamma_{12}(0)$ is not sufficient for accurately reconstructing the source profile. This limitation does not affect the case of interest. In the context of transverse distributions of particles in an accelerator beam,

[1] This applies in general to any Schell-model source

we can safely assume that the source transverse profiles are always symmetric[2]. The symmetry of the transverse profile implies that the degree of coherence is a purely real function of the slit separation, as the Fourier transform of a real and even function remains real and even. While the interferogram phase $\gamma_{12}(0)$ does not provide necessary information for reconstructing the beam profile, it allows investigating some theoretical properties of the wavefront. One such application is the study of the polarization characteristics of the dipole radiation at flat-top energy, which will be discussed in detail in a dedicated paragraph below.

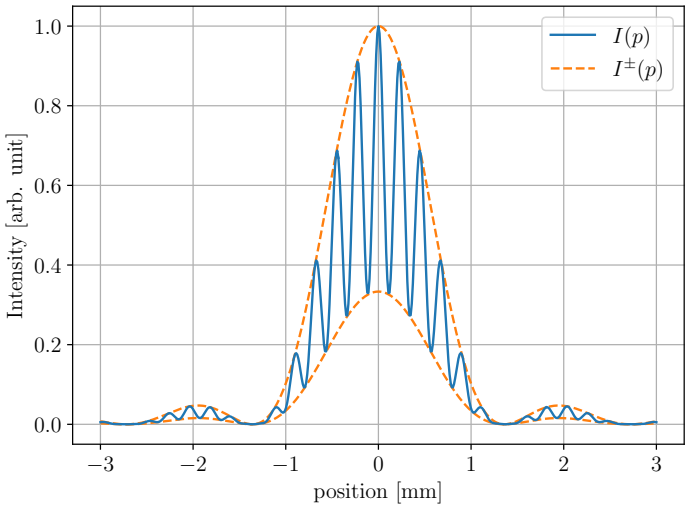

Figure 5.2: Typical interferogram profile. The interference fringes at the detector (blue curve) are described by the integration of Eq. 5.5 along the axis perpendicular to the slit separation. The intensity modulation is bounded by the envelope (orange curve) determined by the spatial degree of coherence of the pair of points sampled by the slits.

5.1.1 Young's experiment: physical understanding

The Young's double-slit interferometer serves not only as a practical experimental setup, but also as a convenient system for gaining a physical understanding of how the source distribution influences the coherence properties of the wavefront. This paragraph aims to provide an insight into the formation of the Young's interference fringes. We start by considering the straightforward case of a classical thermal source, to give a geometric interpretation of the VCZ theorem. We then assume a finite opening angle of the elemental emitters, to approach the diffraction limit and show why the VCZ theorem fails to predict the wavefront coherence in this regime. These scenarios are illustrated in Fig. 5.3. To simplify the analysis, we assume point-like aper-

[2]As described in Chapter 1, particles in the accelerator oscillate around the nominal orbit. Even if the bunch was initially injected with an asymmetric distribution, these oscillations would induce a "filamentation" process in the transverse phase space, that eventually results in a symmetric transverse profile.

tures. The corresponding diffraction pattern is so broad that the single-slit intensity distribution is essentially uniform over the entire detector plane. Furthermore, we assume monochromatic conditions to exclude any temporal coherence effects from our discussion.

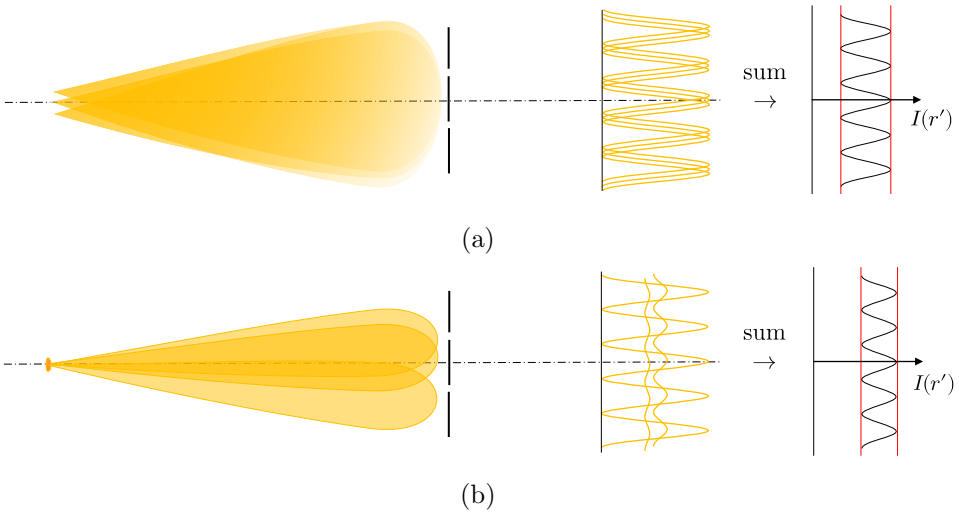

Figure 5.3: Qualitative representation of a Young's experiment with a (a) thermal source and a (b) source at diffraction limit, as presented in Fig. 4.3b.

Thermal source: the Van Cittert and Zernike theorem

A fundamental property of a thermal source is the isotropic emission of each elemental emitter. As discussed in Sec. 4.2, this condition is intimately related with the complete incoherence at the source plane. The interferogram of the extended source can be decomposed into the incoherent sum of the contributions from each individual emitter. The interferogram associated with the elemental emitter exhibits a unitary visibility. This is because the wavefront radiated by each emitter is, by definition, fully coherent, and the isotropic emission ensures that the intensity transmitted through the two slits is perfectly balanced. However, the transverse position of the interference fringes is not the same for all elemental interferograms, as it depends on the transverse position of the emitter. In fact, a change in the emitter position results in a corresponding shift in the location where destructive or constructive interference takes place at the detector. The interferogram of the extended source is the sum of many identical interferograms, with unitary visibility and shifted according to the emitter transverse positions. The interferogram resulting from the incoherent sum has a visibility lower than one, which depends on the transverse distribution of the source. This is the fundamental principle underlying the VCZ theorem, as it explains why the visibility of the extended source interferogram carries information on

the transverse source distribution. This principle is qualitatively illustrated in Fig. 5.3a. Three elemental emitters produce staggered interferograms with unitary visibility. The incoherent sum of these patterns yields the interferogram of the extended source with a non-unitary visibility. The reciprocity relationship between the source size and the coherence area of the wavefront can also be understood by considering that a larger source leads to a lower visibility, due to the widespread distribution of the elemental interferogram positions. Conversely, the elemental interferograms of a small source closely overlap, therefore preserving a higher visibility.

A similar situation occurs when the light radiated by the single emitter is not perfectly isotropic but its aperture significantly exceeds the coherence area of the radiation. In such cases, the intensity of light passing through the two slits is approximately equal for all emitters, leading to the formation of elemental interferograms with the almost unitary visibility. The interferogram of the extended source originates following the same principle described for the thermal source, thus preserving the relationship between the source distribution and the visibility. This type of source corresponds to the quasi-homogeneous model discussed in the previous chapter, where it was demonstrated that the VCZ theorem is applicable, albeit in an approximate manner.

Diffraction limit

Figure 5.3b depicts the case of a source at the diffraction limit, for a beam with a particle divergence comparable with the light opening angle. The diffraction limit implies that the coherence area, thus the required slit separation, is comparable to or larger than the extent of the single-particle light distribution. In this regime, the visibility of the elemental interferogram is not necessarily the same for all emitters. When an emitter uniformly illuminates the two slits, the corresponding interferogram maintains a unitary visibility. However, a tilted particle provides an imbalanced illumination which produces an interferogram with lower visibility. In the extreme case where a particle illuminates only one slit, interference does not occur, and the single particle contribution resembles the flat intensity distribution given by the diffraction from the single aperture. The visibility resulting from the sum of the elemental interferograms is lower than the value predicted by the VCZ theorem. The reason for this is that the fringe contrast is dictated not only by the transverse distribution of the beam, which is the fundamental principle of the VCZ theorem, but also by the imbalance of the illumination across the elemental emitters. This effect is the visual representation of the concept of uneven illumination discussed

in Section 4.1, in the specific case of a Young's interferometer. The resolution performance of the system is limited because only particles that evenly illuminate both apertures effectively convey information about the source distribution. Other particles contribute to a constant intensity background that degrades the interferogram contrast without adding information about the source profile.

Finally, let us examine the diffraction limit for a collimated beam. In this particular scenario, the beam divergence is negligible, ensuring an even illumination of the two apertures. As a result, the individual interferograms generated by each particle exhibit full contrast, with the fringe position determined by the emitter location, similar to what observed for a thermal source. The VCZ theorem accurately estimates the degree of coherence within the confines of the available light. However, it becomes impossible to measure the complete decay of the coherence degree since the coherence area extends beyond the reach of the available light. The limited extent of the available light constrains the resolution of the technique and represents the manifestation of the diffraction limit for a small and collimated beam.

5.2 Implementation at the LHC

Young's interferometry in the visible domain can be implemented using a simple optical setup, making this apparatus a convenient option for a SR interferometer at the LHC. Due to the challenging environmental conditions and limited accessibility to the instrumentation during machine operation, remote control of the setup is necessary, with interventions restricted to a few days per year. To address these requirements, a test setup of a synchrotron radiation interferometer (BSRI) was developed and installed during the LHC run 2 (2015-2018) [13]. Subsequently, the setup underwent upgrades and optimizations during the long shutdown 2 (2018-2022) based on the latest simulations of the LHC SR source, as detailed in this thesis. This section reports the main design parameters and provides an overview of the current implementation of the BSRI setup.

5.2.1 Design parameters: operating wavelength and slit separation

In order to optimize a double-slit interferometer design, the primary objective is to maximize the system's sensitivity to the transverse size of the source. For Gaussian distributed sources, the maximum sensitivity of the visibility to the transverse size is found for a slit separation that

matches the coherence area, i.e. $\sigma_{coh} = D$, which corresponds to a visibility value of $V = 1/\sqrt{e} \approx 0.6$. For a given source size, the interferogram visibility depends on the slit separation, the source distance and the working wavelength, according to Eq. 5.9. In the case of the LHC SR source, the source distance is given by the source layout and corresponds to approximately 26 m. As extensively described in Sec. 4.4, the best estimation of the source distance varies from injection energy to 6800 GeV, following the source evolution as a function of the beam energy. Since the source distance is fixed by the existing hardware, the interferometer optimization concerns the operating wavelength and the slit separation. The wavelength is constrained by the radiation spectrum and the choice of working in the visible domain ($400 \div 800$ nm) whereas the extent of the available SR intensity distribution limits the maximum achievable slit separation. The following considerations ultimately aim to identify a convenient selection of band-pass filters and slit configurations, given the limited options that can be implemented in the experimental setup.

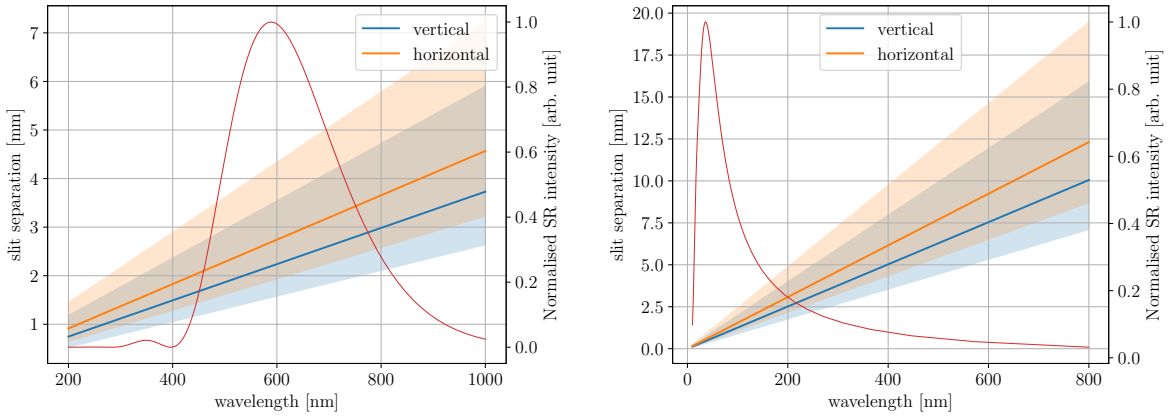

Figure 5.4: Optimization of the BSRI operating wavelength at (a) injection energy and at (b) flat-top energy. The blue and orange curves represent the sets of wavelengths and slit separations that produce the target visibility of $V = 0.6$ at the nominal emittance $\varepsilon_n = 2.5\,\mu$m, for the vertical and horizontal direction respectively. The color band represents the full range of LHC normalized emittance $1 \div 5\,\mu$m. The red curve reports the normalized SR spectrum at the two beam energies.

Figure 5.4 provides an overview of the parameters relevant for the design of the system. At the injection energy, the spatial distribution of the undulator light is significantly larger than the radiation coherence area. This ensures that any desired slit separation can be selected, in the visible domain and across the entire range of beam emittance. However, the operating wavelength is limited by the bandwidth of the on-axis undulator spectrum. To maximize the

photon flux at the slits, the operating wavelength should be chosen in the vicinity of 610 nm, which corresponds to the undulator proper wavelength at the injection energy. At high beam energy, the peak of the SR spectrum emitted by the dipoles lies in the soft X-ray region. The radiation intensity becomes almost flat over the whole visible domain and is much higher than at injection energy, due to the larger relativistic factor of the particles. Consequently, the photon flux is no longer a constraint and, instead, the incoming radiation is usually attenuated to prevent the saturation of the detector. The choice of the wavelength is then determined by the extent of the coherence area, which should not exceed the width of the available SR distribution, around 7 mm from Tab. 4.2. Figure 5.4b shows that the reference visibility for a slit separation of 7 mm is obtained with an operating wavelength between 500 nm and 600 nm. Shorter wavelengths are anyway useful to resolve the full visibility decay within the extent of light spot, especially for beams with a smaller emittance than the reference value of 2.5 µm.

These constraints led to the selection of two band-pass filters with central wavelengths of 560 nm and 400 nm. The 560 nm filter is optimized for injection energy and can still be used with high-energy beams. Furthermore, this wavelength lies at the centre of the visible domain, where standard optical components typically exhibit optimal performance. The 400 nm filter is beyond the undulator range at injection energy but can help reduce the required slit separation at flat-top energy, where the coherence area of the small emittance beams at 560 nm is comparable or larger than the light spot size. Additionally, the 400 nm wavelength is a standard for the other LHC SR monitors, making this band-pass filter useful for comparison purposes in the setup.

The other parameter needed to identify a band-pass filter is the bandwidth of the transmitted light. A spatial interferometer would ideally require an infinitely small bandwidth to satisfy the monochromatic condition and ensure that the degree of coherence is not affected by temporal effects. In practice, a finite bandwidth is required to have a light intensity sufficient for measurements. Therefore, the optimization consists in finding the largest bandwidth that allows an accurate reconstruction of the source size from the interferogram visibility. The result of this procedure is reported in Fig. 5.5.

Since no correlation exists between fields at different wavelength, the interferogram of the finite bandwidth radiation corresponds to the incoherent sum of the individual monochromatic contributions. Figure 5.5a shows some examples of interferogram simulated at different radiation bandwidths. A finite bandwidth leads to a reduction in fringe visibility in the peripheral region of the interferogram. This phenomenon originates from the finite temporal coherence of the non-

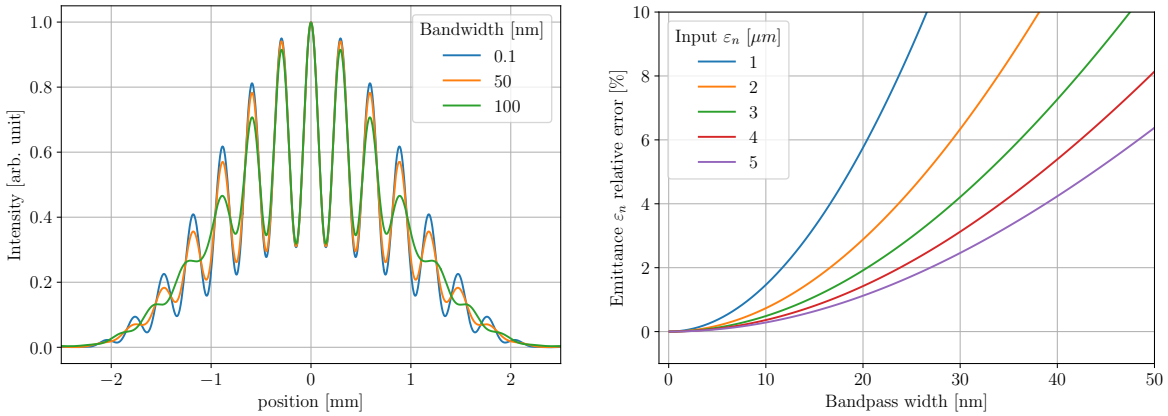

(a) (b)

Figure 5.5: Impact of a finite radiation bandwidth on the source size estimation. In (a), interferograms simulated at different radiation bandwidths, centred at a typical average wavelength of 560 nm. In (b), effect of the finite bandwidth on the beam emittance reconstruction.

monochromatic radiation. The optical path to reach the centre of the interference pattern has the same length for light coming from both slits. The temporal correlation at the interferogram centre is therefore always unitary and the visibility is only reduced by the spatial component of the degree of coherence, irrespective of the radiation bandwidth. However, in the peripheral regions of the interferogram, the optical path difference introduces a loss of correlation that depends on the coherence length of the radiation, thus the spectral bandwidth. This loss of temporal coherence distorts the shape of the interferogram. Using the interferogram function of Eq. 5.5 to fit the intensity profile leads to an underestimation of the visibility because the fringe contrast is not entirely determined by the spatial degree of coherence. The lower visibility eventually results in an overestimation of the beam emittance. An example of the relative errors of the emittance retrieved from the fit of finite bandwidth interferograms is plotted in Fig. 5.5b. The precise values reported in the figure are not universal, as different slit separations and central wavelength may produce slightly different curves. Nevertheless, one may observe that the relative error is always smaller than 1.5 % provided that the bandwidth is narrower than 10 nm, hence a $\Delta\lambda/\lambda < 2\,\%$. This estimation is conservative as it pertains to the smallest achievable emittance and assumes a uniform intensity distribution within the bandwidth. In reality, band-pass filters often exhibit a smoother transmissivity function, where the majority of the light is transmitted at the nominal wavelength and only the tails extend beyond the FWHM. Taking this into account, we can conclude that a band-pass filter with a 10 nm FWHM bandwidth is normally sufficient to ensure the quasi-monochromatic condition.

The values provided in this section serve to define the typical operating conditions and are necessary for determining certain design parameters of the experimental setup. However, it is important to note that the system performance is not heavily dependent on these design values, and reliable measurements can still be obtained under non-optimal conditions. For accurate measurements, it is recommended to work with intermediate values of fringe visibility. The visibility should not be too low, as the fringe contrast would be too sensitive to fluctuations in the light intensity. Conversely, a visibility close to one indicates that the wavefront is essentially fully coherent, and the fringe contrast is marginally influenced by the source size. To optimize the sensitivity to the source transverse size, it is generally desirable to operate within a visibility range of $0.2 \lesssim V \lesssim 0.8$

5.2.2 Experimental setup and control tools

The experimental setup for the BSRI is located at Point 4 of the LHC, installed on the same optical table as the SR telescopes. After being intercepted by the extraction mirror, the radiation is directed towards an optical table located in a light-shielded area beneath the accelerator beam pipe. The incoming light is distributed to all SR monitors using a system of folding mirrors and splitters. At present, the BSRI line receives approximately 35 % of the extracted SR intensity. A diagram of the BSRI setup, depicting the relevant optical components in a schematic view, is shown in Fig. 5.6.

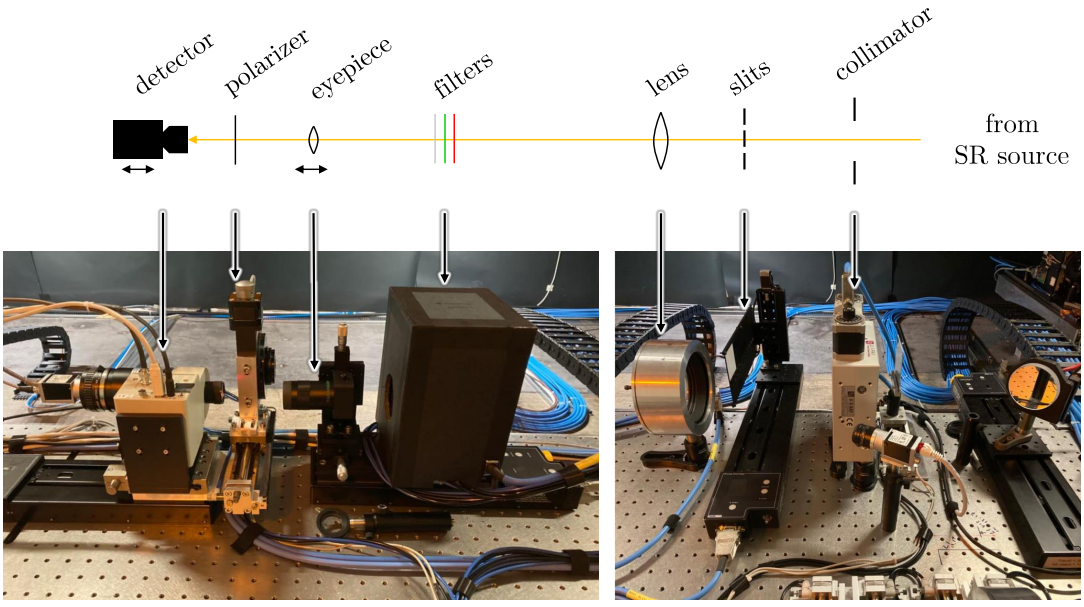

Figure 5.6: The SR interferometer (BSRI) installed at the LHC during run 3.

A motorized mirror at the entrance of the interferometer allows the steering of the optical

line. Downstream of the steering mirror, the light is sampled according to the required double-slit configuration. The light shaping is achieved with a collimator followed by an opaque mask with several laser-cut slit pairs. The collimator ensures that only one slit pair is illuminated at a time, preventing light from passing through the other slits. A slit configuration is defined according to the convention shown in Fig. 5.7. The two rectangular apertures are characterized by a width w, which is evaluated in the direction of the slit separation, and an height h, perpendicular to the former. The transverse position of the slit configuration is defined by the position of its centre (x_c, y_c) relative to the undulator axis, assumed as the reference axis for the SR spatial distribution. In the present BSRI setup, the slit width is determined by the design of the slit opaque mask, which currently includes two sets of slits with 500 µm and 1 mm width. The available slit separations are also chosen by design and range from 3 mm to 12 mm, according to the considerations presented in the previous section. In particular, the smaller slit separation are mainly used to probe the narrow coherence area at injection energy whereas slit separations above 6 mm are normally required at flat-top energy. The slit height has a maximum value of 15 mm and can be finely adjusted by changing the collimator aperture. The entire slit assembly is motorized so that any slit configuration can be transversely shifted across the incoming light. The slit configuration can be positioned anywhere within the 50 mm × 50 mm collimator aperture. This feature is particularly important to study the two-dimensional map of the degree of coherence of the SR at the slit plane.

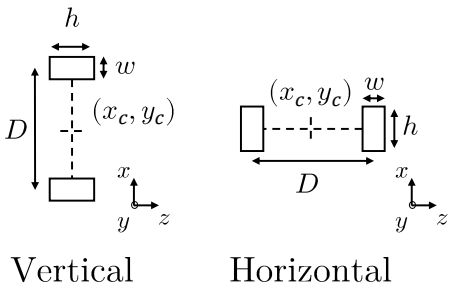

Figure 5.7: Geometry of the BSRI slits. Notice the definition of the width and height dimensions depending on the slit direction.

The quality of the visible SR arriving at the slit plane can be monitored with a camera, which is also used to align the slit assembly with respect to the SR. The light sampled by the slit assembly propagates though the interferometer optical system. Given the large distance from the source, the single lens of the classical Young's apparatus is replaced by a refractive telescope consisting of a main lens and a magnifying secondary lens. The main lens is a super apochromatic

triplet with 816 mm focal length and 102 mm aperture (F/8), taken from a Takahashi TSA-102 refractive telescope. The secondary lens is an eyepiece with 30 mm focal length, from the same company. The primary lens is fixed on the optical table, while the eyepiece is mounted on a translation stage to enable the adjustment of the system focus. In a Young's interferometer, the accurate focus is achieved when the intensity distributions from the individual apertures overlap at the detector plane. A set of neutral density (ND) and bandpass filters is installed in the drift space between the two lenses. All filters are mounted on pneumatic actuators and can be independently inserted in the line. The ND filters are standard absorptive filters from Thorlabs. The available attenuation range is $10 \div 10^5$ (OD1 ÷ OD5). Two hard-coated bandpass filters from Edmund Optics allows the selection of the design 560 nm and 400 nm wavelengths, with an average background attenuation of 10^4 (OD4) and a FWHM bandwidth of 10 nm. A linear polarizer from Newport, featuring an extinction ratio of 700:1, is placed between the eyepiece and the detector. The polarizer is mounted on a rotational stage, enabling the measurement of the interferogram parameters' dependence on the polarization state of the light. The last component of the line is the detector. This device consists of a digital camera (Basler acA1920-25gm) coupled to a fast-gated image intensifier unit (Hamamatsu C9547-01). Due to the LHC bunch spacing of 25 ns, currently available cameras are not sufficiently fast to perform single bunch measurements. An image intensifier is a device based on a microchannel plate (MCP) that can be used as fast light shutter, with an achievable gating time as short as 3 ns. To acquire single bunch data, the intensifier gate is synchronized with the passage of the bunch. Multiple single-turn interferograms are then integrated on the camera to obtain a high-quality signal.

The BSRI uses standard hardware of the LHC SR monitors and it is fully integrated in the CERN control system. The setup is entirely controlled via a Graphical User Interface (GUI) written in Python. The images acquired by the camera are processed by the GUI which provide a real-time monitoring of the interferogram parameters. The BSRI GUI also allows the automated execution of standard parameters scans, such as moving the slits to map the wavefront visibility or performing a scan of the slit separation to measure the coherence decay for different bunches.

5.3 Expected performance of the Synchrotron Radiation interferometer

The potential of reconstructing the beam size based on the coherence properties of the synchrotron radiation wavefront was thoroughly investigated in Chapter 4. In this section, we present the results of simulations that have been carried out to assess the expected performance of the BSRI system. The objective is to confirm the applicability of a Young's interferometer to reconstruct the beam profile and define operational scenarios that effectively address the challenges posed by the complex nature of the LHC SR source.

The complete BSRI optical system is implemented in SRW. The single-particle interferograms are simulated at the detector plane, using the Physical Optics Propagation feature of the code. The interferogram of the extended source is obtained by incoherently summing the single-particle contributions and then fitted to determine the fringe visibility. The visibility is corrected for the intensity imbalance, if necessary, and the resulting degree of coherence is compared to the VCZ prediction. The system response is evaluated by repeating the procedure with different geometries of the slits, to assess the dependence of the visibility on the slit configuration.

The distribution of the SR arriving at the slit plane is shown in Fig. 5.8. The horizontal aperture of the light is limited by the acceptance of the extraction mirror. Since the slits are located approximately 2 m downstream of the extraction plane, the intensity cut is enveloped by the fringes of the Fresnel diffraction from the mirror edge.

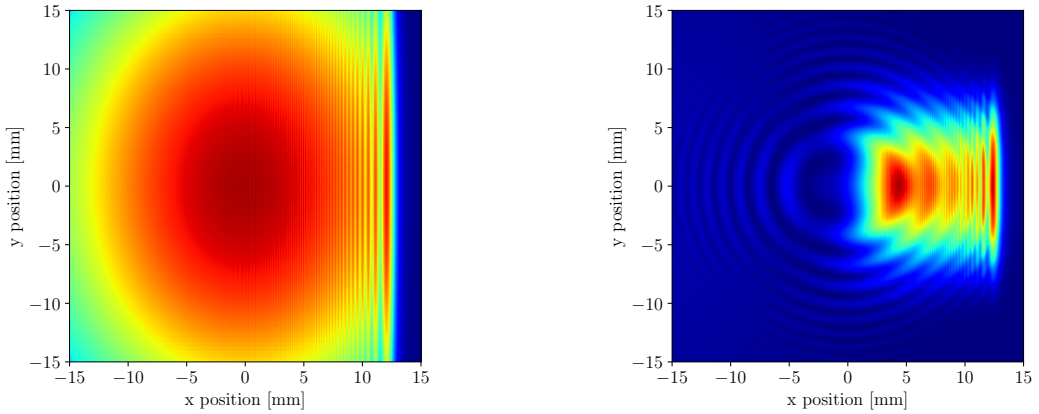

(a) 450 GeV (b) 6800 GeV

Figure 5.8: Simulation of the SR intensity reaching the slit plane at injection and flat-top. The vertical cut on the right side of the light distribution is due to the edge of the extraction mirror, located at $x_m \approx 12\,\text{mm}$

The following two paragraphs present the results of the performance characterization of the BSRI for the injection and flat-top scenarios. The simulations of the complete BSRI system are needed to assess the effects of the finite apertures and the presence of the extraction mirror diffraction at the slit plane, which were not taken into account in the general study of the coherence properties of the wavefront radiated by the LHC source.

Performance at injection energy

Based on the characterization of the coherence properties of undulator radiation, it is expected that the assessed degree of coherence is uniform throughout the entire undulator wavefront at the injection energy. Figure 5.9 displays the degree of coherence obtained from the simulation of the BSRI interferograms for a various slit configurations.

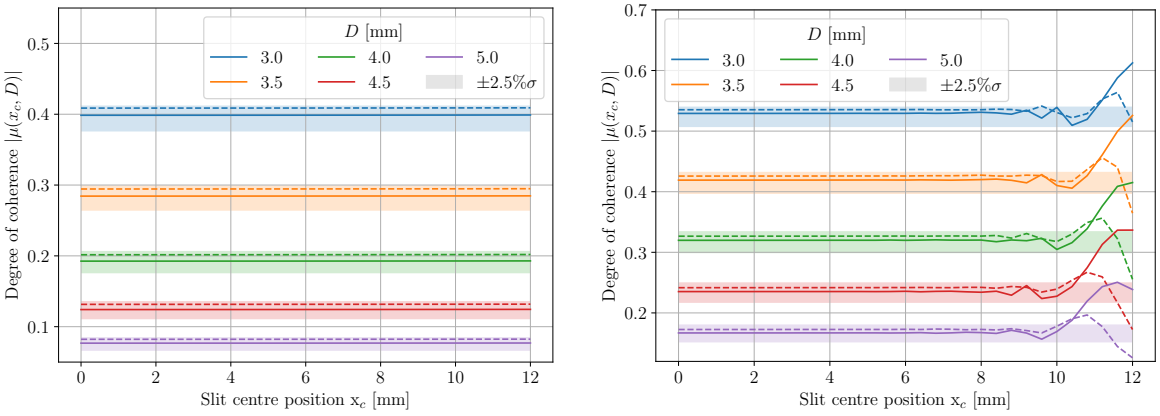

(a) Vertical direction

(b) Horizontal direction

Figure 5.9: Degree of coherence assessed from the BSRI simulations at injection energy. The degree of coherence is simulated at the slit separations of interest for the injection scenario, and at several positions of the horizontal slit centre x_c, fixing the vertical position on the light centre $y_c = 0$. For each slit separation, the simulation is performed with slit widths of $w = 500\,\mu\text{m}$ (solid lines) and $w = 1\,\text{mm}$ (dashed lines). Color bands represent the degree of coherence computed from the input beam size using the VCZ formula, plotted with a beam size tolerance of $\pm 2.5\,\%$. The simulations are performed at the injection operating wavelength of 560 nm.

The uniformity of the degree of coherence is confirmed along the vertical direction, regardless of the position of the slit center and the employed slit separation. The constant value of the degree of coherence, even near the extraction mirror cut, is due to the SR symmetry along the vertical direction, which is not affected by the mirror edge diffraction. The retrieved degree of coherence is compatible with the VCZ prediction, within the required tolerance, for both values of the simulated slit widths. However, a better agreement is found for the narrower 500 µm slits. The discrepancy between the degree of coherence evaluated with the two slit widths can be

attributed to the fact that the slit width of 1 mm is comparable with the typical slit separation. This leads to an "effective" slit separation that differs from the nominal distance between the aperture centres. The effective separation is shorter than the nominal as the radiation intensity increases approaching the optical axis. The higher degree of coherence observed for the wider slits thus originates from the smaller effective slit separation. This problem is not relevant for the narrower slit of 500 µm, as the finite width of these apertures can be neglected compared to the typical slit separation $D \gtrsim 3\,\text{mm}$. The degree of coherence in this configuration perfectly agrees with the VCZ prediction, as expected from the undulator coherence at injection energy.

A similar situation occurs along the horizontal direction. The main difference is the effect of the extraction mirror, which does affect the assessed degree of coherence when the slits are placed in the proximity of the mirror cut. The wavefront sampled by the slits in this region is significantly affected by the fringes of the mirror edge diffraction and the degree of coherence fluctuates accordingly. Nevertheless, this is not a problem in practice as it is sufficient to avoid the region close to the mirror cut and place the slits in the centre of the undulator radiation, where the intensity is also higher.

In conclusion, the simulations performed at injection energy confirm that the BSRI is capable of retrieving the beam size along both directions. The only relevant constraint is that the slit separation should be sufficiently larger than the aperture width. This practically limits the minimum slit separation achievable, thus making it challenging to resolve the narrow decay of the degree of coherence at injection energy, especially in case of large bunches.

Performance at flat-top energy

The performance assessment is more critical at flat-top due to the peculiar characteristics of the two-dipole radiation, which have a significant impact on the coherence of SR. Let us discuss the results of the BSRI simulations, starting from the more straightforward vertical direction depicted in Fig. 5.10a.

The degree of coherence evaluated using square slits of 1 mm × 1 mm (solid lines) exhibits considerable fluctuations with respect to the horizontal slit position, making it difficult to determine a well-defined value of $|\mu(x_c, D)|$. This behaviour is due to the interference between the two dipoles and hinders a reliable assessment of the source size. In addition to the fluctuations, the degree of coherence also shows a decreasing trend as the slit centre moves from the optical axis towards the mirror cut. This behaviour is consistent with the drift of the source distance

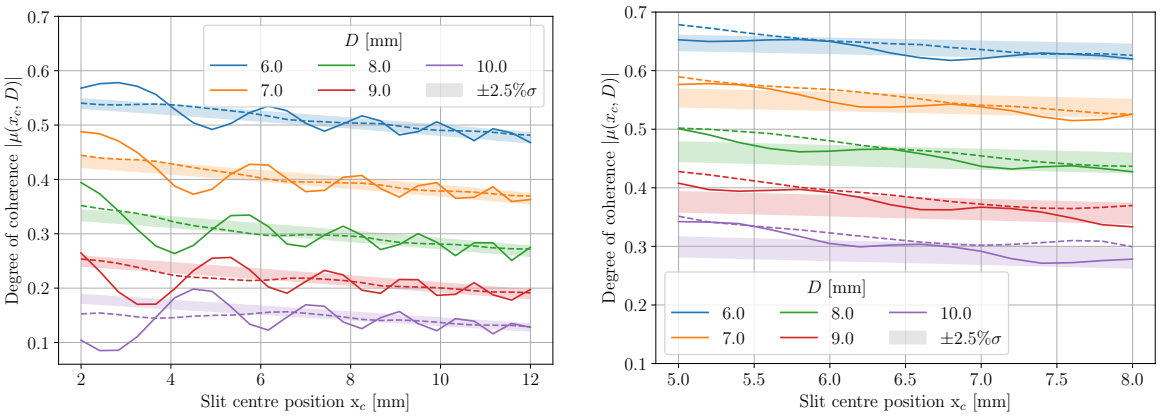

(a) Vertical direction

(b) Horizontal direction

Figure 5.10: Degree of coherence assessed from the BSRI simulations at 6800 GeV. The degree of coherence is simulated for the slit separation of interest for the injection scenario and at several positions of the horizontal slit centre x_c, fixing the vertical position on the light centre $y_c = 0$. Solid lines refer to a slit configuration with square apertures of 1 mm × 1 mm. The dashed lines represent the effect of the dipole interference mitigation discussed in the text. Color bands represent the VCZ prediction with the usual beam size tolerance of ±2.5 %, corrected by the source distance change as a function of the slit horizontal position. The simulation is performed at the operating wavelength of 400 nm.

along the dipole, already mentioned in Sec. 4.4.

The latter effect can be corrected in the same way presented for the coherence map, by redefining the source distance as a function of the horizontal position of the slit centre

$$r_p \approx (z - z_{in})\sqrt{1 - \frac{2\rho x_c}{(z - z_{in})^2}}. \tag{5.10}$$

This expression for the source distance leads to a predicted degree of coherence which is not constant throughout the entire radiation wavefront but decreases as the slits approach the mirror edge. This is fully compatible with the results of the simulation, as the average trend of $|\mu(x_c, D)|$ decreases with x_c. The oscillations around the trend can be mitigated by taking advantage of the finite size of the slits and increasing the slit height to allow at least one full period of the dipole fringes to pass through, thus intrinsically averaging the degree of coherence and damping the fluctuations. The result of this mitigation is shown in the figure as a dashed line and it is in good agreement with the VCZ prediction, which has been corrected by the source distance $r_p(x_c)$. The optimal mitigation was determined to occur at a slit height of $h = 4$ mm. Increasing the slit height beyond this value can negatively impact the correction for the source distance $r_p(x_c)$, which requires short slits to sample light from a well-defined horizontal position x_c.

The simulation results for the horizontal direction are presented in Fig. 5.10b. The qualita-

tive behavior is similar to the vertical case, with an oscillating degree of coherence that decreases as we move from the reference axis to the mirror edge. However, the correction for the source distance and the mitigation of the oscillations are not as effective as in the vertical case. Correcting for the source distance in the horizontal direction is somewhat arbitrary because the two slits sample the wavefront at different horizontal positions. Evaluating the source distance at the slit center lacks a strict physical interpretation and serves as an average distance considering the longitudinal extension of the dipole. The oscillations are minimally influenced by the slit height since the slits are essentially parallel to the dipole interference fringes. To perform averaging, increasing the slit width rather than the height would be more suitable. However, this option is not convenient as it would significantly affect the effective slit separation. Hence, even with the largest available slit height of 15 mm (dashed line), no substantial difference is observed. Lastly, it is worth mentioning that the range of allowable slit center positions in the horizontal direction is limited to ensure that neither of the apertures falls outside the available light spot. The horizontal direction at flat-top energy is also one of the few cases where the correction of the visibility is not negligible. Looking at the SR intensity distribution of Fig. 5.8b, the light transmitted through two vertical apertures is unlikely to be the equal and the correction for the imbalance becomes relevant if one of the apertures approaches the edge of the available light.

To summarize, the behavior of the BSRI at flat-top energy is less straightforward compared to the injection energy. However, there are corrective measures that can be implemented to mitigate the challenges associated with the synchrotron radiation emitted by the interfering dipoles. These measures allow retrieving the beam size from the interferogram visibility, using the Van Cittert and Zernike theorem. While the mitigation strategy is more successful in the vertical direction, achieving the desired $\pm 2.5\,\%$ accuracy in beam size, it proves to be more challenging in the horizontal direction, where the accuracy target is only marginally met.

5.4 Experimental validation of the setup

To conclude the description of the BSRI implementation, we present a collection of experimental results performed to validate the response of the setup and its dependence on various experimental parameters. The measurements performed to characterize the accuracy of the BSRI as a transverse beam size measurement instrument deferred to Chapter 6, entirely dedicated to this subject.

Figure 5.11a showcases a typical interferogram captured by the BSRI. To enhance the interference pattern's quality, a reference image of the background noise is obtained by shutting the light path and subsequently subtracted from the interferogram. The system magnification is adjusted to ensure that the central lobe of the interferogram covers the entire detector, to achieve the best spatial resolution of the fringe pattern. This requirement, necessary to record high-quality interferograms, results in a large region of the detector constantly exposed to light, which negatively affects the lifetime of the image intensifier. As a result, the BSRI is limited to sporadic use, mainly for verifying the stability of SR telescope measurements. Conversely, SR telescopes are well-suited for continuous monitoring since the smaller light spot created by the imaging system can be scanned, thereby diluting the light intensity over a the entire active aread of the detector. The vertical profile extracted from the two-dimensional interferogram is presented in Fig. 5.11b. The analytical fit performed using the interference pattern formula exhibits a perfect overlap with the experimental data. The constant visibility observed across the entire fringe pattern confirms that temporal coherence effects do not distort the interferogram shape. Moreover, the interference fringes remain well-contained within the intensity envelopes, which are calculated by combining the single-slit diffraction distributions using Eq.5.6.

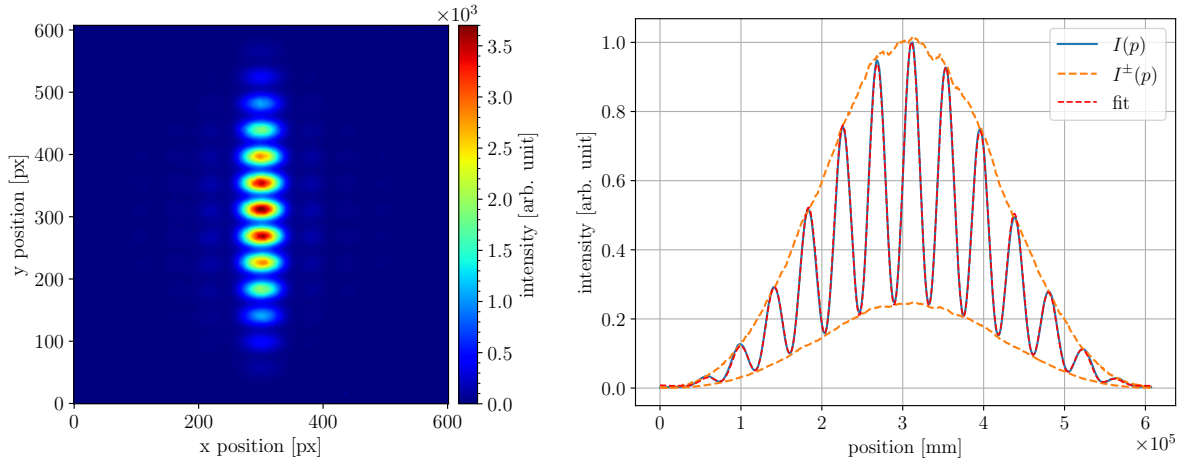

(a) (b)

Figure 5.11: In (a), example of a two-dimensional interferogram recorded on the BSRI detector. In (b), the profile of the intensity fringes is extracted and fitted to retrieve the visibility. The intensity envelopes obtained from the single-slit profiles are plotted as a verification.

Figure 5.12 presents a measurement performed to assess the stability of the visibility measurement. During a standard fill for physics at flat-top energy, four nominal bunches with slightly different sizes were continuously measured using the BSRI. The system demonstrates

its capability to resolve the variations in visibility associated with the evolution of the bunch size during the fill. The fluctuation in the visibility measurement exhibits a standard deviation smaller than 0.5 %. Assuming a linear relationship between the visibility and the source size, valid for small variation around a reference operating visibility, the statistical error of ±0.5 % in visibility corresponds to the same fluctuation in beam size, or twice this value in emittance. This level of precision exceeds the standard performance of the BSRT, where the measurement typically fluctuates with a statistical error of ±3 % in beam size. It is worth noting that the relative error of the BSRT could also be improved by increasing the gain of the detector, although this is normally minimized to extend the lifetime of the image intensifier.

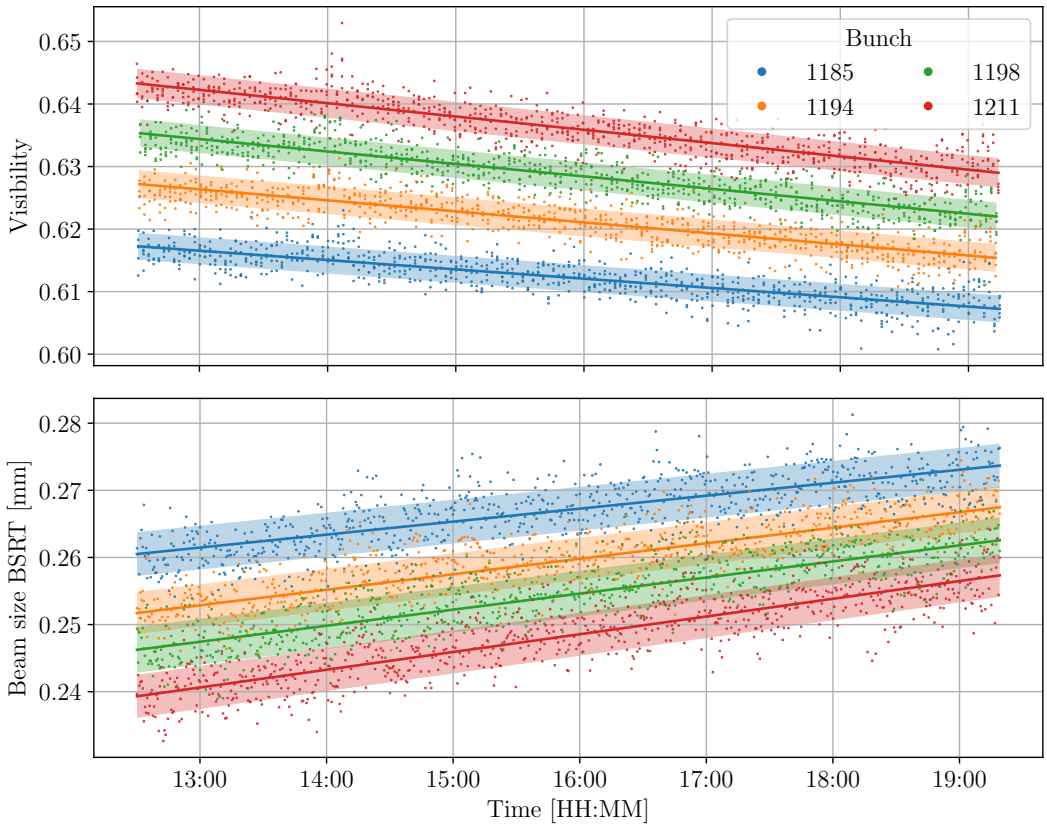

Figure 5.12: Evolution of the visibility measured by the BSRI for nominal bunches during a physics fill at flat-top energy. The bottom plot shows the corresponding evolution of beam size measured by the BSRT for reference. The decrease in measured visibility throughout the fill is consistent with the increase in beam size observed by the BSRT. This behavior can be attributed to bunch collisions that result in the increase of the bunch transverse emittance.

A more quantitative comparison between the BSRT and BSRI beam size measurements is presented in Fig. 5.13. This measurement was performed during a "scrubbing" run, which is a stage of the accelerator commissioning process where multiple bunches are allowed to circulate at injection energy to prepare the machine for the intensity ramp-up. A characteristic of the

scrubbing fill is that the bunches in the tails of each train tend to increase their transverse size due to electron cloud effects [67]. The BSRI effectively detects this phenomenon and provides beam size measurements that are fully compatible with the values obtained from the BSRT for all the bunches in the measured train.

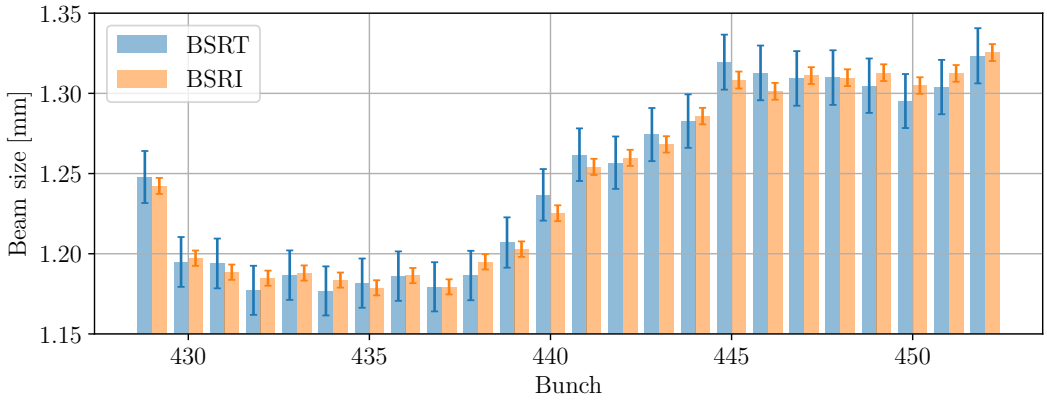

Figure 5.13: Horizontal beam size of 24 consecutive bunches belonging to a train. Measurement performed during a scrubbing fill at injection energy. The beam size measured by the BSRI and BSRT are compared for each bunch. The error bar represent the statistical error associated with the two measurements.

5.4.1 Effect of the exposure time

The intensity captured by the detector can be adjusted with a combination of attenuation filters, gain of the image intensifier, and exposure time of the digital camera. While the attenuation filters and intensifier gain only affect the amount of light reaching the camera, changing the detector exposure time also affects the time response of the system. Long exposure times are sensitive to phenomena such as air turbulence, mechanical vibrations of the setup, or beam instabilities that can blur the interferogram pattern and decrease the assessed visibility.

To investigate the impact of exposure time on the visibility of the interferogram, measurements were conducted by varying the exposure time between 200 ms and 50 µs. The former represents a long exposure time that produces a very stable pattern whereas the latter is the shortest exposure time permitted by the camera. The resulting average visibility and its statistical fluctuation, evaluated over a sample of 30 frames per exposure time, are displayed in Fig. 5.14.

One notable finding is the relatively consistent visibility maintained throughout the entire range of exposure times investigated. As expected, the visibility shows a slight increase at shorter

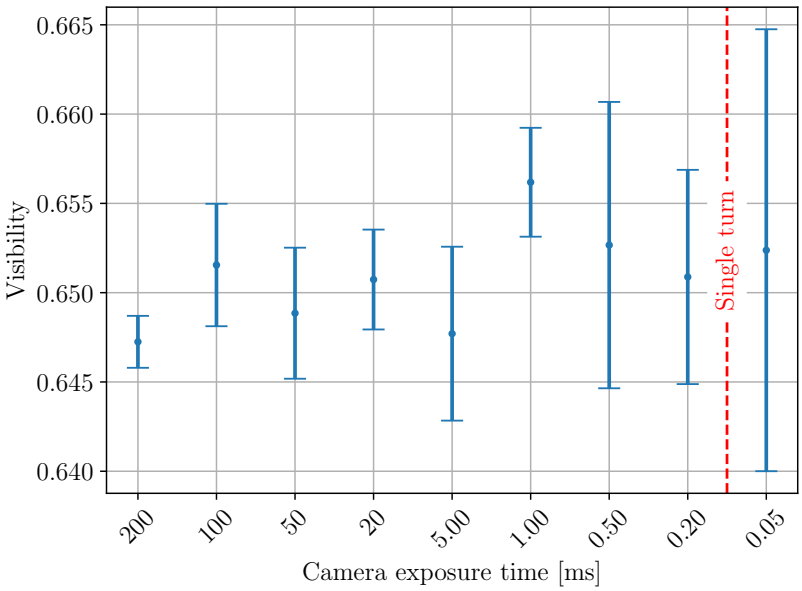

Figure 5.14: Measured interferogram visibility as a function of the camera exposure time. The average visibility value is extracted from a sample of 30 interferograms and its standard deviation is plotted as the vertical error bars.

exposure times, suggesting that experimental factors may have a minor impact on visibility at longer exposures. However, the increase in average visibility is also accompanied by a larger standard deviation. The increase of standard deviation becomes apparent when comparing the quality of the interferograms captured at the two extreme exposure cases, as depicted in Fig. 5.15. The 50 µs exposure interferogram exhibits considerably noisier fringes compared to the cleaner pattern observed at 200 ms, resulting in a significant fluctuation in the fitted visibility. It is important to note that the 50 µs exposure duration is shorter than the LHC revolution period of approximately 90 µs, which means that the actual exposure to synchrotron light is limited to a few nanoseconds due to the bunch length. Despite this extremely short duration, the average visibility remains consistent, indicating that factors such as air turbulence and mechanical vibrations, which operate on a much slower timescale, do not significantly impact the BSRI measurements.

For standard measurements at flat-top energy, an exposure time of 50 ms is typically employed to obtain a good fringe quality without setting the intensifier gain its maximum limit. At injection energy, the exposure time is increased to 200 ms to cope with the less intense undulator SR. At present, shorter exposure times do not offer substantial improvements in system performance, as the real-time image processing operates at a relatively slow frame rate of approximately 1 fps. However, this finding suggests that future upgrades of the BSRI could potentially

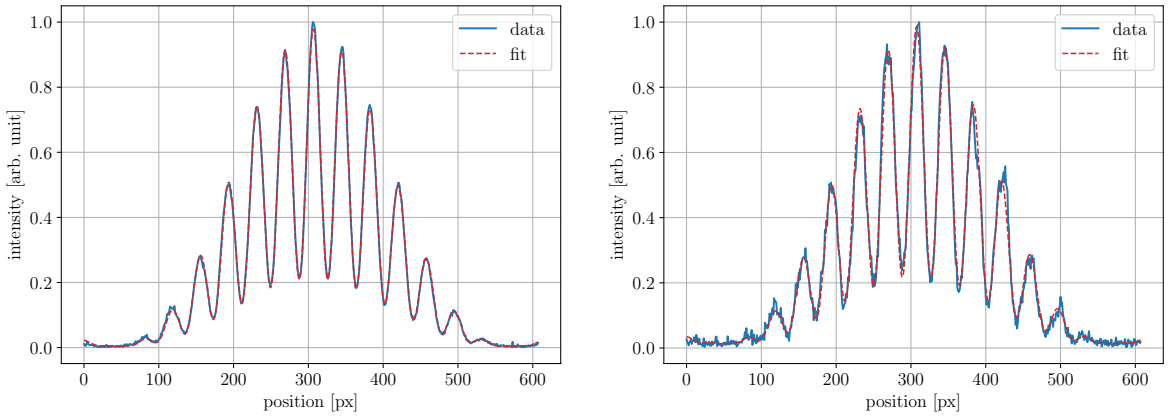

(a) Camera exposure 200 ms

(b) Camera exposure 50 µs

Figure 5.15: Example of interferograms acquired at the minimum and maximum exposure times of Fig. 5.14. The single-turn interferogram (b) is acquired maximising the light at the detector, selecting the largest available slit height, extracting all attenuation filters and setting the maximum image intensifier gain. Furthermore, these measurements were performed during a special fill with high-intensity bunches of 1.8×10^{11} particles.

adopt shorter exposure times to enhance measurement speed without significant compromise to measurement stability.

5.4.2 Visibility uniformity across the SR wavefront

An important experimental test is the validation of the system response when the slits are transversely displaced to map the visibility across the incoming wavefront. Although this type of measurement is not directly relevant to operational scenarios, where the slits are typically held in a stationary configuration or a slit separation scan is performed around a fixed slit center, it serves as a valuable tool for investigating the coherence properties of the wavefront and benchmarking the degree of coherence against simulations. Fig.5.16 and Fig.5.17a present two examples of such visibility maps, which were measured at injection energy and 6800 GeV, respectively.

The measurement carried out at injection energy confirms that the system accurately reproduces the uniform visibility expected from the degree of coherence of the undulator radiation. The observed variations, smaller than 1 %, are consistent with typical statistical fluctuations of the visibility assessment. This result not only validates the uniformity of the undulator radiation coherence but also serves as evidence of the overall optical quality of the system, indicating that it does not introduce any significant wavefront distortions.

The visibility map obtained at flat-top energy exhibits a distinct pattern, which originates

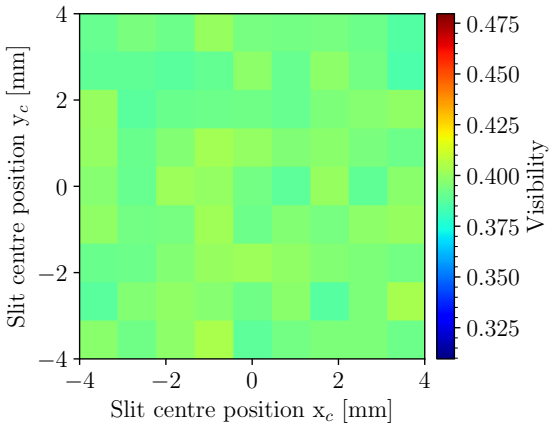

Figure 5.16: Interferogram visibility at 450 GeV mapped as a function of the slit centre position, using a vertical slit configuration with a fixed slit separation of $D = 3\,\text{mm}$. The color scale has the same range as that of Fig. 5.17, allowing for a direct comparison of the uniformity of visibility between injection and flat-top energies.

from the interference between the two D3 dipoles. The measured visibility oscillates following a regular pattern, characterized by concentric rings centred at the light reference axis. The pattern detected in the BSRI visibility map agrees with the results obtained from the simulation of the same slit position scan, providing qualitative validation of the system response to dipole interference effects. However, despite the qualitative agreement between the observed and simulated patterns, the former exhibits some imperfections not present in the latter. Several factors may contribute to this discrepancy, with the most probable explanation being the presence of brighter spots in the SR distribution observed at the slit plane, as depicted in the flat-top image shown in Fig. 3.13. However, these local deviations do not significantly affect the overall response of the system, which remains consistent across the entire visibility map.

5.4.3 Dependence on polarization

To conclude this collection of experimental observations, let us examine the influence of the polarization angle on the interferogram parameters. At high energy, the linear polarizer is essential to avoid superposition between horizontal and vertical polarization components. As discussed in Sec. 3.6, the horizontal polarization of the single particle field has a continuous phase over the entire wavefront, while the vertical polarization undergoes an inversion of sign across the orbit plane, resulting in a π phase jump at $y = 0$. This phase jump associated with the vertical polarization is detectable by the BSRI, as it contributes to the phase term ϕ_{12} of the interferogram fringes. In a vertical slit configuration, whenever the two apertures

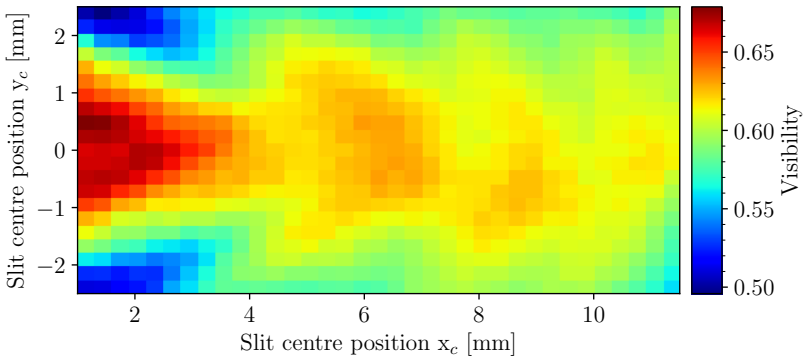

(a) Experimental

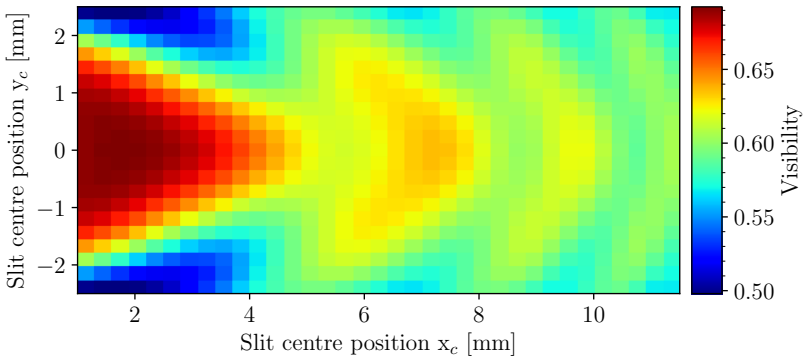

(b) Simulated

Figure 5.17: Interferogram visibility, as a function of the slit centre position at 6800 GeV. Slit position scan performed using a vertical slit configuration with fixed slit separation $D = 7$ mm.

sample points on opposite sides of the orbit plane, the two wavefronts arrives at the centre of the interferogram in anti-phase, leading to an intensity minimum. Conversely, for horizontal polarization, an intensity maximum is observed at the interferogram centre. This behavior is confirmed by the polarizer angle scan presented in Fig. 5.18, where the fitted phase ϕ_{12} is 0 (or 2π) for horizontal polarization and π for vertical polarization.

The visibility of the interferogram remains constant for both horizontal and vertical polarizations individually, as the fringe contrast is not affected by the phase difference ϕ_{12}. However, when the polarizer is set at intermediate angles, the two polarization components combine, leading to the superposition of interferograms with opposite phases. This combination results in a suppression of the visibility, highlighting the importance of using a linear polarizer for accurate visibility measurements. The decay in visibility is less pronounced around the horizontal polarization, primarily due to the higher intensity associated with the horizontal polarization.

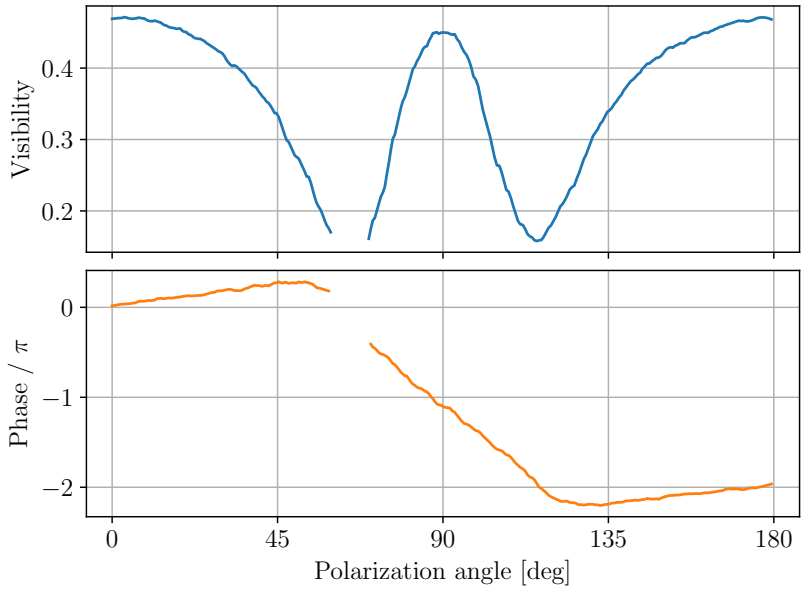

Figure 5.18: Measured interferogram visibility and phase, as a function of the radiation polarization angle. The horizontal polarization corresponds to an angle of 0° (or 180°). The polarization scan is performed at 6800 GeV, with a vertical slit configuration centred at $(x_c, y_c) = (6, 0)$mm and a slit separation of $D = 7$ mm. Some points between 45° and 90° are missing because the fit fails at very low visibility.

Chapter 6

Performance assessment of the synchrotron radiation interferometer

The accuracy and performance of the synchrotron radiation interferometer as a transverse diagnostic instrument are investigated in this chapter.

In the initial part of the chapter, the results from the interferometer are compared to the reference data obtained from wire scanners during the LHC emittance calibration fill. At injection energy, visibility measurements show good agreement with the reference values derived from wire scanner profiles, through the Van Cittert and Zernike theorem. At flat-top energy, a consistent discrepancy appears, with the measured visibility systematically lower than the reference. Extensive investigations have been conducted to identify the source, yet the ultimate cause of the discrepancy has not been isolated. Several observations suggest an intrinsic physical origin, currently not accounted for in simulations. To address this issue, an empirical model was developed to correct the raw visibility data obtained from the interferometer and restore the compatibility with the wire scanner reference.

Section 6.3 delves into the deployment of the interferometer in an operational scenario, where the instrument must operate with a limited range of visibility points to reconstruct the beam profile and estimate the transverse emittance. The diffraction limit represents the ultimate constraint for the interferometer in this context, making it particularly challenging to accurately assess emittance for small bunches at flat-top energy.

Finally, the chapter includes a comparison with emittance values assessed by the CMS detector through an emittance scan, to investigate the overall consistency of transverse diagnostics at the LHC.

6.1 Comparison between synchrotron radiation interferometer and wire scanner measurements

The emittance calibration fill is a special LHC fill where a limited number of bunches, covering the full range of LHC emittances, are injected and accelerated. This reduced number of bunches allows for the operation of wire scanners, which are employed to measure the transverse beam size at regular intervals throughout the entire fill. The primary objective of this fill is to calibrate the synchrotron radiation telescopes (BSRT), enabling them to provide accurate emittance measurements in regular physics fills. Additionally, this fill presents an ideal opportunity to validate and assess the performance of novel systems for transverse diagnostics, such as the synchrotron radiation interferometer (BSRI). Emittance calibration fills are regularly conducted during the accelerator run, to ensure a constant update of the BSRT calibration. The measurements presented in the following refer to the two emittance calibration fills of the 2022 LHC run, identified by the fill numbers 7915 (4^{th} July) and 8479 (24^{th} November).

The emittance calibration fill follows a sequence similar to that of a regular LHC cycle. For both beams, a limited number of bunches with five different emittances are injected, corresponding to the maximum beam intensity allowed by wire scanners. The transverse emittance is determined in the initial stage of the LHC injector complex, at the injection of the Proton Synchrotron Booster (PSB). The H^- ions from LINAC 4 are stripped and the resulting protons are injected into the PSB rings to produce bunches with nominal emittances ranging between 1 µm and 5 µm. These bunches are subsequently accelerated through the complex until they reach the LHC, where the actual emittance is verified by means of wire scanners. Once the injection process is completed, the calibration at the injection energy is performed, followed immediately by beam acceleration. It is important to limit the time spent at injection energy due to the tendency of the bunches, particularly the smaller ones, to experience transverse blow-up. Once the acceleration phase is completed, the beams are adjusted and collisions occur at the interaction points. This stationary regime lasts for several hours, enabling systematic measurements to take place.

The transverse emittance alone does not offer a complete characterization of the transverse distribution of the bunches involved in the calibration fill. Wire scanner profiles reveal that the bunches exhibit significant tails, deviating from the simple Gaussian distribution. As a result, the assumption of a double-Gaussian distribution, introduced in Sec. 4.3, becomes necessary to

better describe the transverse profile of the bunches and allow a consistent comparison between the wire scanners and the interferometer measurements.

6.1.1 Reference measurements from wire scanners

Wire scanner measurements are continuously performed during the calibration fill to monitor the evolution of the transverse beam distribution. Each time a wire scanner is activated, the beam is intercepted twice: once during the inward motion and a second time during the outward motion of the wire. These two measurements are treated independently, and the resulting profiles are considered separately in the following analysis. The transverse size of the desired bunches is determined by fitting the profiles. The normalized emittance is calculated from the beam size using Eq. 1.16. Dispersive effects are neglected, taking advantage of the minimal dispersion function within the LHC straight sections.

Figure 6.1 provides an overview of the wire scanner beam size measurements performed throughout the fill. The fill starts with the injection of the larger bunches. Once the instrumentation setup is completed, the remaining bunches are injected. The machine remains at injection energy for approximately 15 minutes to allow for the calibration of the BSRT and, in parallel, perform a few slit separation scans with the interferometer. Wire scanner measurements reveal a noticeable increase in size at injection energy, exceeding 20 % for the smaller bunches. As the accelerator energy ramp begins, there is a sudden decrease in the transverse beam size. Ideally, the beam size evolution during the energy ramp follows the $1/\sqrt{E}$ trend due to the adiabatic damping. After reaching the flat-top energy of 6.8 TeV, the machine goes through the sequence to initiate collisions. These steps include reducing the beam size at the interaction point (referred to as "squeeze"), approaching the beams (referred to as "adjust"), and optimizing the luminosity to achieve the final stage of "stable beams." These operations primarily change the beam characteristics at the interaction points, with minimal impact on the particle distributions at the diagnostics location. Therefore, for the purpose of our analysis, we can assume stationary beam conditions once the accelerator reaches the flat-top energy.

The emittance evolution of the bunches relevant to the comparison with the synchrotron radiation interferometer is illustrated in Fig. 6.2. Ideally, this plot should exhibit a set of constant emittance values within the desired range of 1 µm to 5 µm, with increments of 1 µm. However, the actual picture is not as straightforward. The emittance at injection does not exactly coincide with the nominal values requested to the PSB, due to the bunch propagation through the injector

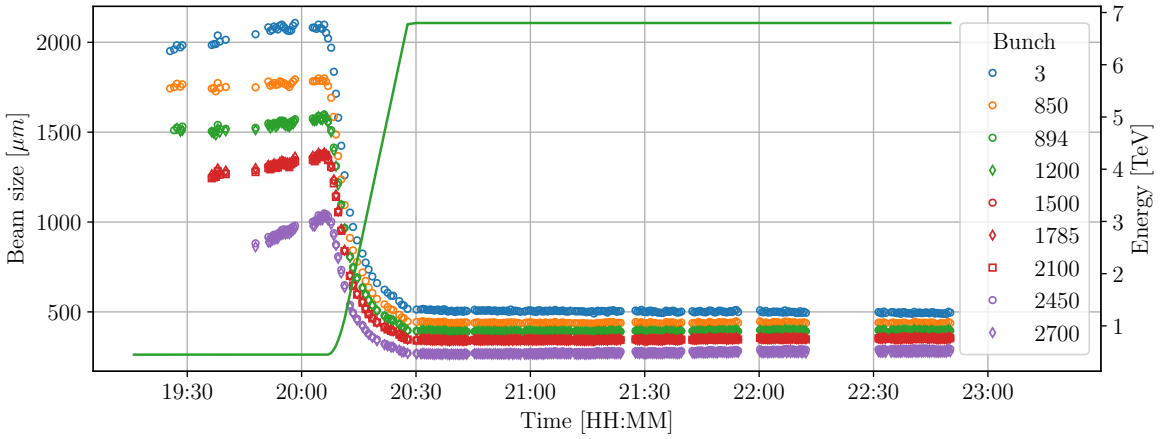

(a) Vertical direction

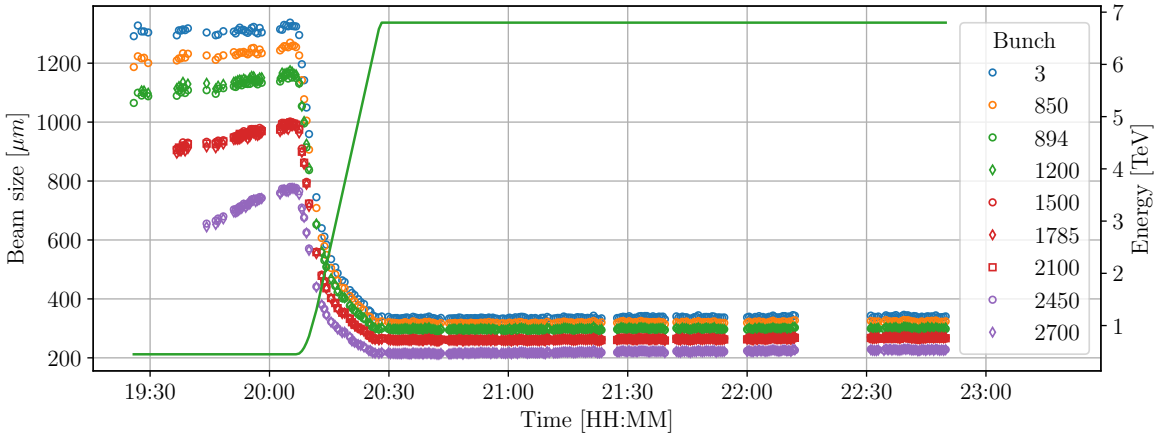

(b) Horizontal direction

Figure 6.1: Beam size measurements obtained by wire scanners during the calibration fill 8479 for Beam 1 in both horizontal and vertical directions. Each data point represents the average size obtained from inward and outward scans. Bunches injected with the same nominal emittance are grouped by color, using different markers. The solid green line corresponds to the beam energy. The marker and color bunch notation remains consistent throughout the chapter, helping the readability of the plots.

complex. At injection energy, the emittance evolution reflects the same increase observed in the beam size, particularly apparent for the smaller bunches. Fluctuations are present during the energy ramp and can be attributed to transients in the accelerator optics, which slightly changes between injection and flat-top energies. Despite these temporary fluctuations, the overall emittance remains well preserved during the ramp, with a slight increase observed for the smaller bunches in the horizontal direction. The preservation of the normalized emittance during the energy ramp also implies that the beam size indeed exhibits the expected $1/\sqrt{E}$ behavior of adiabatic damping. At flat-top energy, the values of the emittance remain stable for several hours. The only noticeable effect is a slight increase in the emittance of bunch 2450 in the

vertical direction, which becomes distinguishable from the bunch 2700, injected with the same nominal emittance of 1 µm.

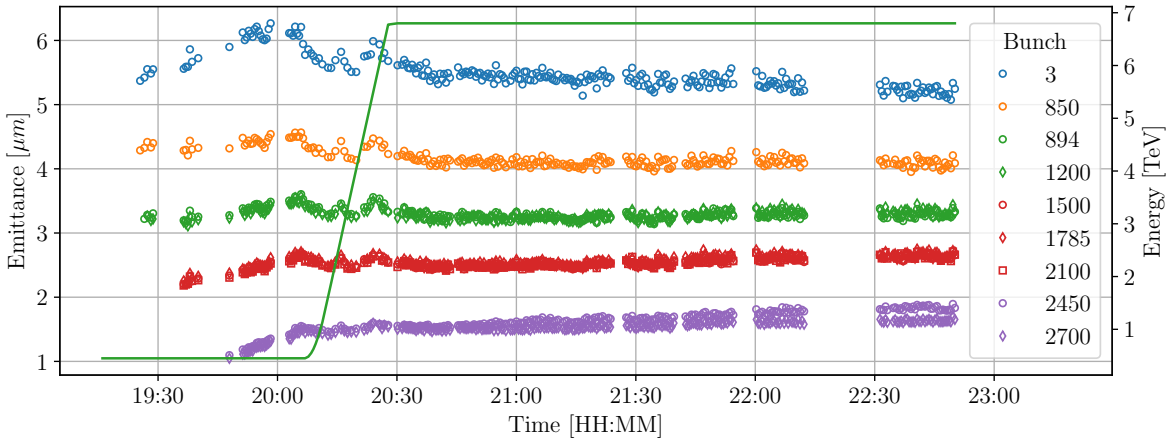

(a) Vertical direction

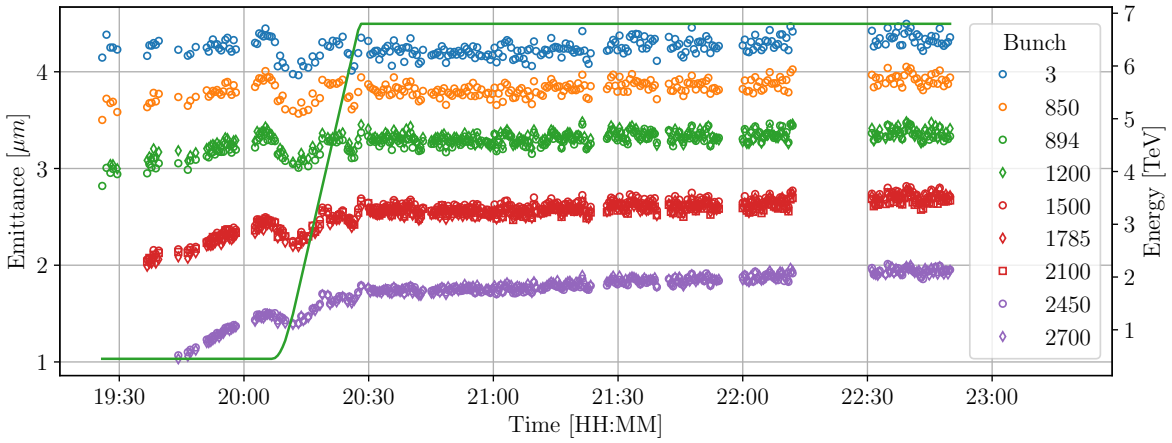

(b) Horizontal direction

Figure 6.2: Reference emittance obtained from the wire scanner profiles during the calibration fill 8479 for Beam 1 in both horizontal and vertical directions. The structure of the plot is the same as Fig. 6.1.

6.1.2 Wire scanner profiles

The simple Gaussian analysis provides a practical characterization of the transverse distribution of bunches. However, additional degrees of freedom are required to accurately describe the real profile of the bunches during an emittance calibration fill.

Figure 6.3 illustrates wire scanner profiles for two representative bunches with different emittances, acquired in both transverse directions. These examples demonstrate a clear deviation from a Gaussian function, with noticeable tails present in the profiles of the smaller bunches.

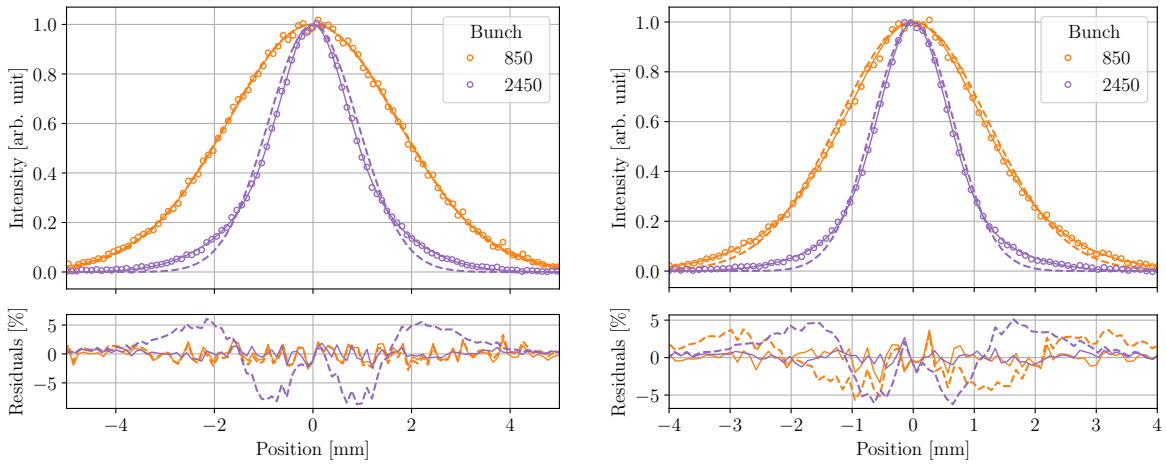

(a) Vertical direction

(b) Horizontal direction

Figure 6.3: Examples of Wire scanner profiles recorded during the injection phase of the calibration fill, for two bunches of different nominal emittance. The circles are the experimental data points, the dashed line is the simple Gaussian fit while the solid line represents the fit performed with the weighted combination of two Gaussian distributions.

A weighted combination of two Gaussian distributions is capable of accurately reproducing the experimental data. Therefore, the best approximation for the actual bunch profile is the double-Gaussian distribution

$$f(\xi) = c\,\frac{1}{\sqrt{2\pi}\sigma_1} e^{-\frac{1}{2}\frac{\xi^2}{\sigma_1^2}} + (1-c)\,\frac{1}{\sqrt{2\pi}\sigma_2} e^{-\frac{1}{2}\frac{\xi^2}{\sigma_2^2}}, \tag{6.1}$$

previously introduced in Eq. 4.27.

To systematically assess the deviation of the bunch profiles from the Gaussian distribution throughout the fill, we can analyze the relative difference between the emittance of the double Gaussian distribution, $\varepsilon_{dg} = c\varepsilon_1 + (1-c)\varepsilon_2$, and the "effective" emittance obtained from the simple Gaussian fit, ε. The result of this comparison is illustrated in Fig. 6.4. The analysis confirms that more significant deviations from the simple Gaussian distribution occur for the smaller bunches, regardless of the transverse direction, and persist throughout the entire fill. The deviation for the bunches with a nominal emittance larger than 3 µm is typically below 10 %, indicating that their profiles can be adequately approximated using the simple Gaussian distribution. At injection energy, the profiles of the injected bunches tend to converge towards a more Gaussian distribution as they circulate in the machine. This behaviour is particularly pronounced for the smaller bunches and, in combination with the increase of the emittance observed in Fig. 6.2, can be attributed to a blow-up of the core fraction of particles. A similar effect

is observed for bunch 2450 at flat-top energy, where the increase in emittance is accompanied by a reduction of the deviation from the Gaussian distribution.

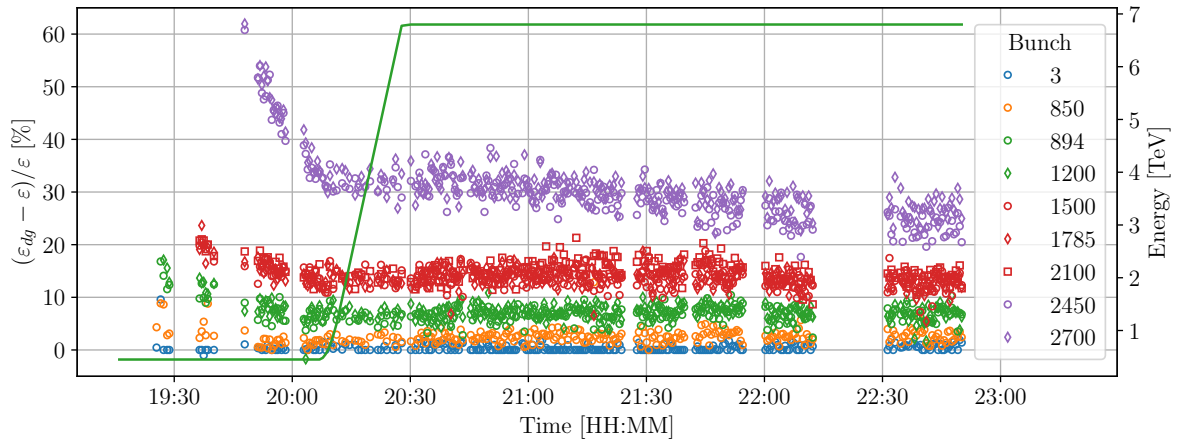

(a) Vertical direction

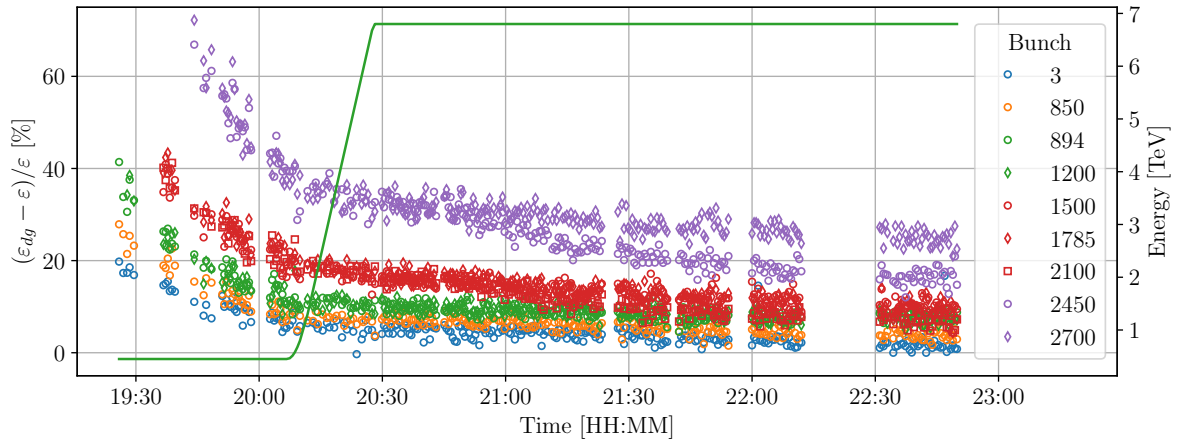

(b) Horizontal direction

Figure 6.4: Relative difference between the emittance computed with a double Gaussian and a simple Gaussian fit of the wire scanner profiles during the emittance calibration fill 8479.

6.1.3 Comparison between wire scanners and synchrotron radiation interferometer data

When comparing the wire scanner and synchrotron radiation interferometer measurements, a few aspects need to be considered. Firstly, the two instruments measure the beam at slightly different locations along the machine, requiring the propagation of the reference measurement from the wire scanner to infer the beam distribution at the synchrotron radiation source. Secondly, the wire scanner measurements clearly show that the smaller bunches significantly deviate from the Gaussian distribution. This prevents the applicability of Eq. 5.9 to infer the beam size from a

single visibility measurement and requires instead a scan of slit separations to probe at least a fraction of the visibility decay. Lastly, the transverse distribution of the bunches evolves over time, thus limiting the comparison between wire scanner and interferometer only to adjacent measurements. This section outlines the methodology used for comparing the results from the two instruments.

The output of a slit separation scan is a discrete set of visibility values acquired for the selected bunches and slit separations. Since this measurement process usually takes only a few minutes, the characteristics of the bunches remain unchanged within this time interval. Therefore, all wire scanner measurements conducted during the interferometer scan can be averaged to obtain the reference measurement. Under the validity of the Van Cittert and Zernike theorem, the visibility measured by the interferometer as a function of the slit separation corresponds to the Fourier transform the bunch profiles. The expected visibility decay for double Gaussian profiles can be determined by applying Eq. 4.28

$$V(D) = c\, e^{-\frac{1}{2}\frac{D^2}{\sigma^2_{coh,1}}} + (1-c)\, e^{-\frac{1}{2}\frac{D^2}{\sigma^2_{coh,2}}}, \tag{6.2}$$

being $\sigma_{coh,i} = \lambda r_p / 2\pi\sigma_i$ the coherence area associated with each of the two Gaussian contributions and c the fraction of core particles. Assuming that the core and tails contributions propagate independently as two overlapping Gaussian beams, the values of σ_i can be transported from the location of the wire scanner to the synchrotron radiation source using the standard principles of transverse beam dynamics, while the core fraction remains preserved along the ring. The standard deviations σ_i and the core fraction c are determined, and propagated, separately for each wire scanner profile. To obtain a unique reference curve $V_{ref}(D)$ for comparing the visibility decay measured by the interferometer, the wire scanner measurements performed during the slit separation scan need to be averaged.

Averaging the fit parameters is not a suitable approach due to the existence of multiple combinations of (σ_1, σ_2, c) that can yield similar wire scanner profiles. Taking the average of each parameter separately often results in an inaccurate assessment of the reference visibility curve[1]. Instead, a preferable approach is to compute the curve $V(D)$ for each profile individually and then average the resulting set of curves to obtain the reference visibility decay $V_{ref}(D)$.

[1]For example, an almost Gaussian profile with a standard deviation σ can be accurately reproduced by parameter combinations like $(\sigma, \sigma, 0.5)$ and $(\sigma, 0, 1)$. Averaging these parameters yields $(\sigma, \sigma/2, 0.75)$, which does not represent the actual shape of the original profile

This method ensures a more reliable estimation of the reference visibility curve by averaging the variations in the parameters across different profiles.

The reference visibility is evaluated at the slit separations used in the interferometer scan. Finally, the reference and measured visibility points are conveniently presented in a scatter plot, offering a visual representation of the agreement between the two datasets.

6.1.4 Injection energy

We will now present the results of the comparison between the synchrotron radiation interferometer and wire scanner measurements, starting with the scans performed at injection energy. The injection scenario is conceptually straightforward and not affected by any potential difficulties arising from the source complexity. Therefore, the agreement between the expected reference and the observed visibility serves as a fundamental validation of the accuracy of the setup.

Figure 6.5a presents the results of a slit separation scan conducted at injection energy along the vertical direction. The measured visibility points align with the reference curves inferred from the wire scanner profiles, indicating a good agreement. Despite the visibility associated with the larger bunches being relatively low and not suitable for accurate measurements, the scatter plot of Fig. 6.5b confirms a satisfactory agreement for all measured bunches. The linear regression of the measured points perfectly overlaps with the expected reference, and overall, the dataset remains confined within a beam size tolerance of $\pm 2.5\,\%$. Similar results are observed for the horizontal direction using data from a slit separation scan performed just before the start of the energy ramp, reported in Fig. 6.6.

The importance of considering the exact shape of the bunch profile when comparing wire scanner and interferometer data is illustrated in Fig. 6.7. For the smaller bunches, the reference visibility curves obtained through a simple Gaussian fit of the wire scanner profiles diverge significantly from the visibility points measured by the interferometer. This deviation is expected, as the distribution of these bunches differs considerably from a simple Gaussian function. The discrepancy between the two approaches vanishes for the larger bunches, which are in fact well-described by a Gaussian distribution.

The fact that the visibility critically depends on the shape of the bunch profile is not problematic at the current stage of the analysis, as the objective of this section is to verify that the visibility points measured by the interferometer align with the reference curve obtained from the wire scanner. However, it does have practical implications when the interferometer is used in

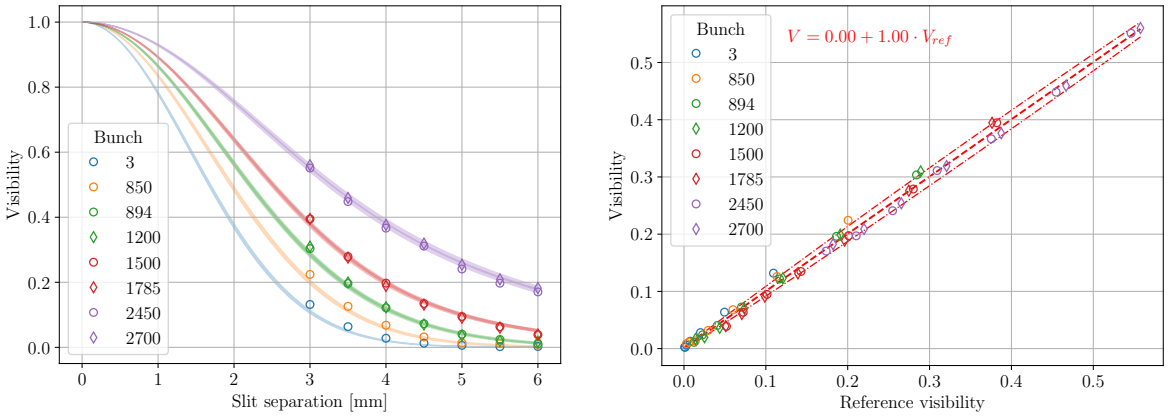

(a) (b)

Figure 6.5: Assessment of the BSRI accuracy along the vertical direction at injection energy. In (a), the comparison between the reference visibility inferred from the wire scanner profiles (lines) and the visibility measured by the interferometer (markers). For each bunch, the average reference visibility is plotted as a solid line inscribed in a color band which represents the statistical uncertainty associated with the wire scanner measurements. In (b), the scatter plot of reference and measured visibility. The linear regression $V(V_{ref})$ is plotted as a red dashed line and the computed coefficients annotated on the plot. The red dash-dotted lines represent a tolerance of 2.5 % beam size around the ideal trend $V = V_{ref}$, plotted as a grey dashed line (not visibile in this case as perfectly overlapping with the linear regression).

situations where the shape of the profile is not known a priori, and it needs to be reconstructed from the available visibility points. This constraint is part of a broader intrinsic limitation of the interferometer, and will be discussed in more detail in Sec. 6.3 when addressing the deployment of the interferometer in an operational scenario.

6.1.5 Flat-top energy

The radiation emitted by the smaller beams at flat-top energy exhibits a larger coherence area, which allows for a wider range of slit separations to be used in probing the visibility decay. The results of two slit separation scans conducted at flat-top energy are shown in Fig. 6.8a and Fig. 6.9a, representing the vertical and horizontal planes respectively. In contrast to the injection energy, a significant discrepancy is found between the measured visibility points and the reference curves. In particular, the measured visibility is systematically lower than the corresponding target value. This behavior is qualitatively similar for both vertical and horizontal scans. The only quantitative distinction is that the smaller horizontal beam size leads to a range of visibility values that are generally larger compared to the vertical direction. The occurrence of a "loss of visibility" at flat-top energy is not an isolated phenomenon limited to a single occurrence. It consistently manifests in all scans conducted during both emittance calibration

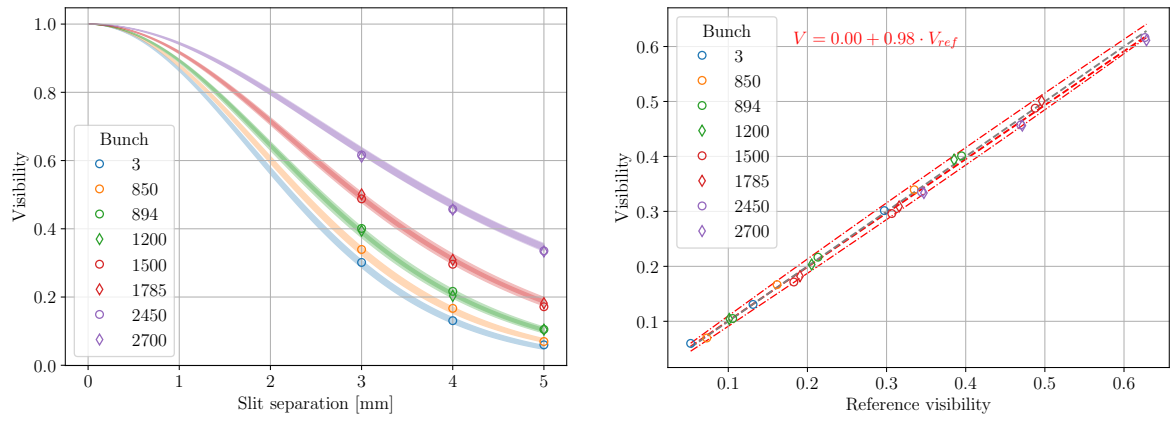

(a) (b)

Figure 6.6: Assessment of the BSRI accuracy along the horizontal direction at injection energy. The structure of the two plots is the same as Fig. 6.5.

fills and therefore deserves further investigations. Despite the optimum operating wavelength for the flat-top case being set at 400 nm based on simulations, the majority of measurements were conducted at 560 nm to compensate for the lower-than-expected visibility using a longer wavelength. However, scans were also conducted at 400 nm, and the results obtained at both operating wavelengths are fully compatible, as detailed in a dedicated paragraph in Sec. 6.2 below.

The scatter plots of Fig. 6.8b and Fig. 6.9b provide a more quantitative representation of the discrepancy between the measured and reference visibility. As expected from the plots of the visibility curves, the measured points clearly fall outside the beam size tolerance of ±2.5 %. The deviation primarily manifests as a constant offset rather than a different slope. Furthermore, the points do not align well along a consistent trend, and their scatter varies depending on the specific bunch. In this scenario, linear regression is not a suitable method to describe the relationship between the measured and reference visibility. Even if the average trend of the measured points is corrected using the parameters determined through linear regression, the points would still be scattered around a region corresponding to a relative error in beam size larger than ±20 %, significantly above the desired tolerance.

These results indicate that the raw visibility measured by the interferometer cannot be directly used for an absolute measurement of the beam size using the procedure outlined in Chapter 4 and based on the Van Cittert and Zernike formula. However, a promising finding is that the visibility curves exhibit a consistent trend and a clear correlation with the different size of the bunches. This suggests that, upon implementation of an effective algorithm to correct

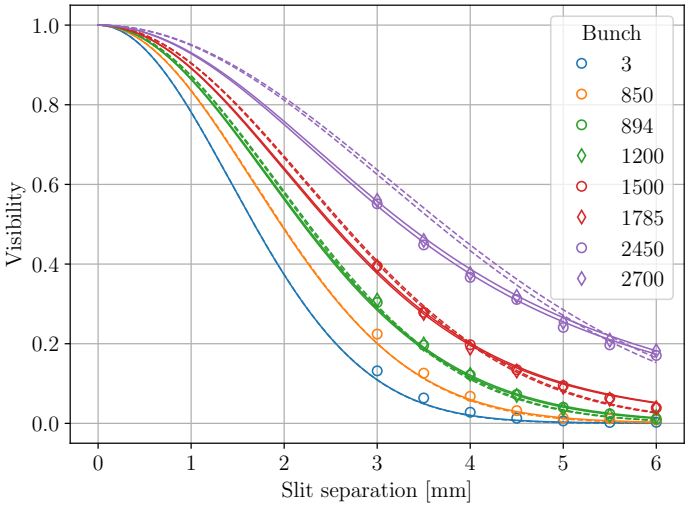

Figure 6.7: Effect of profile Gaussianity on visibility curves at injection. The solid lines represent the reference curves obtained through a double Gaussian fit of the wire scanner profiles, while the dashed lines are derived from a simple Gaussian fit. The color bands representing the reference uncertainty are omitted. Data from the same scan as Fig. 6.5 is used for this comparison.

for the loss of visibility, the interferometer could still serve as a redundant and independent, yet calibrated, instrument for transverse diagnostics.

6.1.6 Correction of loss of visibility

The aim of this paragraph is to find an empirical model that can be used to correct the raw visibility and restore agreement with the reference values. This model is essential not only for making the interferometer data usable but it could also help the investigation of the physical origin of the visibility loss, which will be the subject of Sec. 6.2.

Several parameters have been considered in search of a consistent model to explain the observed discrepancy. Eventually, good results were achieved by introducing a slight modification to the linear regression $V(V_{ref})$, incorporating a dependence on the slit separation

$$V(V_{ref}, D) = a_3 V_{ref} D + a_2 V_{ref} + a_1 D + a_0, \tag{6.3}$$

where the coefficients a_i are left as fitting parameters of the points in the (V_{ref}, D) space.

The results of the fitting operation are illustrated in Fig. 6.10a and Fig. 6.11a, for the same vertical and horizontal scans presented in the previous section. The fitting function of Eq. 6.3 represents a surface in the three dimensional space (V_{ref}, D, V). Despite the linear dependence on V_{ref} and D, this surface is not a plane due to the non-zero value of the coefficient a_3 associated to

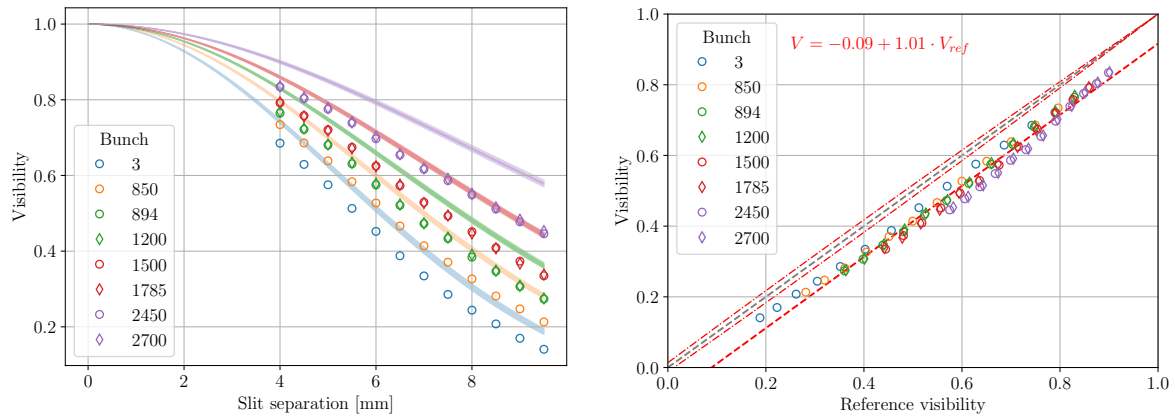

(a) (b)

Figure 6.8: Assessment of the BSRI accuracy along the vertical direction at flat-top energy. The structure of the two plots is the same as Fig. 6.5. Measurement performed at the operating wavelength of 560 nm.

the mixed term. The agreement between the measured data points and the fitted surface shows that this empirical model is effective in reproducing the experimental dataset for all bunches. Figure 6.10b and Fig. 6.11b offer a more quantitative representation of the fit quality. The raw visibility is corrected according to the relationship of Eq. 6.3 and the result is plotted against the reference visibility. The corrected points perfectly align along the reference. The spread among different bunches vanishes, and all points are well confined within the required tolerance. The correction of the visibility loss is also effective in the horizontal direction. However, as expected in the more challenging horizontal plane, the fitting process yields larger residuals. As a result, the scatter among the bunches can still be observed in the corrected data, which slightly exceeds the beam size tolerance of ±2.5 %. The fit error could be further reduced by using a quadratic surface as fitting function. However, this option is excluded to maintain a relatively simple relationship for the visibility correction and to avoid the risk of overfitting the experimental dataset.

Reproducibility of the visibility correction

To ensure the practical implementation of the visibility correction in an operational scenario, it is crucial to assess the stability of the coefficients a_i defined in Eq. 6.3 across various slit separation scans and, ideally, over longer periods of time across different calibration fills. An immediate way to assess the reproducibility of the visibility correction is by applying the coefficients calculated in one calibration fill to correct the raw data from a different fill. The results of this test are

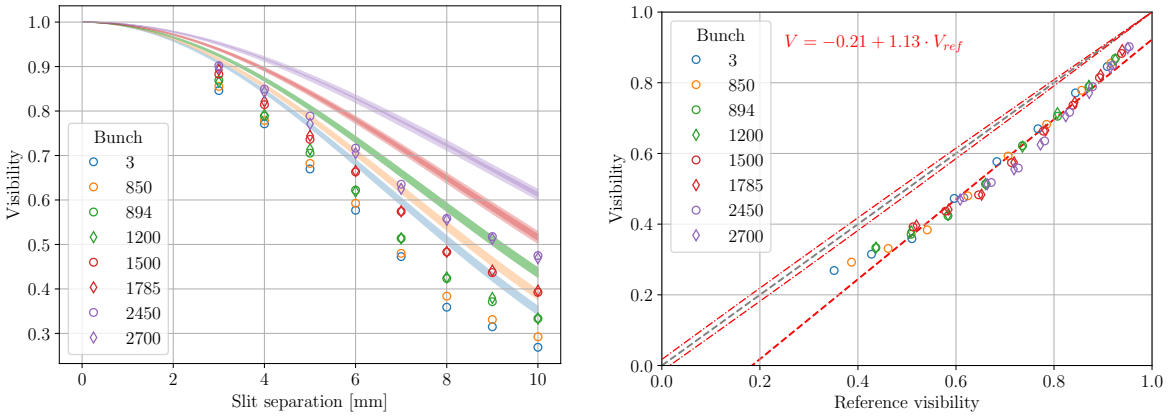

(a) (b)

Figure 6.9: Assessment of the BSRI accuracy along the horizontal direction at flat-top energy. The structure of the two plots is the same as Fig. 6.5. Measurement performed at the operating wavelength of 560 nm

shown in Fig. 6.12, where the visibility raw data acquired during the emittance calibration fill of November 2022 is corrected using the coefficients computed from the fill of July 2022.

The reproducibility of the correction function is validated in both directions. The correction using coeffiecients from a different fill is slightly less effective compared to the cases where the raw data were corrected using coefficients computed on the same dataset. Nevertheless, the linear regression of on the corrected data confirms that the visibility loss is effectively compensated. The spread of points around the reference trend remains within acceptable limits, therefore preserving the tolerance achieved with the correction computed on the same dataset.

Although no significant modifications were made to the interferometer setup, there was a gap of several months between the two calibration fills. During this period, the instrument was frequently operated, and interventions were conducted on other equipment located on the same optical table. Despite these factors, the correction coefficients remained consistent, demonstrating the stability of the visibility correction. This stability is fundamental for the practical use of the interferometer, as the model of Eq. 6.3 can be adopted as a calibration of the device, ensuring reliable and consistent measurements over time.

6.2 Investigations on loss of visibility at flat-top energy

The previous section introduced a strategy to address the loss of visibility at flat-top energy by utilizing an empirical model that incorporates a correction based on the slit separation, and a set of experimental coefficients. In the following discussion, we study the problem of the

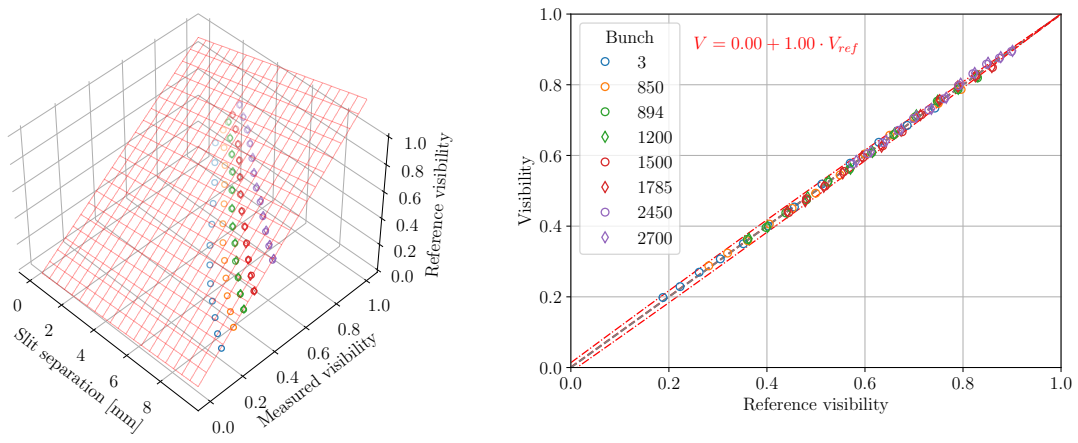

(a) (b)

Figure 6.10: Loss of visibility correction along the vertical direction at flat-top energy. In (a), a visualization of the $V(V_{ref}, D)$ fit of Eq. 6.3 and, in (b), the scatter plot of the corrected visibility points.

loss of visibility at flat-top energy and provide a summary of the investigations performed to identify the underlying cause of this discrepancy. The analysis conducted so far has not yielded conclusive results, and the ultimate source of the issue remains unidentified. Nevertheless, several potential factors that could induce a loss of visibility have been ruled out, and certain observations suggest that the loss of visibility is likely to originate from intrinsic properties of the synchrotron radiation source.

Defects in the experimental setup

A potential explanation for the loss of visibility in the recorded interferogram is related to defects in the experimental apparatus. Imperfections in the optical components can cause smearing or blurring of the light distribution at the detector, resulting in reduced contrast of the interference fringes. The same phenomenon may occur as a consequence of mechanical vibrations or air turbulence in the optical line. Interferometers are particularly sensitive to these phenomena compared to imaging systems because they rely on the phase information of the wavefront, which is easily distorted by wavefront errors, air turbulence or mechanical vibrations.

Nevertheless, optical defects in the apparatus are not a plausible explanation for the observed loss of visibility, as they would equally affect measurements at both flat-top and injection energy. Moreover, measurements at injection energy are even more sensitive to optical defects due to the broader emission of the undulator, which covers a larger area of the optical surfaces compared to the narrow light spot of dipole radiation. However, no discrepancies were

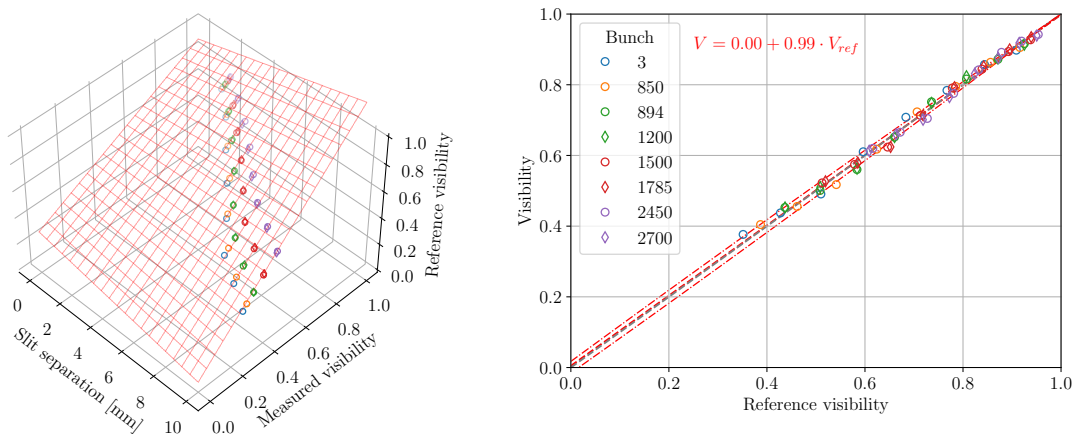

(a) (b)

Figure 6.11: Loss of visibility correction along the horizontal direction at flat-top energy. In (a), a visualization of the $V(V_{ref}, D)$ fit of Eq. 6.3 and, in (b), the scatter plot of the corrected visibility points.

observed at injection energy, and the measured visibility remained consistently uniform across all the available wavefronts, as demonstrated in Sec. 5.4. On the other hand, the stability of the visibility measurements reported in Fig. 5.14, even when the exposure time of the detector is reduced to the few nanoseconds of the single bunch passage, rules out mechanical vibrations or air turbulence as potential causes for the loss of visibility.

In conclusion, it is unlikely that the observed discrepancy between the reference and the measured visibility at flat-top energy is due to defects in the experimental apparatus.

Effect of background light

The presence of background light at the detector is another common cause of loss of contrast in interference patterns. Background light may originate from various sources, including spurious contributions of the synchrotron radiation itself or residual light that is not properly shielded. In the case of interest, constant backgrounds due to stray light would not affect the visibility assessment because the image processing accounts for the subtraction of a reference background. The presence of spurious contributions from synchrotron radiation cannot be ruled out a priori. Reflections on the vacuum chamber while the radiation is still in the beam pipe, reflections from the optical components[2], and leakage of spurious wavelengths from the bandpass filters are all potential sources of such contributions.

To evaluate the potential impact of background light, multiple simulation scenarios were

[2]Although most of the components have antireflective features, a small fraction of light is inevitably reflected, which can produce aliases of the interferogram at the detector.

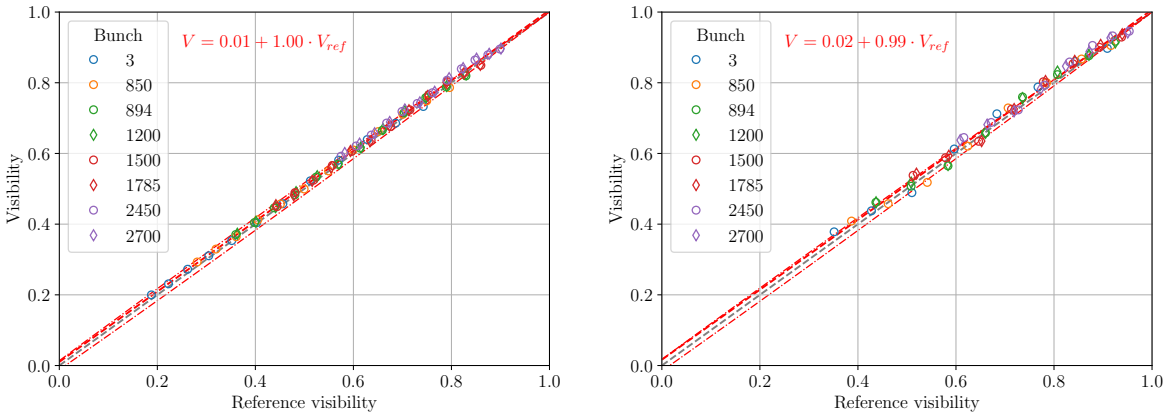

(a) Vertical direction

(b) Horizontal direction

Figure 6.12: Reproducibility of the visibility correction between the two calibration fills of 2022. The scatter plots depict slit separation scans conducted in both the horizontal and vertical directions. The scans were performed in fill 8479 and the corrections were applied using the coefficients calculated during fill 7915.

performed. The simulations used the interferograms predicted by the reference measurements as input and introduced several types of background light patterns. These patterns included aliases of the interferograms, shifted to simulate spurious reflections, interferograms with different fringe periodicity to simulate spurious wavelengths leaking through the filter, and light distributions that may not follow the interferogram function and could simulate stray light reaching the detector. The interferograms resulting from these simulations were then fitted to assess the discrepancy between their visibility and the reference visibility used as input. The objective of these tests was to reproduce a situation where the visibility deviates from the reference in way similar to the behaviour observed in experiments, as shown in Fig. 6.8b.

Despite numerous attempts, it is not possible to replicate the observed discrepancy. In particular, the bunch-dependent deviations are not observed in any manipulation of the input interferogram. While various tests result in a visibility trend that deviates from the reference, the resulting visibility points still exhibit a consistent alignment along a common trend. The spread among the bunches could be artificially induced by introducing bunch-dependent corrections, such as adapting the parameters of the background light to match the observed discrepancy. However, these corrections are considered arbitrary and therefore excluded, since there are no physical reasons to support their application.

Physical origin of the visibility loss

Common experimental causes of visibility loss have been investigated and ruled out as explanations for the discrepancy observed in the interferometer data at flat-top energy. This section gathers a few considerations that suggest that these discrepancies are actually inherent physical characteristics of the LHC synchrotron radiation source, which currently elude the simulations.

The consistency of the loss of visibility provides the initial evidence of a physical origin. The observed discrepancy in the visibility curves follows a regular pattern that exhibits high reproducibility across various scans and fills, while also demonstrating qualitative similarity in both planes.

An additional indication that the visibility loss is not an experimental artifact can be deduced from the empirical model found for the visibility correction. The raw visibility, for all points and bunches, is nearly perfectly corrected by incorporating only a dependence on the slit separation. This dependence is not accidental as the slit separation is one of the parameters, alongside the wavelength and the source distance, which determines the spatial coherence, thus the fundamental coordinate that governs the transverse coherence of a wavefront. These findings suggest that the empirical formula used to correct the raw visibility in Eq. 6.3 may actually represent a first-order expansion of an underlying physical model that provides the exact correction of the VCZ theorem for the specific case under study.

This assumption can be further probed by studying the dependence of the measured visibility with respect to the wavelength. According to the Van Cittert and Zernike theorem, visibility curves at different wavelengths should overlap when plotted as a function of the spatial frequency $\nu = D/(r_p\lambda)$ rather than the slit separation alone. Figure 6.13 reports a comparison between slit separation scans performed at the two operating wavelengths of the setup at flat-top energy. The overlap of the two observation wavelengths is validated as the data points from both scans align well along a common trend. It is important to note that while this scaling law was derived from the VCZ theorem, the concept of spatial frequency is a fundamental principle in physical optics, governing the propagation of optical fields. The alignment between two wavelengths strengthens the assumption of a physical origin for the observed discrepancy. However, this evidence alone cannot be considered as an exclusive proof of the VCZ theorem, as alternative models could potentially exhibit the same scaling law.

In conclusion, many independent observations support a physical origin of the visibility loss at flat-top energy. The recorded discrepancy is extremely consistent and common experimental

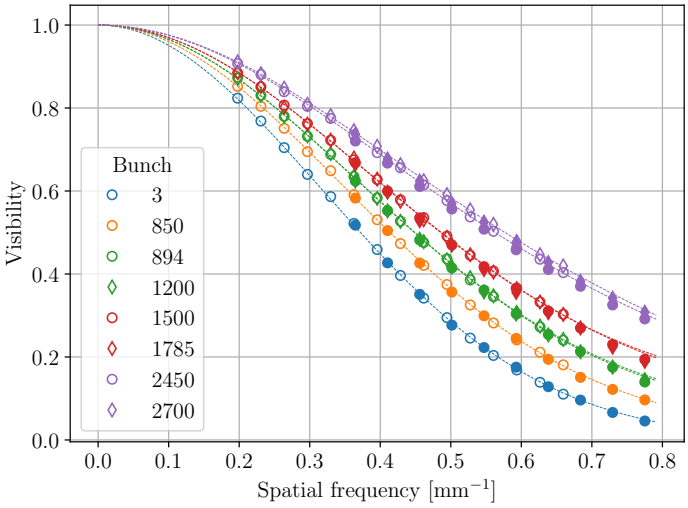

Figure 6.13: Comparison between the visibility measured at 560 nm (empty markers) and 405 nm (filled markers) at flat-top energy, for a vertical slit separation scan. The double Gaussian fit of the visibility points is plotted as dashed lines, to highlight the common trend of visibility data both wavelengths. In order to overlap scans recorded at different wavelengths, the horizontal axis is expressed as spatial frequency instead of the usual slit separation.

sources of visibility loss have been investigated and ruled out. While the deviation from the VCZ theorem is not currently predicted by simulations, there is no reason to distrust the simulation tools themselves, as they are based on a well-established code like Synchrotron Radiation Workshop, which has accurately predicted other aspects of the LHC source, such as the two-dipole interference, even before they were directly observed. Further investigations are therefore required to expand the analysis of potential sources, searching for elements that have not yet been included into the simulations and could account for the observed discrepancy.

6.3 Deployment of the synchrotron radiation interferometer in an operational scenario

The results presented thus far demonstrate the compatibility between the visibility measured by the interferometer and the reference visibility inferred from the wire scanner profiles. At injection energy, the agreement is achieved applying the VCZ theorem to relate the bunch transverse distributions to the degree of coherence of the radiation. At flat-top energy, although the measured visibility can still be related to the reference, the direct comparison using the simple VCZ formula proved to be ineffective. However, compatibility can be restored by applying an empirical formula to correct the raw measured visibility. This correction has been demonstrated

to be consistent for all bunches and scans, and reproducible across different fills.

The objective of this section is to assess the performance of the interferometer in an operational scenario, where the aim is not only to establish a correlation between the interferometer and wire scanner data but also to provide independent and accurate beam size measurements. In this context, the primary limitation of the interferometer lies in the limited range of available slit separations, which hinders the direct measurement of the complete decay of visibility and therefore the reconstruction of the complete transverse particle distribution.

Let us first consider the case of a perfectly Gaussian bunch. In this ideal scenario, the only unknown parameter of the visibility decay is the coherence area σ_{coh}, which can be retrieved from a single visibility measurement at a fixed slit separation. Once the visibility of the interferogram is measured, and corrected if necessary, the corresponding source size can be computed as $\sigma = \lambda r_p/(\pi D)\sqrt{1/2\log(1/V)}$, derived inverting Eq. 5.9. This approach heavily relies on the assumption of a Gaussian bunch profile, and its accuracy is dictated by the accuracy of the single visibility measurement. Studies performed during the emittance calibration fill confirmed that the single visibility measurement is accurate within an emittance tolerance of $\pm 5\,\%$ at injection energy. Upon correcting the raw visibility to compensate for the loss of visibility, comparable results were achieved for the flat-top scenario. The tolerance target was successfully validated for the vertical plane, while it was only marginally met for the more challenging horizontal case.

The situation changes significantly when the assumption of Gaussian bunches cannot be made a priori, and the shape of the bunch profile needs to be obtained based on the visibility data itself. This realistic scenario is discussed in Fig. 6.14a, where a slit separation scan at flat-top from the emittance calibration fill is provided as an example to discuss this limitation.

Due to the limited extent of available light distribution, the interferometer can only probe a finite range of slit separations. As a result, the behavior of visibility decay at larger separations remains completely unknown. This limitation would not be problematic if the bunch profile were known a priori, as the visibility tail could be extrapolated accurately based on the fit of the available points. Otherwise, multiple solutions are possible and the extrapolated behaviour is essentially dictated by the guess parameters used for the fit. In the specific example presented in the figure, the measured points are fitted with a double-Gaussian function, employing four distinct combinations of guess parameters $(c, \sigma_{coh,1}, \sigma_{coh,2})$. The resulting profile reconstruction is entirely arbitrary and yields widely scattered values of effective emittance, rendering them of limited usefulness in an operational scenario. The situation can be partially improved by

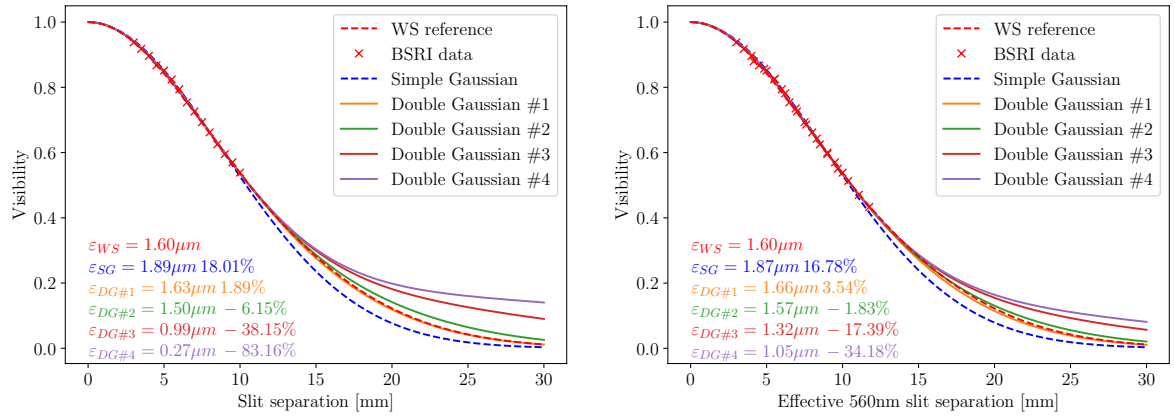

(a) 560 nm (b) 560 nm and 400 nm

Figure 6.14: Deployment of the interferometer in an operational scenario. In (a), the visibility decay of bunch 2700 (red crosses) from Fig. 6.8 is fitted with a simple Gaussian function (blue dashed line) as well as multiple double-Gaussian functions (solid lines) using different combinations of guess parameters. The effective emittance obtained from each fit is indicated on the plot, along with the reference profile and the corresponding reference effective emittance from the wire scanner. In (b), a scan performed at 400 nm is superimposed to the previous. The physical slit separation D of the latter scan is scaled to $D \times 560/400$ to ensure compatibility with the 560 nm dataset, according to the scaling law based on the spatial frequency definition. The same fitting procedure is repeated for the combined dataset.

performing slit separation scans at various wavelengths and merging the measured visibility points using the spatial frequency scaling law outlined in the previous section, as illustrated in Fig. 6.14b. Including the shorter wavelength in the visibility scan expands the range of available slit separations and helps to reduce the spread of the tails, thus decreasing the uncertainty on the emittance assessment.

The inability to systematically reconstruct the complete visibility decay has a significant impact on the scans conducted at flat-top energy, particularly for smaller bunches. These cases are characterized by visibility decay that typically extend beyond the range of the available light. This represents a fundamental limitation of the LHC synchrotron radiation interferometer, which is unable to fully reconstruct the bunch profile. The origin of this constraint lies in the diffraction limit. To effectively minimize the uncertainty in emittance, a potential solution would involve significantly reducing the wavelength and operating in the far ultraviolet domain, as the synchrotron light telescopes do. However, several experimental constraints hinder the implementation of this option, with the most notable challenges being the high sensitivity to optical defects at such short wavelengths and the significant magnification required to compensate for the otherwise narrow fringe periodicity. A more practical approach is to reduce the degrees of freedom in the visibility fit by fixing the core fraction c and allowing the two standard

deviations of the double Gaussian function to be the free parameters. Although this solution affects the self-consistency of the interferometer emittance measurement, as it requires prior knowledge about the shape of the bunch profile, satisfactory results were achieved by fixing a typical value for the core fraction $c = 0.6$ and leaving the standard deviation parameters to fit the available experimental data points.

In the vertical direction, the assessed emittance exhibits deviations of less than $\pm 4\,\%$ for bunches with a nominal emittance $\varepsilon \gtrsim 3\,\mu\text{m}$. However, the diffraction limit introduces a slight increase in uncertainty to $\pm 6\,\%$ for bunches within the nominal LHC emittance range of $2\,\mu\text{m} \lesssim \varepsilon \lesssim 3\,\mu\text{m}$. For the smallest recorded bunches of $1.5\,\mu\text{m}$, discrepancies larger than $\pm 10\,\%$ are observed. These situations can be mitigated by including data from the 400 nm wavelength, thus reducing the relative errors by a margin of 2 %. The situation is slightly worse for the horizontal direction. Although the uncertainty for larger bunches remains below the accuracy target of $\pm 5\,\%$, the smaller bunches with an emittance of $1.5\,\mu\text{m}$ experience significant relative errors, sometimes close to $\pm 12\,\%$.

It is important to emphasize that these figures are applicable to cases where the bunch profile is not known a priori. In scenarios where the bunch is known to follow a Gaussian distribution, or an accurate distribution is available from an independent source, the interferometer has been shown to meet the required specifications of $\pm 5\,\%$ emittance error accuracy.

6.3.1 Comparison with data from emittance scans

The emittance measurements performed at flat-top energy using synchrotron radiation monitors exhibit an unavoidable correlation, as both the telescopes and the interferometer rely on corrections derived from the wire scanner data. The comparison between the two instruments remains important in order to monitor any variations or drifts in their respective results. However, the emittance scans performed by the experiments at the interaction points offer an independent measurement which can be used to assess the consistency of the overall LHC transverse diagnostics.

A good opportunity to compare measurements from the synchrotron radiation monitors and the experiments is a special LHC run dedicated to Van der Meer (VdM) scans. In this series of fills, approximately 150 nominal bunches are circulating and several emittance scans are performed by the experiments. While the primary objective of the VdM program is to calibrate the luminosity detectors of the experiments [68], it also provides ideal conditions for

cross-comparison among the LHC transverse diagnostic instruments.

Figure 6.15a provides a visual comparison between the vertical emittance measured by the synchrotron radiation telescope and the interferometer for all bunches in Beam 1. The BSRI emittance measures systematically a larger values than the BSRT. The discrepancy is approximately 7 % for the smaller bunches, but decreases to less than 3 % for the larger bunches exceeding 2.5 µm. This deviation may suggest a potential drift in the BSRT calibration, but it could be also attributed to the limited performance of the interferometer in resolving the emittance of very small bunches.

The luminosity detectors of the LHC experiments provide bunch-by-bunch measurements that can be compared with the data from the synchrotron radiation monitors. However, the intrinsic limitation of the emittance scan is that it can only provide the average emittance of each pair of colliding bunches. The instantaneous luminosity, measured as a function of the beam separation, is only sensitive to the overlap between the two beams, and the distributions of each beam cannot be isolated. For each pair of colliding bunches, the emittance scan can provide the average emittance

$$\varepsilon_{avg} = \gamma_{rel}\frac{\Sigma^2}{2\beta^*} \triangleq \frac{\varepsilon_{b1} + \varepsilon_{b2}}{2}, \tag{6.4}$$

where $\Sigma^2 = \sigma_{b1}^2 + \sigma_{b2}^2$ represents the variance obtained from the convolution of the transverse distributions of the two colliding bunches, β^* the betatron function at the interaction point and γ_{rel} the usual relativistic factor. In case of a finite crossing angle, Eq. 6.4 includes an additional contribution accounting for the bunch longitudinal size and the value of the crossing angle itself. To eliminate additional sources of uncertainty, the emittance scans conducted by CMS are considered for comparison with the vertical emittance measurements discussed earlier, since the crossing angle at IP5 lies on the horizontal plane.

Direct comparison between emittance measurements obtained from the interferometer and the emittance scan data is not feasible since a BSRI setup is currently only available for Beam 1. Nevertheless, a direct comparison can be made between data from CMS and the BSRT to gain additional insights into the agreement between the BSRT and the BSRI. The correlation between average emittances measured by CMS and the BSRT is illustrated in Fig.6.15b. The comparison reveals that the BSRT tends to underestimate the results from the experiment, slightly beyond the typical uncertainty associated with the emittance scan [69]. This discrepancy may confirm

a slight calibration drift in the BSRT, resulting in an underestimation of the beam emittance.

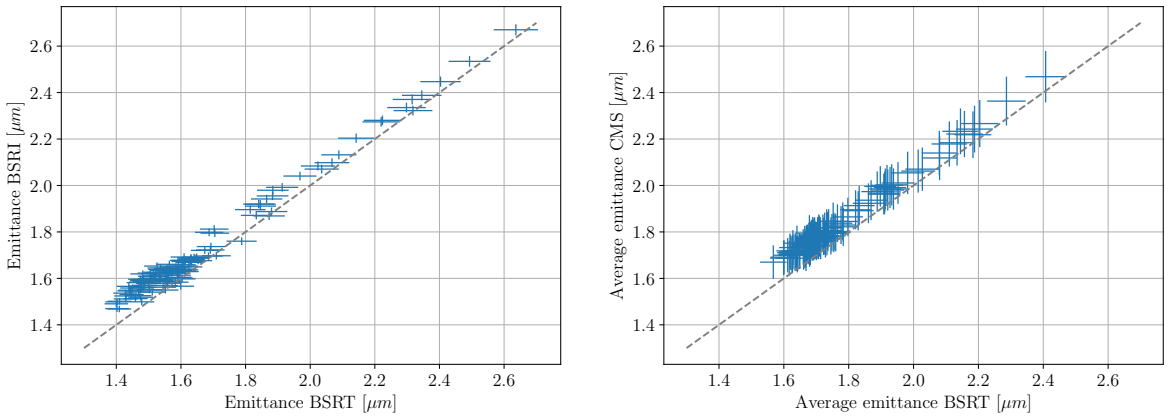

(a) (b)

Figure 6.15: Cross-comparison among synchrotron radiation monitors and CMS emittance scan performed during the 2023 Van der Meer run. In (a), comparison between the emittance of all bunches circulating in Beam 1, as measured by the BSRI and BSRT. In (b), the bunch-by-bunch average emittance between Beam 1 and Beam 2, as measured by the BSRT and inferred from the CMS luminometer. The identity line is displayed as a grey dashed line on both plots. The measurements refer to the vertical direction only and were performed during a special fill 8999, dedicated to Van der Meer scans.

In conclusion, the comparison with the experiment's emittance measurements provide valuable and independent insights but they also introduce inherent sources of uncertainty. The wire scanners offer a well-established reference, less prone to systematic errors. Therefore, comparison with the wire scanners during an emittance calibration fill remains the more reliable approach to assess the performance of novel systems for transverse diagnostics.

Conclusion and outlook

This thesis presented a comprehensive overview of the latest studies conducted on the synchrotron radiation source of the LHC and thoroughly investigated the performance of a synchrotron radiation interferometer as an instrument for non-invasive transverse beam diagnostics.

The spatial and spectral properties of the radiation emitted throughout a standard cycle of the LHC have been accurately characterized by numerical simulations, employing state-of-the-art codes for the modeling of synchrotron radiation emission and propagation. The most distinctive features of the LHC source were also studied by means of theoretical models, aiming to offer deeper insights into the physical origins of the observed properties. This framework allowed to accurately describe the characteristics of the synchrotron radiation in the stationary regimes of injection and flat-top energy, as well as following their evolution during the accelerator energy ramp. The outcome of this characterization extends beyond the scope of the synchrotron radiation interferometer, and may serve as a reference for the development of future diagnostics based on synchrotron radiation at the LHC.

Extensive simulations were also performed to characterize the spatial coherence properties of the radiation, with the goal of establishing models that link the spectral degree of coherence to the source distribution. At injection energy, the Van Cittert and Zernike theorem was confirmed in its canonical form, meaning that the transverse beam profile can be inferred from the decay of the degree of coherence through a simple Fourier transform operation. At high beam energy, the longitudinal extension of the source, the narrower emission angle of synchrotron radiation, and the presence of interference phenomena between multiple source elements hinder the straightforward applicability of the theorem. Nevertheless, strategies have been developed to mitigate the complications due to the source and restore the validity of the Van Cittert and Zernike formula, albeit in an approximate manner. The proposed approach is based on a redefinition of the source distance parameter and on the identification of specific configurations of the interferometer. These studies indicate that the operational requirement of achieving a $\pm 5\,\%$

emittance accuracy can be met at both injection and flat-top beam energies.

Systematic benchmark of the simulations was conducted during the initial year of LHC run 3. The measurement campaign utilized a test setup of the synchrotron radiation interferometer, which was refurbished and optimized based on the simulation findings. The setup produces interferograms featuring high-quality interference fringes. The fringe visibility exhibits a statistical fluctuation smaller than $\pm 0.5\,\%$, thus providing high stability in the source size measurement. The visibility measurement demonstrates a low sensitivity to variations in experimental parameters, such as changes in detector gain and exposure time. The response is very uniform across the entire acceptance of the system and marginally affected by the alignment of the various components of the optical line. These results demonstrate the interferometer's capability to provide relative measurements, enabling emittance evolution monitoring and comparisons between bunches of different sizes.

The results obtained from the interferometer are subsequently compared to reference measurements from the wire scanners to assess the absolute accuracy of the instrument. In particular, the visibility points measured by the interferometer are compared with the reference degree of coherence inferred from the wire scanner profiles. The reference degree of coherence is derived from the transverse profile using the Van Cittert and Zernike formula, with adjustments based on simulation findings to account for the specific characteristics of the LHC source at flat-top energy.

The agreement between the two instruments is confirmed at injection energy, where the measured visibility points are consistently confined within a tolerance of $\pm 2.5\,\%$ emittance error around the reference curve. Similar results are achieved in both the horizontal and vertical directions, in line with the uniformity of undulator radiation along both planes.

The comparison at flat-top energy yields an unexpected outcome, as the visibility measured by the interferometer is systematically lower than the values expected from the wire scanner profiles. The investigations carried out to identify the origin of this discrepancy did not yield conclusive results. Several observations, along with the absence of issues at injection energy, indicates that the observed discrepancy does not stem from a defect in the experimental setup. Instead, it appears to be related to a physical feature of the LHC source at high energy which is currently not taken into account in simulations. A semi-empirical model was found to correct this discrepancy and restore the agreement with the wire scanner reference. This model provides a compact formula to correct the raw visibility data, including a dependence on the slit separation

and a set of numerical coefficients that are fitted experimentally. The interferometer cannot provide absolute beam size measurements at flat-top energy until the physical origin of the discrepancy is understood. Nevertheless, the semi-empirical correction can be incorporated into the processing of the raw data as a calibration, allowing the instrument to remain an independent and redundant tool of non-invasive transverse diagnostics. In this context, an important outcome of the measurement campaign is the consistent reproducibility of the correction coefficients across the calibration fills conducted throughout the year.

The effectiveness of the visibility correction ensures that the problem of visibility loss, while remaining theoretically interesting, does not preclude the operation of the interferometer. A more relevant limitation concerns the capability of the instrument to resolve smaller beams at flat-top energy. This limitation is ultimately related to diffraction and therefore intrinsic to any optical technique. In interferometry, it is manifested by the impossibility to fully measure the coherence decay due to the coherence area extending beyond the narrow angular opening of the radiation. The current implementation of the interferometer operates in the visible domain, which poses challenges in reconstructing the profile of bunches with an emittance smaller than 1.5 µm. The only solution to mitigate the limitation imposed by diffraction is to reduce the operating wavelength, thereby decreasing the coherence area to fit within the available light extent. This involves a redesign of the system to operate in the ultraviolet range. While technologically challenging, the implementation of ultraviolet interferometry is undoubtedly the most effective option to enhance the theoretical performance of the technique and enable accurate reconstruction of the smallest bunch profiles.

It is important to emphasize that the diffraction limit primarily affects situations where the shape of the bunch profile is not known a priori and must be inferred from the sole interferometer measurements. If the bunch profile precisely follows a Gaussian distribution, the full decay of the coherence can be extrapolated from the fit of the available range of visibility points. This approach remains valid for non-Gaussian bunches, provided that the shape of the profile is known in advance and the effective size is left as a fitting parameter to match the measured points. Examples were shown in this thesis, using a combination of two Gaussian distributions to describe the transverse profile of the smallest bunches. The accuracy of this approach relies significantly on the knowledge of the shape of the input profile. Since the single visibility measurement satisfies the ±5 % uncertainty, the operational accuracy target can be met as long as an accurate profile is provided as input for the fitting process.

Based on the results presented in this thesis, the synchrotron radiation interferometer can be deployed in an operational scenario to complement the measurements provided by the synchrotron radiation telescope. In particular, it can be used as an expert tool to monitor the stability of the telescope measurements and detect any drift in its calibration. The interferometer is not suitable for continuous measurements as the lifetime of the detector would be drastically affected. However, the instrument could provide on-demand measurements, or automatic scans could be periodically performed during physics fills, for instance at the beginning of the stable beams phase when emittance scans are also conducted by the LHC experiments. The hardware of the test setup consists of standard components that are already used in the other synchrotron radiation monitors. The control tools developed for the experimental benchmark need to be adapted to facilitate the operational usage of the setup. This essentially involves limiting flexibility to enhance performance and ensure user-friendliness of the software tools. The challenge of achieving an absolute beam size measurement, independent of any calibration, persists until the source of the visibility discrepancy at flat-top energy is identified. This issue also limits the use of interferometry during the accelerator energy ramp. Although a correction strategy could be developed for this scenario, it would involve a series of several empirical models to adjust the raw visibility and follow the evolution of the synchrotron radiation source as a function of the beam energy. While feasible, this approach contradicts the principle of an operational instrument for transverse diagnostics, which should ideally provide a robust beam size assessment, minimizing the need for external corrections. Despite the progress and understanding of most phenomena observed in previous experiments, the synchrotron light source of the LHC remains an intriguing subject of study due to its complexity. Such studies are necessary to address current gaps and potentially enable the full exploitation of the interferometer for absolute beam size measurement during all stages of the accelerator energy ramp.

Appendix A

Synchrotron radiation field and intensity units

The wavefront of synchrotron radiation is fully described by the electric and magnetic fields

$$\begin{cases} \mathbf{E}(t) = \frac{q}{4\pi\epsilon_0}\left[\frac{\mathbf{n}\times((\mathbf{n}-\beta)\times\dot{\beta})}{cr_p(1-\mathbf{n}\cdot\beta)^3}\right]_{t'}, \\ \mathbf{B}(t) = \frac{\mathbf{n}\times\mathbf{E}(t)}{c}. \end{cases} \tag{A.1}$$

For most physical optics applications, it is more convenient to work in the space-frequency domain, where the wavefront is decomposed in a superposition of monochromatic waves. The transformation is performed through a Fourier transform and the Fourier-transformed field is

$$\tilde{\mathbf{E}}(\omega) = \frac{1}{\sqrt{2\pi}} \int \mathbf{E}(t) e^{-i\omega t}\, \mathrm{d}t\,. \tag{A.2}$$

This field is a complex vector that defines the intensity and phase of the radiation in the three-dimensional space. Synchrotron radiation is typically emitted within a narrow cone. In a coordinate frame where the longitudinal component is aligned with the propagation direction, the wavefront can be approximated as $\tilde{\mathbf{E}} \approx [E_x, E_y, 0]$. The longitudinal component is omitted and the problem reduces to the computation of sole transverse field. This is called paraxial approximation and it is often implicitly assumed when discussing synchrotron radiation.

The intensity of the radiation is quantified by the energy radiated per unit solid angle and unit angular frequency. It can be computed from the radiation field

$$\frac{\mathrm{d}^2 U}{\mathrm{d}\Omega\, \mathrm{d}\omega} = \frac{2r^2}{\mu_0 c}\left|\tilde{\mathbf{E}}(\omega)\right|^2. \tag{A.3}$$

This definition, given in SI units, is seldom used in practical cases as the light intensity is more conveniently quantified as a photon flux. In this thesis, the radiation intensity is always expressed as the number of photons per second emitted by a beam of 1 A current, in a 1 nm bandwidth, impinging on a unit surface of 1 mm^2. The corresponding unit is $\mathrm{ph}/(\mathrm{s\,mm^2\,nm\,A})$.

Numerical codes, like Synchrotron Radiation Workshop, normally compute the number of photons emitted in a bandwidth corresponding to 0.1% of the central frequency. This definition is tightly related to the concept of brilliance commonly used by the light source community. The conversion between the two definitions is reported for reference

$$I\left[\mathrm{ph}/(\mathrm{s\,mm^2\,nm\,A})\right] = I\left[\mathrm{ph}/(\mathrm{s\,mm^2\,0.1\%BW\,A})\right] \cdot \frac{10^3}{\lambda[\mathrm{nm}]}. \tag{A.4}$$

Appendix B

Derivation of the weak magnet model

The starting point of this derivation is the Liénard-Wiechert equation for the radiated electric field [24, p. 18] in time domain and in the observer frame. With the notations of Fig. 2.1, the electric field writes

$$\mathbf{E}(t) = \frac{q}{4\pi\epsilon_0}\left[\frac{\mathbf{n}\times((\mathbf{n}-\beta)\times\dot{\beta})}{cr_p(1-\mathbf{n}\cdot\beta)^3}\right]_{t'}, \tag{B.1}$$

where the subscript t' means that all quantities are evaluated at the emitter time. The solution of this field is in general complicated because of the conversion between emitter and observer time of Eq. 2.2. The situation drastically simplifies when the observation angle becomes almost constant and the time transformation reduces to $t = \kappa t'$. This occurs if the particle deflection is small and the length of the magnet is much shorter than the observation distance. The versor particle-observer is $\mathbf{n} \approx [\sin\vartheta\sin\varphi, \sin\vartheta\cos\varphi, \cos\vartheta]$. The weak deflection also implies that the motion remains almost longitudinal, i.e. $\beta \approx \beta[0,0,1]$. To simplify further the computation, we assume the non-restrictive hypotheses of small angles $\vartheta \lesssim 1/\gamma$ and ultrarelativistic regime $\gamma \gg 1$ which together yield $\mathbf{n} \approx [\vartheta\cos\varphi, \vartheta\sin\varphi, 1-\vartheta^2/2]$ and $\beta \approx 1$. These assumptions are also consistent with the expression $\kappa \approx (1-\boldsymbol{n}\cdot\boldsymbol{\beta}) = (1+\gamma^2\theta^2)/(2\gamma^2)$ already derived for Eq. 2.5. Finally, we need to obtain an explicit form for the particle transverse acceleration $\dot{\beta}$. Let us consider a vertical magnetic field $\mathbf{B}(z) = [0, B(z), 0]$ which exerts a Lorentz force on the charged particle. Taking advantage of the small deflection, one can neglect the effect of this force on the

longitudinal acceleration and assume $\dot{\beta}$ being purely transverse

$$\dot{\beta} \equiv \dot{\beta}_{\perp} = \frac{qB(z)}{m_0\gamma}[1,0,0], \tag{B.2}$$

being q and m_0 the particle charge and rest mass, respectively. Substituting these quantities in Eq. A.1, the radiated field becomes[1] and the field in time domain reads

$$\mathbf{E}(t) \approx \frac{4r_0c\gamma^3}{r_p}\left[B(z)\frac{[1-\gamma^2\vartheta^2\cos(2\varphi), -\gamma^2\vartheta^2\sin(2\varphi), 0]}{(1+\gamma^2\vartheta^2)^3}\right]_{t'}, \tag{B.3}$$

being $r_0 = q^2/4\pi\varepsilon_0 m_0 c^2$ the particle classical radius. The two terms in brackets represent the horizontal and vertical polarization components of the field, while the longitudinal component is negligible and thus omitted. This omission is consistent with the paraxial approximation of synchrotron radiation, where the narrow emission angle allows us to consider the SR wavefront as planar and purely transverse.

The last step to obtain the electric field in time domain is to perform the transformation between emitter and observer time scales. Since all angles are constant, the only term to be transformed in Eq.B.3 is the longitudinal coordinate

$$z \approx ct' = \frac{ct}{\kappa} = \frac{2\gamma^2}{1+\gamma^2\vartheta^2}ct \tag{B.4}$$

where we used Eq. 2.3. The resulting (transverse) field becomes

$$\mathbf{E}(t) = \frac{4r_0c\gamma^3}{r_p}\frac{[1-\gamma^2\vartheta^2\cos(2\varphi), -\gamma^2\vartheta^2\sin(2\varphi)]}{(1+\gamma^2\vartheta^2)^3}B\left(\frac{c}{\kappa}t\right) \tag{B.5}$$

Finally, the expression is Fourier-transformed to derive the field in space-frequency domain. The Fourier-transform acts solely on the magnetic field profile, the only time-dependent quantity left in this model. The final result for the radiated field is

$$\tilde{\mathbf{E}}(\omega) = \frac{2r_0\gamma}{r_p}\frac{[1-\gamma^2\vartheta^2\cos(2\varphi), -\gamma^2\vartheta^2\sin(2\varphi)]}{(1+\gamma^2\vartheta^2)^2}\tilde{B}\left(\frac{\kappa}{c}\omega\right). \tag{B.6}$$

The only quantity to compute in the weak magnet approximation is the Fourier transform of the magnetic field profile $\tilde{B}(k_{wm}) = \mathcal{F}\{B(z)\}$. The result is then evaluated at the "weak magnet" wavevector $k_{wm} = \kappa\omega/c$ and substituted into Eq. B.6 to obtain the field radiated at the angular

[1] The vectorial identity $\mathbf{a}\times(\mathbf{b}\times\mathbf{c}) = (\mathbf{a}\cdot\mathbf{c})\mathbf{b} - (\mathbf{a}\cdot\mathbf{b})\mathbf{c}$ is helpful to expand the triple product.

frequency ω. Since the approximation requires an almost constant observation wavelength, a sufficient condition is that the particle deflection is small compared to the typical SR emission angle of $1/\gamma$.

Notations

Abbreviation	Description	Page
LHC	Large Hadron Collider	2
IP	Interaction Point	2
BWS	Wire Scanner	10
BSRT	Synchrotron Radiation Telescope	11
BSRI	Synchrotron Radiation Interferometer	13
BGV	Beam Gas Vertex monitor	13
BGI	Beam Gas Ionization monitor	13
SR	Synchrotorn Radiation	16
WM	Weak Magnet approximation	20
SRW	Synchrotron Radiation Workshop	33
D3	LHC D3-type special dipole magnet	36
UND	LHC superconducting undulator	37
VCZ	Van Cittert and Zernike theorem	66

List of abbreviations and acronyms used in this thesis. The page number refers to the acronym definition.

Symbol	Descriptions
a	scalar
$\mathbf{a}$	vector
a^*	complex-conjugate of a
$\mathbf{a} \times \mathbf{b}$	vector product between $\mathbf{a}$ and $\mathbf{b}$
$\mathbf{a} \cdot \mathbf{b}$	scalar product between $\mathbf{a}$ and $\mathbf{b}$
$\triangleq$	equal by definition to
$\approx$	approximately equal to
$\simeq$	asymptotically equal to
$\propto$	proportional to

Notation adopted for mathematical expressions.

Symbol	Description	Page
$\mathcal{L}$	instantaneous luminosity	3
α, β, γ	Twiss parameters. Standard convention, distinction from relativistic factors clear from context	7
σ and σ'	beam size and divergence	7
D	dispersion	8
ε	normalized emittance	9
$\mathbf{r}$ and $\mathbf{n}$	vector for observation point and corresponding unity vector $\mathbf{n} \triangleq \mathbf{r}/r$	16
β and γ	relativistic factors. Standard convention, distinction from Twiss parameters clear from context or explicitly written as β_{rel} and γ_{rel}.	17
t and t'	observer and emitter time	17
$\mathbf{E}(t, \mathbf{n})$	electric field in space-time domain	17
$\kappa(t')$	time scale change factor	18
$\tilde{\mathbf{E}}(\omega, \mathbf{n})$	electric field in space-frequency domain, also referred to as "Fourier-transformed field"	20
I	optical intensity of a radiation field	20
λ, k, ω	wavelength, wavevector and angular frequency of a field described in frequency domain	20
K	undulator deflection parameter	22
λ_1	undulator proper wavelength	24
ω_c	dipole critical (angular) frequency	28
l_{coh} and σ_{coh}	coherence length and coherence area	60
$\Gamma_{12}(\tau)$	mutual coherence function	62
$\gamma_{12}(\tau)$	complex degree of coherence	62
$W_{12}(\omega)$	cross-spectral density	64
$\mu_{12}(\omega)$	spectral degree of coherence	65
σ_l and σ'_l	size and divergence of an elemental emitter in a source of light	70
V	visibility of an interferogram	96

Symbols used to denote recurring quantities. The page number refers to the definition of the corresponding variable.

Bibliography

[1] C. Communication and O. Group, "LHC: the Guide. Facts and figures about the Large Hadron Collider (LHC)," 2021.

[2] M. Benedikt, P. Collier, V. Mertens, J. Poole, and K. Schindl, "LHC Design Report, volume III, The LHC injector chain," tech. rep., CERN, 2004.

[3] J. Coupard, D. Manglunki, A. Funken, M. Meddahi, H. Damerau, B. Goddard, E. Chapochnikova, R. Garoby, R. Scrivens, G. Rumolo, *et al.*, "LHC injectors upgrade, technical design report," tech. rep., CERN, 2016.

[4] O. Brüning, P. Collier, P. Lebrun, S. Myers, R. Ostojic, J. Poole, and P. Proudlock, "LHC Design Report, volume I, The LHC main ring," tech. rep., CERN, 2004.

[5] H. Wiedemann, *Particle accelerator physics; 4th ed.* Springer, 2015.

[6] G. Arduini, W. Herr, T. Pieloni, and E. Métral, "Alternative bunch filling schemes for the LHC," 2007.

[7] M. Kuhn, *Transverse Emittance Measurement and Preservation at the LHC.* PhD thesis, Hamburg University., 2016.

[8] J. Wenninger, "Machine Protection and Operation for LHC," *CERN Yellow Reports*, 2016.

[9] A. Latina, "Introduction to transverse beam dynamics." Notes from the Joint Universities Accelerator School, 2019.

[10] H. Bartosik, "Non-linear effects." Notes from the Joint Universities Accelerator School, 2019.

[11] K. Wittenburg, "Overview of recent halo diagnosis and non-destructive beam profile monitoring," in *39th ICFA Advanced Beam Dynamics Workshop on High Intensity High Brightness Hadron Beams*, 2006.

[12] M. Sapinski and T. Kroyer, "Operational limits of wire scanners on LHC beam," in *Proceeding of the Beam Instrumentation Workshop, Lake Tahoe, California*, 2008.

[13] G. Trad, *Development and Optimisation of the SPS and LHC beam diagnostics based on Synchrotron Radiation monitors*. PhD thesis, 2014.

[14] M. Hostettler *et al.*, "How well do we know our beams?," in *7th Evian Workshop on LHC beam operation*, CERN, 2017.

[15] M. Hostettler, K. Fuchsberger, G. Papotti, Y. Papaphilippou, and T. Pieloni, "Luminosity scans for beam diagnostics," *Physical Review Accelerators and Beams*, Oct 2018.

[16] R. Tomás, "Beam size measurements requirements for HL-LHC," in *LHC Beam Size Review*, 2019.

[17] A. Alexopoulos *et al.*, "Noninvasive LHC transverse beam size measurement using inelastic beam-gas interactions," *Physical Review Accelerators and Beams*, 2019.

[18] S. Levasseur, *Development of a Hybrid Pixel Detector Based Transverse Profile Monitor for the CERN Proton Synchrotron*. PhD thesis, 2019.

[19] D. Butti, "Synchrotron radiation interferometry for beam size measurement in the Large Hadron Collider," Master's thesis, 2019.

[20] V. A. Bordovitsyn and I. M. Ternov, *Synchrotron Radiation Theory and Its Development*. World Scientific, 1999.

[21] Robinson, A, "History of Synchrotron Radiation," *Synchrotron Radiation News*, 2015.

[22] Zhang, X, *Synchrotron Radiation Applications*. World Scientific, 2018.

[23] J. D. Jackson, *Classical electrodynamics*. Wiley, 3rd ed. ed., 1999.

[24] Hofmann, A, *The Physics of Synchrotron Radiation*. Cambridge University Press, 2004.

[25] Kim, K, "Characteristics of synchrotron radiation," *AIP Conference Proceedings*, 1989.

[26] Hofmann, A, "Diagnostics with synchrotron radiation," 1998.

[27] Feynman, R P, *The Feynman Lectures on Physics, Vol I.* American Journal of Physics, 1965. Argument adapted from Chapter 34: Relativistic Effects in Radiation.

[28] R. Coïsson, "On synchrotron radiation in non-uniform magnetic fields," *Optics Communications*, 1977.

[29] Enge, Harald A., "Effect of Extended Fringing Fields on Ion-Focusing Properties of Deflecting Magnets," *Review of Scientific Instruments*, 2004.

[30] J. Schwinger, "On the Classical Radiation of Accelerated Electrons," *Phys. Rev.*, 1949.

[31] M. Bassetti, J. Bosser, M. Gygi-Hanney, A. Hofmann, E. Keil, and R. Coïsson, "Properties and Possible Use of Beam-Beam Synchrotron Radiation," *Nuclear Science, IEEE Transactions on*, 1983.

[32] M. M. Nikitin, A. F. Medvedev, M. B. Moiseev, and V. Y. Epp, "Interference of Synchrotron Radiation," *Sov. Phys. JETP*, 1980.

[33] O. Chubar, "Recent updates in the "Synchrotron Radiation Workshop" code, on-going developments, simulation activities, and plans for the future," in *Advances in Computational Methods for X-Ray Optics III*, SPIE, 2014.

[34] "Synchrotorn Radiation Workshop repository." `https://github.com/ochubar/SRW`. Last version: 02/10/2022.

[35] G. Geloni, V. Kocharyan, E. Saldin, E. Schneidmiller, and M. Yurkov, "Theory of edge radiation," 2008.

[36] Magnet Group, Brookhaven National Laboratory, "Design report for the Interaction Region Dipoles and the RF Region Dipoles," tech. rep., US/CERN LHC Accelerator Collaboration, 1999.

[37] R. Jung, F. Méot, and L. Ponce, *LHC proton beam diagnostics using synchrotron radiation.* CERN Yellow Reports: Monographs, CERN, 2004.

[38] D. Butti, "Status of the BSRT upgrade for HiLumi," in *11th HL-LHC COllaboration Meeting*, 2021.

[39] R. Maccaferri, D. Tommasini, R. Jung, W. Venturini-Delsolaro, and M. Facchini, "The 5 T superconducting undulator for the LHC synchrotron radiation profile monitor," tech. rep., 2004.

[40] F. Roncarolo *et al.*, "Electromagnetic Coupling Between High Intensity LHC Beams and the Synchrotron Radiation Monitor Light Extraction System," 2013.

[41] Bravin, E, "Possible synchrotron light upgrades for HL-LHC," in *LHC Beam Size Review*, 2019.

[42] M. Born and E. Wolf, *Principles of Optics: Electromagnetic Theory of Propagation, Interference and Diffraction of Light.* Cambridge University Press, 7th ed., 1999.

[43] K. J. Kim, Z. Huang, and R. Lindberg, *Synchrotron Radiation and Free-Electron Lasers: Principles of Coherent X-Ray Generation.* Cambridge University Press, 2017.

[44] N. S, H. Y, and A. H, "Edge radiation and its potential to electron beam diagnostics at HiSOR," *Nuclear Instruments and Methods in Physics Research Section A: Accelerators, Spectrometers, Detectors and Associated Equipment*, 2000.

[45] L. Mandel and E. Wolf, *Optical Coherence and Quantum Optics.* Cambridge University Press, 1995.

[46] E. Wolf, "A macroscopic theory of interference and diffraction of light from finite sources II. Fields with a spectral range of arbitrary width," *Proceedings of the Royal Society of London. Series A. Mathematical and Physical Sciences*, 1955.

[47] E. Wolf, "New theory of partial coherence in the space-frequency domain. Part I: spectra and cross spectra of steady-state sources," *J. Opt. Soc. Am.*, 1982.

[48] L. Mandel and E. Wolf, "Spectral coherence and the concept of cross-spectral purity," *J. Opt. Soc. Am.*, 1976.

[49] A. T. Friberg and E. Wolf, "Relationships between the complex degrees of coherence in the space–time and in the space–frequency domains," *Opt. Lett.*, 1995.

[50] F. Zernike, "The concept of degree of coherence and its application to optical problems," *Physica*, 1938.

[51] P. H. van Cittert, "Die Wahrscheinliche Schwingungsverteilung in Einer von Einer Lichtquelle Direkt Oder Mittels Einer Linse Beleuchteten Ebene," *Physica*, 1934.

[52] J. W. Goodman, *Introduction to Fourier optics*. Roberts and Company publishers, 2005.

[53] A. C. Schell, *The multiple plate antenna*. PhD thesis, Massachusetts Institute of Technology, 1961.

[54] W. H. Carter and E. Wolf, "Coherence and radiometry with quasihomogeneous planar sources," *J. Opt. Soc. Am.*, 1977.

[55] K. J. Kim, "Brightness, coherence and propagation characteristics of Synchrotron Radiation," *Nuclear Instruments and Methods in Physics Research Section A: Accelerators, Spectrometers, Detectors and Associated Equipment*, 1986.

[56] R. Coïsson, "Spatial coherence of Synchrotron Radiation," *Appl. Opt.*, 1995.

[57] R. Coïsson and S. Marchesini, "Spatial Coherence of Synchrotron Radiation," *Recent Research Developments in Optics,*, 2003.

[58] G. Geloni, E. Saldin, E. Schneidmiller, and M. Yurkov, "Transverse coherence properties of X-ray beams in third-generation synchrotron radiation sources," *Nuclear Instruments and Methods in Physics Research Section A: Accelerators, Spectrometers, Detectors and Associated Equipment*, 2008.

[59] F. Burkart, "Beam Loss and Beam Shape at the LHC Collimators," Master's thesis, Frankfurt University, 2012.

[60] W. Herr and B. Muratori, "Concept of luminosity." Notes from the CERN Accelerator School, 2006.

[61] J. K. Wood, K. A. Sharma, S. Cho, T. G. Brown, and M. A. Alonso, "Using shadows to measure spatial coherence," *Opt. Lett.*, 2014.

[62] H. Arimoto and Y. Ohtsuka, "Measurements of the complex degree of spectral coherence by use of a wave-front-folded interferometer," *Opt. Lett.*, 1997.

[63] B. L. Anderson and P. L. Fuhr, "Twin-fiber interferometric method for measuring spatial coherence," *Optical Engineering*, 1993.

[64] M. Koivurova, H. Partanen, J. Turunen, and A. T. Friberg, "Grating interferometer for light-efficient spatial coherence measurement of arbitrary sources," *Appl. Opt.*, 2017.

[65] Y. Takayama, H. Shiozawa, N. Takaya, T. Miyahara, and R. Tai, "Electron-beam diagnosis with Young's interferometer in soft X-ray region," *Nuclear Instruments and Methods in Physics Research Section A: Accelerators, Spectrometers, Detectors and Associated Equipment*, 2000.

[66] T. L. Wilson, K. Rohlfs, and S. Hüttemeister, *Tools of Radio Astronomy*. Springer, 2013.

[67] G. Iadarola and G. Rumolo, "Scrubbing: expectations and strategy, long range perspective," in *Chamonix Workshop on LHC Performance*, CERN, 2014.

[68] S. van der Meer, "Calibration of the effective beam height in the ISR," tech. rep., CERN, 1968.

[69] O. Karacheban, "Understanding the beam emittance evolution during stable beams based on emittance scans," tech. rep., CERN, 2019.